Drop Impact onto a Wall Wetted by a Thin Film of Another Liquid

Vom Fachbereich Maschinenbau
an der Technischen Universität Darmstadt
zur
Erlangung des Grades eines Doktor-Ingenieurs (Dr.-Ing.)
genehmigte

D i s s e r t a t i o n

vorgelegt von

Hannah Maria Kittel, M.Sc.

aus Marburg an der Lahn

Berichterstatter:	Prof. Dr.-Ing. C. Tropea
1. Mitberichterstatter:	Apl. Prof. Dr. I.V. Roisman
2. Mitberichterstatter:	Prof. Dr. M. Marengo
Tag der Einreichung:	16.04.2019
Tag der mündlichen Prüfung:	13.06.2019

Darmstadt 2019
D17 (Diss. Darmstadt)

Kittel, Hannah Maria:
Drop Impact onto a Wall Wetted by a Thin Film of Another Liquid
Darmstadt, Technische Universität Darmstadt
Jahr der Veröffentlichung der Dissertation auf TUprints: 2019
Tag der mündlichen Prüfung: 13.06.2019

Bitte zitieren Sie dieses Dokument als:
URN: urn:nbn:de:tuda-tuprints-89860
URL: https://tuprints.ulb.tu-darmstadt.de/id/eprint/8986

Dieses Dokument wird bereitgestellt von TU Prints, E-Publishing-Service
der Technischen Universität Darmstadt
http://tuprints.ulb.tu-darmstadt.de tuprints@ulb.tu-darmstadt.de

Hiermit erkläre ich, dass ich die vorliegende Arbeit unter der Betreuung von Prof. Dr.-Ing. C. Tropea und Apl. Prof. Dr. I.V. Roisman, abgesehen von den in ihr ausdrücklich genannten Hilfen, selbstständig verfasst habe.

Darmstadt, den 16. April 2019

What we know is a drop,
what we don't know is an ocean.

Sir Isaac Newton

...especially if the ocean is of another liquid.

Abstract

Drop/wall film interaction is an important process involved in many technical applications, such as fuel injection into the combustion chamber and spray cooling, coating or cleaning. In some cases the liquids of a drop and of a wall film are different. If secondary droplets result from this interaction, these droplets might contain both liquids. In an internal combustion engine this phenomenon could influence the combustion process and emission formation, and could potentially be a reason of pre-ignition events. The outcome of drop impact is influenced by several parameters, such as initial drop diameter, impact velocity, but also the fluid properties of both liquids and even on their miscibility. For technical applications it is necessary to know the different phenomenon involving outcomes such as maximum corona diameter and content of secondary droplets. Due to the large number of influencing parameters if both liquids are different, the process is highly complex and not fully understood yet.

In the present study the impact of a single liquid drop onto a thin liquid film of another miscible as well as immiscible fluid is investigated experimentally. The dynamics of drop impact are captured using a high-speed video system. For the investigation of the drop impact dynamics different configurations of the experimental setup are used: for study of the normal and inclined impact, for obtaining of the bottom view on the expanding corona, and for investigation of details of the flow of both liquids using a colour high-speed visualization.

Different outcomes resulting from normal drop impact are determined and classified regarding the influencing impact parameters: deposition, corona, splashing and partial rebound. Drop spreading is observed on highly viscous and soft substrates. The maximum spreading diameter on these substrates is determined for different impact conditions. For less viscous wall films, drop impact can lead to the expansion of a corona. The maximum corona diameter is investigated and determined for several fluid combinations. In case of drop impact onto an inclined wall film the impact leads to the expansion of a non-axisymmetric corona. The geometry of the non-axisymmetric expansion is determined and theoretically described.

Under certain conditions secondary droplets are formed as result of drop splashing. To predict splashing, splashing thresholds have been determined for wetted and soft substrates separately. Since both fluid properties influence the splashing

threshold, new scalings are introduced, which involve the properties of both liquids. It is shown that the well-known K number only determines the splashing threshold of the viscosity of the film if it is much larger or much smaller than the drop viscosity. For comparable viscosities of drop and wall film, a critical modified K number is introduced, which is a function of the viscosity ratio. Finally, the modified K number is used to predict splashing for typical engine conditions, since splashing is considered as one of the effects triggering pre-ignition in the engine. A further phenomenon, which is observed at some conditions, is corona detachment. In this case the corona detaches from the corona base leading to a secondary atomisation. This phenomenon is investigated and the range of parameters, for which corona detachment can be observed, is determined.

Finally, it is not only important to be able to predict whether splashing will occur or not, but also to know the content of multicomponent corona and secondary droplets, when the liquids of drop and wall film are different. To distinguish flows of different liquids, the drop is dyed and a colour high-speed visualization of impact is implemented. A calibration method is introduced and described, which allows the determination of the content ratio of both liquids in case of an immiscible droplet-in-droplet configuration. The distribution of both liquids in the corona and secondary droplets is determined. It is shown that the content of the secondary droplets is dependent on the wall film viscosity. It is demonstrated that the introduced method is applicable for future parametric studies of multicomponent droplets.

Kurzfassung

Die Interaktion von Tropfen und Wandfilm ist ein wichtiger Prozess in etlichen technischen Anwendungen, wie der Kraftstoffeinspritzung in die Verbrennungskammer, der Sprühkühlung, der -beschichtung oder -reinigung. In manchen Fällen sind die Flüssigkeiten von Tropfen und Wandfilm unterschiedlich. Kommt es zur Bildung von Sekundärtropfen, können diese Tropfen beide Flüssigkeiten enthalten. Auftreten von Sekundärtropfen in modernen Verbrennungskraftmaschinen kann den Verbrennungsprozess und die Schadstoffbildung signifikant beeinflussen. Des Weiteren kann Splashing Vorentflammung im Motor begünstigen. Das Resultat des Tropfenaufpralls wird von vielen Parametern beeinflusst, wie vom Tropfendurchmesser oder der Aufprallgeschwindigkeit, aber auch von den Flüssigkeitseigenschaften beider Flüssigkeiten, wie Viskosität oder Oberflächenspannung. Das Verständnis der unterschiedlichen Phänomene ist für viele technische Anwendungen unabdingbar. Von besonderem Interesse sind hier beispielsweise der maximale Kronendurchmesser und die Zusammensetzung der Sekundärtropfen. Wenn die Flüssigkeiten unterschiedlich sind, ist der Prozess aufgrund der großen Anzahl an Parametern hochkomplex und nicht vollständig verstanden.

In dieser Arbeit wird der Aufprall eines einzelnen Tropfens auf einen dünnen Flüssigkeitsfilm einer anderen Flüssigkeit, die miteinander mischbar sein können, experimentell untersucht. Die Dynamik des Tropfenaufpralls wird mittels einer Hochgeschwindigkeitskamera aufgezeichnet. Für die Untersuchung der Tropfenaufpralldynamik werden verschiedene Konfigurationen des Versuchsaufbaus verwendet: für die Untersuchung des normalen und geneigten Tropfenaufpralls, für die Untersuchung der Untenansicht der sich ausbreitenden Corona und für die Untersuchung der Zusammensetzung der Sekundärtropfen mittels einer Farbhochgeschwindigkeitskamera.

Verschiedene Resultate des Tropfenaufpralls werden bezüglich der Aufprallbedingungen klassifiziert: Deposition, Coronabildung ohne Splash, Coronabildung mit Splash sowie Partial Rebound. Die Tropfenausbreitung auf hochviskosen und soften Oberflächen, sowie die Bestimmung des Ausbreitungsdurchmessers als Funktion verschiedener Aufprallparameter, ist Grundlage der vorliegenden Studie. Im Falle von weniger viskosen Wandfilmen führt der Tropfenaufprall zur Bildung einer Krone. Der maximale Kronendurchmesser wird untersucht und für verschiedene Flüssigkeitskombinationen bestimmt. Beim Tropfenaufprall auf

einen geneigten Wandfilm bildet sich eine unsymmetrische Krone aus. Die Geometrie dieser Kronenausbreitung wird bestimmt und theoretisch beschrieben.

Unter bestimmten Bedingungen werden Sekundärtropfen durch Splashing gebildet. Um Splashing vorhersagen zu können, werden Splashinggrenzen für die benetzte und softe Wand bestimmt. Da die Eigenschaften von beiden Flüssigkeiten das Resultat beeinflussen, wird eine neue Skalierung eingeführt, die die Eigenschaften von beiden Flüssigkeiten berücksichtigt. Es wird gezeigt, dass die bekannte K Zahl lediglich die Splashinggrenze bestimmen kann, wenn entweder die Viskosität des Wandfilms viel größer oder viel kleiner als die des Tropfens ist. Für vergleichbare Viskositäten wird eine modifizierte kritische K Zahl als Funktion des Viskositätsverhältnisses eingeführt. Letztendlich wird die modifizierte K Zahl zur Vorhersage von Splashing im Falle typischer Motorbedingungen verwendet. Ein neues Phänomen wurde unter bestimmten Bedingungen entdeckt: Corona Detachment. In diesem Fall reißt die Krone an ihrer Basis an einem Punkt beginnend ab und schnellt nach oben, bis schließlich die Rim zerstäubt wird. Dieses Phänomen wird untersucht und die Bedingungen, unter denen Corona Detachment beobachtet werden kann, werden bestimmt.

Es ist nicht nur wichtig, Splashing vorhersagen zu können, sondern auch die Zusammensetzung von Mehrkomponentensekundärtropfen zu kennen, wenn die Flüssigkeiten unterschiedlich sind. Um die Flüssigkeiten zu unterscheiden, wird der Tropfen eingefärbt und mittels einer Farbhochgeschwindigkeitskamera aufgezeichnet. Eine Kalibriermethode wird eingeführt und beschrieben, die die Untersuchung der Zusammensetzung im Falle nicht mischbarer Flüssigkeiten erlaubt. Die Verteilung beider Flüssigkeiten in der Kronenwand und in den Sekundärtropfen wird bestimmt. Es zeigt sich, dass die Zusammensetzung von der Viskosität des Wandfilms abhängt. Es wird gezeigt, dass die eingeführte Methode für zukünftige Parameterstudien der Untersuchung Mehrkomponentensekundärtropfen verwendet werden kann.

Acknowledgements

First of all I would like to thank my supervisors Professor Dr. Ilia V. Roisman and Professor Dr.-Ing. Cameron Tropea for the extraordinary encouragement, the ongoing support and the opportunity to conduct my research at the Institute for Fluid Dynamics and Aerodynamics (SLA) of the Technische Universität Darmstadt. I am very grateful for all of the inspiring discussions, which always highly motivated me. Working in this group enabled me to gain scientific and also personal experience in facing complex problems and identifying of complex correlations. The unique facilities and equipment contributed in a large part to this study.

The financial support by the Deutsche Forschungsgemeinschaft (DFG) in the framework of the collaborative research center SFB-TRR 150 is gratefully acknowledged. My project gave me the opportunity to investigate the most fascinating and beautiful phenomena I can imagine. I was able to gain so many experiences due to the participation on international conferences as well as the research stay at the MIT. I would like to thank the colleagues from the SFB-TRR 150, especially Philipp Hänichen and Alex Weidenlener (aka *der harte Kern*), and from the Institute for Fluid Dynamics and Aerodynamics (SLA) of the Technische Universität Darmstadt, especially Sebastian Brulin and Dr.-Ing. Patrick Stegmann for so many fruitful discussions and sharing of unforgettable experience, personally and also professionally.

My research would not have been so successful without the help of my students. The long list: Sebastian Brulin, Him-Tschan Youn, Daniel Lehmann, Ganzaya Bayarsaikhan, Pascal Johe, Julius Breuer, Lana Wolni, Schirin Aghalale, Peter Hanauer, Dominik Rauen, Philipp Schneider, Mathis Schweigert, Yannik Fischer, Nicolas Häffner, Benjamin Hauska, Torsten Zerling, Butrint Zumeri, Anil Bayrak, Emre Abali, Cihat Ates, Sarah Keller, Florian Goertz, Niklas Matthias Quernheim, Louis Maximilian Reitter and Robin Philipp Schultheis.

Special thanks goes to my colleagues and friends at the Center of Smart Interfaces Ehsanul Alam, Michael Heinz and Anna Schmidt for all the contribution, discussions, support, helping hands, coffees and always supporting and pushing me and finally turning work into home. I want to thank the administrative team

consisting of Birgit Neuthe, Petra Fuhrmann, Corinna Neumann and Monika Medina and the workshop team headed by Ilona Kaufhold, their help and support contributed in a large part to the success of this study.

Last but not least, I would like to thank my parents, Dr. Rainer and Michaela Kittel, family and friends for always supporting me and also tolerating me in more stressful times during the last years. I cannot imagine how I should have done it without the best personal assistant, lab assistant, coffee maker, and so much more, someone could imagine, my husband Martin.

Contents

1 Introduction

Splashing from drop impact onto a liquid film is of high significance due to its importance in many industrial applications. For example, fuel mixture preparation and emissions in modern combustion engines are influenced by the interaction of fuel spray drops impacting onto lubricating oil films in the cylinder. Spray cooling during the process of hot forging [197] or functional printing [101] are further examples of technologies which involve drop film interaction of different liquids. In these examples the drop/wall interaction is affected by the fact that the drop and the liquid film are different liquids and may exhibit different degrees of miscibility.

The impact of a drop onto a surface, whether it is dry or wetted, soft or solid, has been extensively investigated in the past. Prediction of splashing as a result of drop impact onto a wetted substrate is rather important for modeling of different industrial processes, like spray coating or painting [81, 136, 173, 200, 201], microencapsulation [65, 68], spray cooling [87, 111], or for internal engine combustion processes [7, 168]. Fuel mixture preparation in modern combustion engines is influenced by the interaction of fuel spray droplets impacting onto lubricating oil films on the cylinder walls, resulting in splashing of mixed component drops into the combustion chamber. This modified mixture can significantly affect the combustion process resulting in degraded efficiency and increased pollution load [125]. Another example is the injection of AdBlue into the exhaust gas system of a vehicle. AdBlue is an aqueous urea solution of 32.5 wt.% urea, which is injected into the selective catalytic reduction in order to improve the emissions of a diesel engine. The effect of AdBlue injection is influenced, among other parameters, by the content of the urea/water film already existing on the wall, since this influences the composition of the splashed droplets. Besides applications in the automotive industry, spray cooling during the process of forming and forging and the role of additives in the lubrication solvents are further examples of where information regarding the splash occurrence after drop impact is of importance. The drop/wall interaction in all of these cases is affected by the fact that the drop and the liquid film are different liquids and may exhibit different degrees of miscibility.

Since all these applications show a very high degree of complexity the influence of each parameter is not clearly evident. To gain a better understanding of the physics of drop impact on wetted walls, first single drop impact experiments are conducted to isolate the corresponding parameters.

1.1 Hydrodynamics of drop impact

Different phenomena of drop impact can be distinguished: impacts onto dry and wetted walls, onto soft substrates and deep liquid pools. Additional phenomena, related to phase change, can appear during impacts under various thermal conditions, onto a very hot or very cold substrates. The diverse possible drop impact combinations. In this chapter the theoretical background and recent studies to drop impact onto dry walls and wetted walls are discussed.

The chapter starts with a fundamental description of the hydrodynamics of drop impact including the corresponding dimensionless numbers followed by a review of drop impact onto a solid, dry wall in Section 1.2, onto a wetted wall in Section 1.3 including different impact outcomes (Section 1.3.1), description of the corona propagation (Section 1.3.3) and the splashing threshold (Section 1.3.4). Finally, the chapter concludes with the recent studies of drop impact onto thin films of different liquids in Section 1.4, which is the main part of this study.

Dimensionless parameters Dimensional analysis is commonly used to analyse the relationship between physical variables. Therefore, the base parameters such as length, mass and time of the physical variables and the corresponding units are identified. Finally, by comparing the base parameters, dimensionless numbers are created by elimination of the units. The obtained numbers can be used to compare physical processes neglecting the corresponding units, to classify the results or to transfer the data [165]. Physical processes are therefore often described by the dimensionless parameters instead of the dimensioned variables. Thus, the experimental data can be generalized [201].

The falling drop is influenced by four forces, i.e. inertia, viscosity, gravity and surface tension forces. Impact parameters such as initial drop diameter D_0, impact velocity U_0 and film thickness h and fluid properties such as kinematic and dynamic viscosity ν respectively μ, surface tension σ and density ρ influence the drop impact. The following dimensionless numbers are used in this study to describe the physical processes.

The Reynolds number Re describes the ratio of inertia to viscous forces [166] and therefore shows the effect of viscosity compared to inertia. With increasing Re the inertia forces dominate over the viscous forces

$$\mathrm{Re} = \frac{U_0 D_0}{\nu} = \frac{U_0 D_0 \rho}{\mu}. \tag{1.1}$$

The Weber number We describes the ratio of inertia to surface tension. With increasing We the forces of deformation are dominating the surface tension leading

to a decrease of the drop shape of a sphere [48].

$$\mathrm{We} = \frac{\rho D_O U_0^2}{\sigma} \tag{1.2}$$

The Ohnesorge number Oh describes the influence of the viscosity on the deformation of drops and bubbles [121]

$$\mathrm{Oh} = \mathrm{We}^{1/2}\mathrm{Re}^{-1}. \tag{1.3}$$

The capillary number Ca is relevant to drop impacts on solid substrates if the dynamic contact angle influences the impact [201]

$$\mathrm{Ca} = \frac{\mathrm{We}}{\mathrm{Re}} = \frac{\mu U_c}{\sigma}. \tag{1.4}$$

with the contact line velocity U_c.

In order to describe the impact combination two dimensionless numbers related to the impact parameters are used: the viscosity ratio κ and the relative film thickness δ

$$\kappa = \frac{\nu_f}{\nu_d}, \quad \delta = \frac{h}{D_0}. \tag{1.5}$$

Furthermore, the dimensionless convective time τ defined as

$$\tau = \frac{tU_0}{D_0}, \tag{1.6}$$

is often used for the dimensionless presentation of transient phenomena.

1.2 Drop impact onto a dry, solid wall

The hydrodynamics of drop impact onto a dry wall have been studied rather intensively in the past, starting from the pioneer works of Worthington [194].

Different outcomes of drop impact have been identified [147] in the case of drop impact onto a solid substrate as shown in Fig. 1.1: deposition, corona and prompt splash, full and partial rebound. The outcome is determined by the impact parameters [132, 135, 183, 187] such as drop diameter, impact velocity and impact angle, liquid properties such as density, surface tension and viscosity, substrate properties [139, 144] such as wettability, roughness, material properties, elasticity and ambient conditions.

The observed outcomes are as various as the band width of applications. The outcome of the drop impacting onto a surface is determined by the properties of

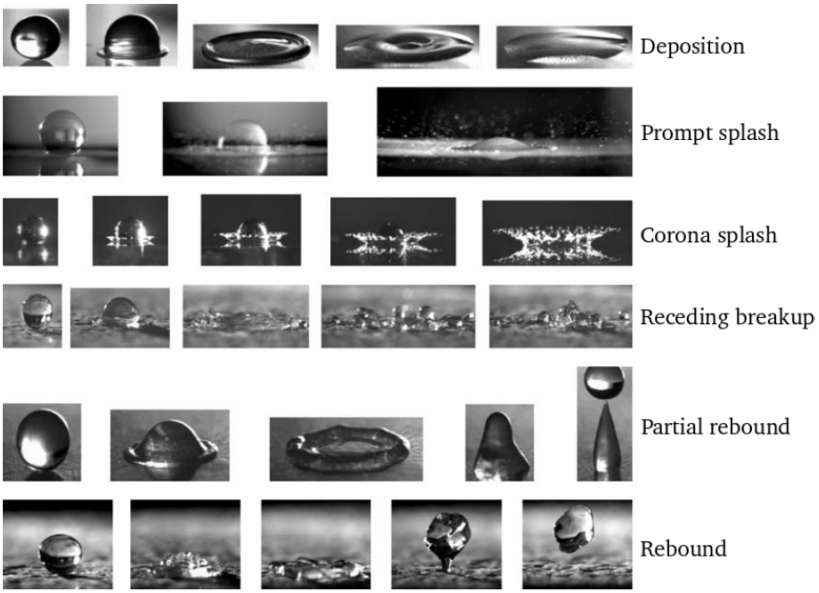

Figure 1.1: Different outcomes resulting from drop impact onto a dry wall: deposition, prompt and corona splash, receding break up and partial and complete rebound. Reprinted from [147]. Copyright (2001) with permission from Begell House, Inc.

the surface, whether it is wetted or dry, soft or hard. One such pioneering work is from Roisman et al. [157], where the authors introduced a theoretical model which predicts the spreading diameter taking into account inertia, viscous and surface tension forces as well as wettability. Due to both, the importance of the technical application and the different outcomes the drop impact has been and is still investigated regarding numerous impact conditions. Two most recent review articles summarised the research that have been undertaken over the past two decades [81, 200]. The authors mention that depending on the application certain outcomes are desirable, i.e. rebound in case of super-cooled drops impacting onto the surface of an aircraft or splashing in case of spray cooling. In order to fulfill the requirements of the applications the drop impact has to be understood.

Importance and industrial relevance of the phenomena of viscous drop impacting a deformable substrate [44], lead to intensive research in this field and an in-

creased number of publications in the last years. The study of deformable substrates have revealed deformation at the three-phase contact line due to the balance of surface tension and elastic stresses inside the substrate at the contact line [1, 112, 140, 162]. The existence of a wetting ridge at the moving contact line influences significantly the wetting and dewetting kinetics [8]. Recent studies of water drop impact onto deformable viscoelastic surfaces [4, 33] have demonstrated the influence of the viscoelastic dissipation during the receding phase.

Drop spreading and receding The drop impact consists of two phases, spreading and receding. These two phases are mainly governed by the motion of the rim. The drop impact onto a solid substrate generates a radially expanding flow in a thin lamella of nearly uniform thickness bounded by a rim which is created due to capillary and viscous forces [157, 171, 202]. Under certain conditions, the rim can get unstable and lead to the generation of secondary droplets. Yarin and Weiss developed an inviscid, remote approximation of the velocity field in the thin expanding lamella for high Reynolds and Weber numbers [202]. The following approximation satisfies the mass and momentum balance.

$$v_{r0} = \frac{r}{t+\tau}, \quad v_{z0} = \frac{2z}{t+\tau}, \tag{1.7}$$

with the radial and axial coordinates r and z and the corresponding velocity components v_{r0} and v_{z0}, the time t and the time constant τ.

On the other hand, an exact similarity solution of Roisman takes the viscosity of the droplet liquid into account [150]

$$v_r = \frac{r}{t} g\prime(\xi), \quad v_z = -2\sqrt{\frac{v}{t}} g(\xi), \quad \xi = \frac{z}{\sqrt{vt}}, \tag{1.8}$$

with the dimensionless function $g(\xi)$ of the similarity variable ξ. The analysis of the expansion of a viscous boundary layer in the spreading drop yields an expression for the residual thickness of the lamella [150]

$$h_{res} \approx 0.79 D_0 \mathrm{Re}^{-2/5}. \tag{1.9}$$

The contact area between the impacting drop and the substrate is described by the spreading diameter. The maximum spreading diameter is an important parameter in several applications such as spray cooling. The spreading diameter is determined by the flow inside the lamella and the propagation of the rim [150]. Consequently, Reynolds and Weber number as well as the substrate properties such as wettability determine the maximum spreading diameter additionally. The

spreading diameter has been already investigated from small scale of micrometer drops [181, 186] to big scale of millimeter drops [36, 97]. For the analysis of the spreading behaviour the dimensionless maximum spreading diameter $\overline{D}_{max,spread} = D_{max}/D_0$ is introduced. In the following several theoretical approaches describing the maximum spreading diameter are discussed.

Different approaches have been used modelling the maximum spreading diameter. Several authors focused on the energy balance of the impacting drop comparing the initial kinetic and surface tension energy of the drop with the surface tension energy of the lamella while accounting the energy loss due to viscous dissipation [30, 40, 57, 137, 193]. This kind of approach yields exemplary following algebraic equation [180]:

$$\begin{aligned} &A\overline{D}_{max}^3 - B\overline{D}_{max} + 8 = 0, \\ &A = 3(1 - cos\theta) + 4\mathrm{WeRe}^{-1/2}, \\ &B = \mathrm{We} + 12 \end{aligned} \tag{1.10}$$

with the contact angle between substrate and drop θ. The root of this equation predicts the maximum spreading diameter.

Scheller and Bousfield [159] as well as Marmanis and Thoroddsen [118] introduced the correlation between $\overline{D}_{max}$ and the K number $K = Re^{1/2}We^{1/4}$ (which is explained in Section 1.3.4 in more detail). Resulting from this correlation following expression was proposed [159].

$$\overline{D}_{max} \approx 0.61K^{0.332} \tag{1.11}$$

Clanet et al. introduced a scaling, i.e. $\overline{D}_{max}Re^{-1/5}$, dependent on the dimensionless impact parameter Λ as introduced in Eq. (1.12) in the case of drop impact onto a superhydrophobic substrate [39]. The impact parameter Λ describes two regimes, a non-viscous regime and viscous regime.

$$\begin{aligned} \Lambda = &\mathrm{WeRe}^{-4/5} \\ \Lambda > 1 \qquad &\overline{D}_{max} \sim \mathrm{Re}^{1/5} \\ \Lambda < 1 \qquad &\overline{D}_{max} \sim \mathrm{We}^{1/4} \end{aligned} \tag{1.12}$$

In contrast, Roisman scales with the residual lamella thickness h_{res} as introduced in Eq. (1.9). This model accounts for the motion of the rim under the influence of surface tension. Good agreement with experimental data is obtained [150]

$$\overline{D}_{max} = 0.87\mathrm{Re}^{1/5} - 0.4\mathrm{Re}^{2/5}\mathrm{We}^{-1/2}. \tag{1.13}$$

Butt et al. extended this model for superhydrophobic substrates ($\theta \to \pi$) [27]

$$\overline{D}_{max} = 0.87\mathrm{Re}^{1/5} - 0.48\mathrm{Re}^{2/5}\mathrm{We}^{-1/2}. \tag{1.14}$$

Splashing Whether or not splashing occurs is relevant to several applications and can also influence the spreading diameter. Therefore, several approaches modelling the splashing threshold have been made.

The splashing threshold is determined by various parameters such as impact parameters of the drop, substrate characteristics and also ambient conditions, such as surface roughness and temperature. Several empirical expressions for the splashing threshold have been developed, which allow to predict the transition from deposition to splashing. Such expressions account for the impact angle [16] or for substrate roughness [156]. Exemplary, the ambient gas material and its pressure can suppress splashing [98, 196]. Since the ambient atmosphere is not changed in this study, ambient pressure effects are not reviewed in more detail.

The substrate characteristics such as morphology and porosity can also significantly influence the impact outcome [105, 124, 148]. Porosity allows the liquid to partially penetrate the substrate and consequently the substrate imbibes liquid. Roughness enhances prompt splash. Roisman et al. defines a critical Weber number for prompt splash on rough and structured surfaces [156]

$$\mathrm{We}_{prompt} \approx 10(Rpk/Rsm)^{-0.83}, \tag{1.15}$$

with the average height of the protruding peaks above the roughness core profile Rpk and the mean width of the profile element Rsm.

The K number is used several times for predicting the corona splash, but several authors revealed that K is only applicable for a narrow range of drop impacts [16, 132, 135, 183]. Roisman et al. introduced empirical expressions based on existing experimental data [156]

$$\begin{aligned} \mathrm{Ca}_{corona} &= 0.067 + 0.6\ \mathrm{Oh}^{0.35} \quad && \mathrm{Re} < 450, \\ \mathrm{Oh}_{corona} &= 0.0044 && \mathrm{Re} > 450. \end{aligned} \tag{1.16}$$

Several studies focus on the impact phenomena by analyzing the influence of drop rheological properties on splash when non-Newtonian liquid drops are used.

Among these rheologically complex liquids are dilute polymer solutions on hydrophobic surfaces [15, 18] along with shear thinning [78, 86, 96, 102] and shear thickening liquids [22].

Splash phenomenon can be enhanced or suppressed also by choice of the substrates, by varying their bulk or surface properties [43]. Passive control for drop impact and its splashing is implemented, for example, in the design of icephobic surfaces [5, 9, 28, 82, 95, 122, 123, 175, 184]. Drop impact onto porous, nanofiber coated surfaces, which can be used for intensive cooling of microelectronic devices [167], is followed by fast drop penetration into the porous layer and the successive slow drop imbibition and evaporation. In many cases, coatings suppress splash and prevent rebound [105, 191].

Next to the influencing parameters of drop and substrate, temperature also plays a significant role. The impact outcomes are significantly different if the impact substrate is cooled or heated. In case of a heated substrate a temperature related regime occurs [23]. Drop impact onto a heated wall is related to spray cooling at the early stage or fuel injection in aircraft gas engines. In case of a drop impact onto cold surfaces or impact of supercooled drops involves additionally the thermodynamic process of solidification and is exemplary related to aircraft icing [161].

1.3 Drop impact onto a wetted wall

If the impact substrate is wetted, the drop firstly contacts the wetting liquid. If the substrate influences the impact outcome is dependent on the film thickness. The resulting outcomes differ from the outcomes on solid substrates, since the wall film liquid participates in most cases.

1.3.1 Outcomes of drop impact

Drop impact onto a wetted wall results in several different impact outcomes such as deposition, corona, prompt and corona splash and partial rebound [3, 133, 155] as shown in Fig. 1.2. For low Weber numbers two further impact outcomes are observed, floating and bouncing [134, 170]. In case of floating, the droplet floats on the surface of the wall film before it eventually coalesces with the film. The drop is (partially) reflected from the surface and jumps on the surface in the case of bouncing. Impacts of tiny drops ($D_0 \approx 0.5$ mm) or with low velocity on thin films lead to capillary waves. These waves propagate over the free surface of the wall film starting from the impact point. Gravity can be neglected for scales of the order of several millimeters and viscosity can be neglected for time scales in

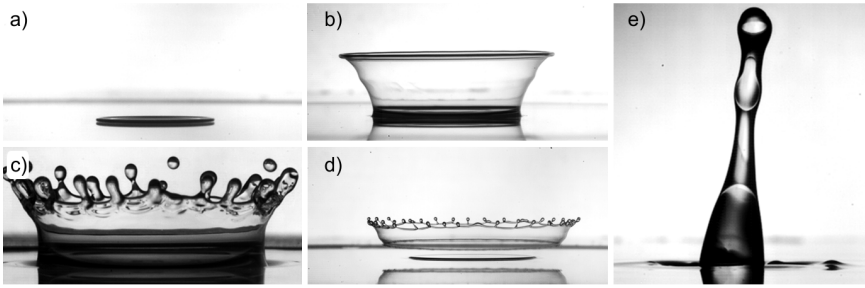

Figure 1.2: Different impact outcomes: a) Deposition, b) Corona, c) Corona Splash, d) Corona Detachment and c) Partial Rebound. Reprinted figure with permission from [92]. Copyright 2018 by the American Physical Society.

the order of several milliseconds [201]. Self-similar capillary waves are described and discussed in [202]. Since significantly higher Weber and Reynolds numbers are used in this study, these effects are not discussed in more detail. One important phenomenon is the rupture of the liquid film on a wall as a result of the fast spreading produced by drop or spray impact [83]. The flow instability leading to the film rupture can be enhanced by the presence of the second liquid of different surface tension. This phenomenon could potentially increase the wall deposition significantly under engine conditions.

The outcome of drop impact is influenced by the impact parameters (drop diameter D_0 and impact velocity U_0) and the material properties of the fluids (kinematic viscosity ν, density ρ and surface tension σ). Correspondingly, the main dimensionless parameters describing drop impact are the Reynolds and Weber numbers defined in Eq. (1.1) and Eq. (1.2).

The drop initially penetrates the wall liquid film, creating a crater. This crater first expands and then retracts because of capillary forces and gravity. If the impact velocity of the drop is relatively low, the impact generates a set of circular waves expanding on the wall film. At higher impact velocity and surface tension, retraction of the crater can lead to the generation of a central jet. In some cases this jet breaks up, leading to partial drop rebound [200].

Another recent study by [111] shows a review of drop impacts onto liquid films of the same liquid.

Table 1.1: Different wall film regimes

Wall film regime	Range of δ	References
Very thin film	$L_{nd} < \delta < 3R_{nd}^{0.16}$	[177]
	$\delta < 0.1$	[188]
Thin film	$3R_{nd}^{0.16} < \delta < 1.5$	[177]
	$\delta < 1$	[42, 127]
Shallow pool	$1.5 < \delta < 4$	[177]
Deep pool	$\delta \gg 4$	[177]

1.3.2 Wall film regimes

The phenomena resulting from drop impact onto a wetted wall is highly influenced by the film thickness (thin film or deep pool) due to its potential contact with the impact substrate. The effect ranges from influence of the substrate roughness till no influence in changes of the film thickness. Therefore, the wall film needs to be classified before discussing the impact phenomena. First classifications have been defined in the 1960s using the relative film thickness δ. Engel [53] defined shallow, $\delta < 2$, and deep pool, $\delta > 5$, regarding whether the pool bottom affects the impact (shallow pool) or not (deep pool). Furthermore, Engel constructed the hypothesis that secondary droplets created through drop impact use only 5% of the impacting drop kinetic energy. In contrast, Macklin and Hobbs [114] redefined shallow, i.e. $\delta \leq 0.5$, and deep pool, i.e. $\delta \geq 1.5$. Furthermore, the dimensionless surface roughness $R_{nd} = R_a/D_0$ and the length scale of roughness $L_{nd} = L_a/D_0$ are used for the classification of wall film regimes [177].

Nowadays, wall films are divided into different regimes: very thin film, thin film, shallow pool and deep pool [42, 127, 177, 188] as shown in Table 1.1. In this thesis, the relative film thickness is in the range of $0.03 < \delta < 0.36$ and therefore, in the very thin film and thin film regime.

The influence of the wall film thickness on the total number of secondary droplets in case of splashing was already studied in 1959 by Gregory et al. [69]. With increasing wall film thickness the number of secondary droplets decreases together with the height of the ejected jets [76].

(Very) Thin film If the drop impacts onto a (very) thin film the drop will touch the impact substrate. Due to this contact, the conditions of the impact substrate clearly influence the impact outcome. In this study, smooth glass plates are used and the corresponding surface roughness is negligible compared to the initial drop

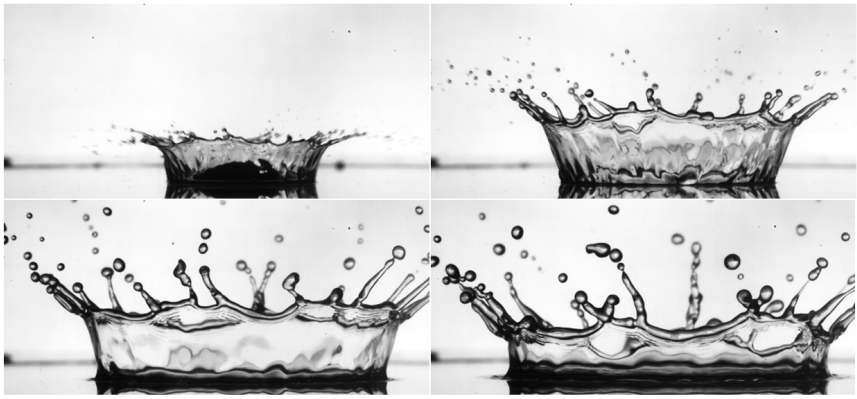

Figure 1.3: A water drop impacting onto a water wall film with $D_0 = 3$ mm, $U_0 = 3.1$ m/s and $\delta = 0.033$ and resulting Re $= 9500$ and We $= 420$

diameter. The corona propagation resulting from drop impact onto a thin wall film is described in more detail in Section 1.3.3. If the film thickness is comparable to the initial drop diameter but much bigger than the surface roughness, the wall film regime is called *thin film*. The surface roughness $R_{nd} = R_\phi/\phi$ gains in importance if the film thickness decreases. If the relative film thickness is comparable to R_{nd}, the regime is called *very thin film* [42], see Table 1.1.

This thesis focuses on drop impact onto (very) thin wall films ($0.04 < \delta < 0.35$) and therefore, the review focuses mainly on (very) thin wall films.

Shallow/Deep pool In the case of shallow or deep pool the impacting drop is not interacting with the impact substrate and therefore, the impact substrate does not play any role. Depending on D_0 and U_0 the drop is penetrating the liquid until the bulk liquid stops the penetration due to viscosity. A typical impact outcome is shown in Fig 1.4. The drop penetrates the semi-finite liquid pool and creates an expanding cavity which is similar to a spherical cap (half sphere). Inertia and surface tension then cause the receding of the cavity. The collapse of the corona creates capillary waves moving down to the receding cavity. Finally, the central jet is ejected [17]. For increasing impact velocities the formed corona can possibly arise further and neck in, which leads to a dome above the crater. This leads to a downward jet moving towards the raising crater. During the collapse, air bubbles can be possibly entrapped. A classification of different kind of bubble entrainment have been proposed by Pumphrey and Elmore [143]: irregular and regular

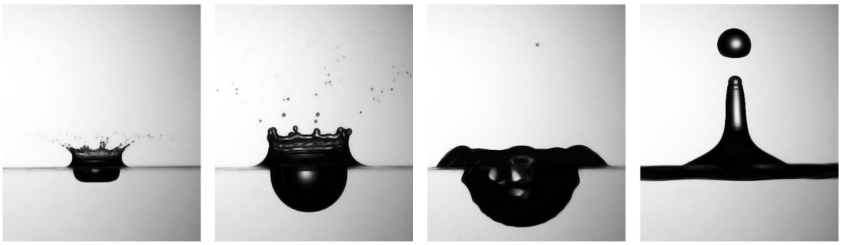

Figure 1.4: A water drop impacting onto a water deep pool with $D_0 = 2.8$ mm, $U_0 = 4.2$ m/s and $\delta \gg 4$ and resulting Re = 14638 and We = 683. Reprinted figure with permission from [17]. Copyright 2010 by the American Physical Society.

entrainment, entrainment of large bubbles and the Mesler entrainment. The film thickness is not influencing the impact outcome in the deep pool regime.

Comparing Fig. 1.3 and Fig. 1.4 the influence of the wall film regime is very obvious. Besides the wall film thickness the impact parameters are approximately comparable, therefore, the two different wall film regimes cause the different impact outcomes. In Fig. 1.4 the drop can penetrate the wall film liquid freely without influence of the wall leading to the formation of a crater. In Fig. 1.3 the drop motion is stopped at an early stage due to the wall leading to the formation of the corona.

Oblique drop impact If the wetted substrate is inclined, the wall film is not in rest anymore, but flows with the velocity V_τ driven by gravity. The impact velocity U_0 is measured normal to the wall. Using the inclination angle α the expression $\tan\alpha = V_\tau/U_0 = \overline{V_\tau}$ is used [201]. Several experimental studies focus on oblique drop impacts onto thin films [31, 109] and onto deep films [106, 131]. Cheng et al. focused on the numerical investigation of the oblique impact [37]. Che et al. [31] varied the Ohnesorge and Weber number of the drop as well as the Reynolds number of the film and observed phenomena such as bouncing, partial coalescence and splashing. Dependent on Weber and Reynolds number, the different outcomes are classified in a regime map. The flowing film affects the impact outcome significantly [31]. Liang et al. [109] focused on the influence of surface tension and viscosity. Spreading becomes asymmetric and no contradiction for the outer rim is observed. Consequently, also splashing is asymmetric. The size of the secondary droplets can be increased with increasing surface tension of the film. Okawa et al. [131] investigated the effect of inclination on the total mass of produced secon-

dary droplets. The authors observed a critical inclination angle for the formation of secondary droplets. For smaller inclination angle ($\alpha = 10° - 50°$) the size of the secondary droplets increases and therefore the total mass. Inclination angles of $\alpha = 50° - 70°$ lead to a decrease of size and total number. Exceeding $\alpha = 70°$, no secondary droplets are generated anymore [131]. Leneweit et al. [106] observed bouncing only till $\alpha = 14°$. Capillary waves are observed for small Weber numbers (We < 10), whereas for larger Weber numbers a lamella is ejected. The authors compared the experimental data with their numerical data and obtained good agreement. Cheng and Lou [37] showed that an increase of inclination leads to the transition from splash to partial splash till a critical inclination angle is reached and splashing is suppressed. Splashing becomes asymmetric with an elliptical lamella bottom.

Complex liquids Many studies focus on complex liquids due to the technical applications such as suspensions, emulsions [20, 50, 51, 73, 142] or encapsulated drops [38] onto dry substrates. One of the recent studies [108] is devoted to the impact of a liquid drop onto a deep pool of another, immiscible liquid. They have shown that at some threshold velocity the impact leads to the drop impact into several fragments and thus to the liquid emulsification. Similar phenomena could happen also after drop impact onto a liquid film if the impact velocity is high enough. Furthermore, Non-Newtonian liquids show a wide range of fascinating behaviour such as shear thinning or thickening, which is also very important in many applications such as painting [59].

1.3.3 Corona propagation

Drop impact onto a wetted wall with high impact velocity results in the formation and expansion of a corona. Due to the drop impact, the film in deformed. The expanding corona is nearly axisymmetric for the normal impact onto a homogenous wall film. The expanding base is circular starting from the impact point and only the radial velocity component in the film appears. The expansion of the corona is assumed to be inertia dominated and therefore viscosity effects are neglected (Re $\ll 1$). However, the velocity gradients can be high inside the drop at the first stages of the impact even for high Re and We. Even in this case the viscosity effect cannot overall be neglected, due to the viscous boundary layer near the wall. Outside of this viscous boundary layer the velocity of the liquid is in the same order as the impact velocity U_0.

The expansion of the corona can be divided into four regions, the liquid lamella on the wall film inside the corona, the undisturbed wall film outside the corona,

the corona sheet and the free rim bounding the corona. Due to the corona ejection a jump occurs in the wall film thickness and in the velocity in both liquids, which is described by the kinematic discontinuity shown in Fig. 1.5 [202].

The formation and expansion of the corona is explained in [202] by the kinematic discontinuity of the wall film. This inviscid theory [149, 202], valid for very high Reynolds and Weber numbers of impact, allows prediction of the temporal evolution of the corona radius (at the base of the corona) as $R_{\text{corona}} \sim t^{1/2}$ as a balance of inertia and surface tension forces. At large times of corona expansion, the influence of surface tension becomes significant. These forces, together with gravity, lead to deviation of the radius expansion from the square root dependence on time predicted by the inviscid theory. Moreover, at some instant the radius reaches a maximum and the crater begins to recede. The motion of the rim determines the complete lifetime of the corona, starting from the initial elevation till the surface tension and gravity driven collapse. The dimensionless maximum crater diameter and the corresponding dimensionless spreading time t_{max} are only slightly dependent on the initial film thickness and on the liquid viscosity and is in contrast determined mainly by the Weber number. These phenomena are investigated in detail and modeled in [13, 158].

Kinematic discontinuity The understanding of the dynamics of drop impact onto a liquid film is based on the study of Yarin and Weiss [202], where an asymptotic solution for an inviscid wall flow is found and the splash phenomena is described as a propagation of a kinematic discontinuity of a spreading film. The uprising free liquid sheet resulting from drop impact is formed due to this kinematic discontinuity. The kinematic discontinuity is described by using different regions as shown in Fig. 1.5. The wall film is separated by the base of the uprising liquid sheet and is shown in Region 1 and 2 in Fig. 1.5. The interface X_B represents the transition between these two regions and is presented as Region 3 in Fig. 1.5. At this interface two jumps occur, the film thickness jumps from h_1 to h_2 and the velocity from V_1 to V_2. This transition region resulting in these two jumps is called the *kinematic discontinuity* proposed by Yarin and Weiss [202]. The thickness of the kinematic discontinuity is in the same order of magnitude as h_1 and h_2. Region 4 is the rim bounding the free uprising sheet and will be discussed in Paragraph **Taylor rim**. The detailed theoretical derivation can be found in [201, 202]. For low Weber numbers crown formation is prevented since inertial forces are weak compared to the forces of surface tension. Therefore, the theoretical derivation in [201, 202] only considers inertia dominated impacts. Considering the magnitude of the velocity of the kinematic discontinuity (normal to its front) U and the specific volume flux into the kinematic discontinuity Q following expressions are

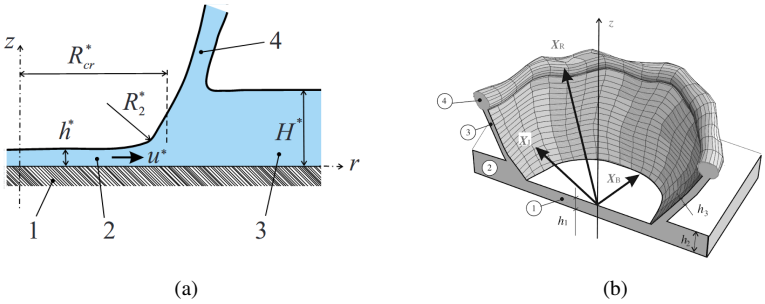

(a) (b)

Figure 1.5: Schematic sketches of the kinematic discontinuity: jump of the film thickness (a) (Reprinted figure with permission from [158]. Copyright 2008 by the American Physical Society Permission.) and the different regions of the uprising liquid sheet formed by the kinematic discontinuity (b) (Reproduced with permission [149]).

obtained [201].

$$U = \frac{1}{2}\left(V_{n1} + V_{n2}\right), \quad Q = \frac{1}{2}\left(h_1 + h_2\right)\left(V_{n1} - V_{n2}\right) \tag{1.17}$$

For a positive value of the sink term Q the kinematic discontinuity is formed by the interaction of two liquids on the wall as shown schematically in Fig. 1.5 (a). The thickness of the uprising sheet is assumed to be thin. The sheet experiences the effect of capillary, viscous, body and gas drag forces. The effect of the surface tension consists of the capillary pressure in the film and the functional surface tension force acting at the free surfaces [201].

Moreover, this study proposes a reliable and widely accepted form for the description of the splashing threshold, which depends, among other parameters, on the drop impact frequency. Following this theory, the velocity u, the lamella thickness h and the radius of the corona R_b can be expressed in dimensionless form as

$$\overline{u} = \frac{r}{t+\tau}, \quad \overline{h} = \frac{\eta}{(t+\tau)^2}, \quad \overline{R}_b = \beta\sqrt{t+\tau}. \tag{1.18}$$

where τ and β are constants. Here the drop initial diameter is used as a length scale and the impact velocity as the velocity scale [202].

Propagation of the corona in a liquid film has been studied in [158]. Experimental data agree well with Eq. (1.18) and show that surface tension influences the

evolution of the corona radius leading to its deviation from the predicted square-root dependence of R_b on time [41, 202]. Moreover, surface tension and gravity lead to the crater receding after its diameter reaches the maximum value $D_{\max}$.

Trujillo and Lee generalised this theory of Yarin and Weiss by taking the effect of viscous forces into account and improved the prediction of the propagation of the crown radius [179]. Since the difference is not as big though compared to the model of Yarin and Weiss, the liquid inertia is clearly the main influencing factor for high impact velocities [201].

Taylor rim The surface tension is balanced by the inertia of the liquid at the free edge of a free liquid sheet. The free rim propagating towards the liquid sheet occurs due to capillary forces [171]. The relative steady rim velocity V in normal direction to the centerline can be expressed by

$$V = \left(\frac{2\sigma}{\rho h_s} \right)^{1/2} \tag{1.19}$$

with h_s being the thickness of the free sheet. Eq. 1.19 is valid for low viscosities.

The propagation of the rim can explain many physical phenomena such as spreading and receding of drop impact onto a solid substrate and binary drop collision. The flow entering the rim from the free sheet and the capillary forces influence the rim dynamics and stability mainly. The surface tension can lead to an acceleration and to a deformation of the rim. If the rim becomes unstable, finger-like jets are produced, which can lead to the break up into secondary droplets. The flow in these jets can be considered as almost parallel to the plane of the free liquid sheet in the normal direction to the centerline of the rim. If the viscous stresses are comparable with the capillary pressure, the rim is deformed and not circular anymore. No rim at all is formed, if the viscous stresses are balanced by surface tension [201].

Rim instability and the mechanisms of splash still remain obscure and depend (probably) on the impact conditions. Some ideas about rim instability are discussed in the following. The stability analysis of a infinite cylindrical jet cannot describe the formation of finger-like jets and their break up. Therefore, the Rayleigh capillary instability cannot be considered solely. However, one remark of the analysis of Rayleigh says that the fastest growing perturbation of an infinite cylinder is axisymmetric, just as the rim deformation [155]. The Rayleigh capillary instability is only valid for no longitudinal stretching of the rim, what can be observed in propagating coronas though. Roisman et al. analysed the linear stability of the inviscid rim [155]. The obtained equation system is derived from the mass, momentum and angular momentum balance equations. With rim acceleration, the

growth rate of the rim perturbations increases significantly and decreases with the relative film thickness. The occurring wavelengths are comparable with the wavelengths obtained by Rayleigh and Weber [201]. The perturbation of the rim is not clearly visible when the formation of finger-like jets starts. The instability of the internal flow inside the rim can lead to the deformation of the rim cross section. This phenomenon can be explained by the long-wave approximation of the quasi two-dimensional theory of rim dynamics.

Stretching leads to viscous stresses in the liquid sheet influencing the dynamics of the rim. For low viscosity liquids, the effect of the rim formation on the liquid flow is small leading to the stretching as an independent parameter. The theoretical approach can be found in Yarin [199].

Viscous boundary layer Even for high Reynolds numbers, where inertial effects predominate viscous effects, viscous effects cannot be totally neglected, especially near the wall, where the velocity gradients and thus the viscous stresses are high. At the instant of drop impact a near wall viscous boundary layer occurs. In this boundary layer, the flow is significantly slowed down. The thickness of the boundary layer is

$$\delta_{BL} = 1.88\sqrt{\nu t}. \tag{1.20}$$

The velocity field in the boundary layer is expressed by

$$v_r = g'\left[\frac{z}{\sqrt{\nu t}}\right]\frac{r}{t}, \quad v_z = -2g\left[\frac{z}{\sqrt{\nu t}}\right]\frac{\sqrt{\nu}}{\sqrt{t}} \tag{1.21}$$

and the wall shear stress is expressed by [150]

$$\tau_w \approx 1.0354\sqrt{\nu}\rho r t^{-3/2}. \tag{1.22}$$

Residual film thickness A liquid film is formed below a penetrating and expanding cavity resulting from drop impact. The penetration velocity decreases when approaching the wall due to the wall effects [13]. The film thickness below the cavity follows the remote asymptotic solution of Yarin and Weiss [202] when inertia of the liquid is dominant. The viscosity effect damps the flow of the liquid film to a minimum film thickness below the cavity. A near wall viscous boundary layer occurs instantly at the impact for drop impacts onto thin films and high Re and We. At some time the thickness of this viscous boundary layer is comparable with the film thickness below the cavity. The thickness of the viscous boundary layer is a function of the square root of time, $\delta_{BL} \approx \sqrt{t/\mathrm{Re}}$ [153]. Finally, the dimensionless residual film thickness is described by

$$h_{res} = A(\delta)\mathrm{Re}^{-2/5}. \tag{1.23}$$

Numerical results yield the coefficient A.

$$A \approx 0.79 + 0.098\delta^{4.04} \tag{1.24}$$

For thin wall films (small δ) the approach is similar to the impact onto a solid wall [201].

1.3.4 Splashing threshold

One of the most important outcomes for many technical applications is splashing, occurring when drop impact leads to the generation of a number of secondary droplets. Two main kinds of splash has been identified, the *corona splash* and the *prompt splash* [74, 107, 115, 147, 188, 195]. Occasionally, also corona detachment has been observed during spray impact in microgravity by [154], leading to the generation of larger secondary droplets, formed from the corona rim. This phenomenon is described in Chapter 6 in more detail. In *prompt splash* fine secondary droplets are produced from the jets ejected immediately after the impact. The *corona splash* occurs when the inertial effects in the flow generated by drop impact are significant. The effect of capillary forces is also significant at the edge of the uprising sheet forming the corona. These forces lead to the formation of a propagating rim [152, 171, 202], growing due to the flow entering the rim from the free liquid sheet. The rim bounding an uprising sheet is unstable. If the corona expansion time is long enough ($t_{splash} \ll D_0/U_0$), the rim instability can lead to the formation of cusps [155, 202] and finger-like jets, which then finally break up and generate a number of secondary droplets. Two kinds if perturbation waves can be observed during corona formation: longitudinal and azimuthal waves. While the longitudinal waves propagate in vertical direction in the corona, the azimuthal waves can be observed along the cylinder as periodical swallowing. The azimuthal waves seem to be correspondent to the roots of the jets [42]. The cusps are formed by the liquid motion inside the rim.

Among the parameters which are mostly studied in the field of drop impact are the splashing threshold, diameter of the secondary droplets and their mass ratio scaled by the mass of the impacting drop, maximum spreading diameter of the drop or of the corona. Comprehensive reviews [81, 117, 200, 201] of drop impact phenomena and their modeling can be found in the literature.

Empirical correlations can be formulated for the splashing threshold

$$\mathrm{K} = 2100 - 2700\exp(-58.\delta), \quad 0.02 < \delta < 0.1, \tag{1.25}$$

$$\mathrm{K} = 2100 + 5880\delta^{1.44}, \quad 0.1 < \delta < 1. \tag{1.26}$$

based on the existing experiments [42, 146], where the splashing threshold parameter K is defined as

$$\mathrm{K} \equiv \mathrm{We}^{4/5}\mathrm{Re}^{2/5}. \tag{1.27}$$

The splashing threshold for drop impact onto a wetted substrate has been introduced in the form of the critical K number [128], defined as

$$\mathrm{K} = \mathrm{We}^{1/2}\mathrm{Re}^{1/4}. \tag{1.28}$$

The formulation of the parameter K can be explained by the assumption that splash occurs when the inertial forces are much larger than forces associated with surface tension [42, 202]. An empirical expression for the critical K number [42] for drop impact onto a film is

$$\mathrm{K}^{8/5}_{\mathrm{critical}} = 2100 + 5880\,\delta^{1.44}, \quad \delta = \frac{h}{D_0}, \tag{1.29}$$

where h is initial thickness of the unperturbed film, and δ is its dimensionless value.

More recent studies [146] on drop impact onto thin liquid films ($\delta < 0.15$) claim that the K number is still not a reliable dimensionless parameter. Moreover, the K number is definitely not suitable for the description of drop impacts onto dry solid substrates [156].

The splashing threshold of a drop impacting onto a thin film [183] is obtained in the form

$$\left(\mathrm{Re}^{0.17}\mathrm{We}^{0.5}\right)\Big|_{\mathrm{critical}} = 63, \tag{1.30}$$

however, the relative film thickness δ has not been documented in these experiments.

The splashing threshold in the case of inclined drop impact onto a deep pool [131] is described by the critical K number computed using the normal component of the impact velocity. The corresponding splashing threshold is

$$\mathrm{K}^{8/5}_{\mathrm{n,critical}} \approx 2100, \quad \delta \gg 1. \tag{1.31}$$

1.4 Drop impact of different liquids

Most studies focus on the drop impact onto a wall wetted by the same liquid. However, in many technical applications drop and wall film are not the same liquid. For example during the fuel injection into the combustion chamber some relatively large fuel drops impact onto a cylinder surface wetted by a thin oil layer. The properties of these liquids, mainly viscosities, can be very different. The differences in the liquid properties may affect the impact outcome significantly. Not only the fluid properties of both liquids influence the impact, but also their miscibility is important.

Miscibility Miscibility describes the property of materials to fully dissolve in each other to a homogeneous solution. Random molecular motion causes diffusion until a homogeneous solution is obtained and can be described by a diffusion flux as the rate per unit area at which mass moves [46]. The diffusivity coefficient expresses the rate of the diffusion progress. Diffusion is mostly a slow process. This process can be accelerated by stirring, even if stirring is a macroscopic motion. Diffusion can be mathematically described either by Fick's law or by mass transfer. Fick's law is commonly used in physics, physical chemistry and biology, while mass transfer is used in chemical engineering. Fick's law yields for a steady state system the constant flux in z direction [46]

$$j_i = -D\frac{dc_1}{dz} = \frac{D}{l}(c_{10} - c_{1l}) \tag{1.32}$$

with the constant diffusion coefficient D, the distance l and the concentrations c_{10} and c_{1l}.

Immiscible liquids do not form a solution but form an interface separating each other immediately. Interfacial tension describes the surface energy between two immiscible liquids σ_{AB} for phase A and B. The inferfacial tension of water/oil is $\sigma_{WO} \approx 50$ mN/m at room temperature [49]. Considering an oil droplet covered by water the oil drop tries to lower its potential energy and forms a sphere of radius R. The covering water drop has the radius $R + dR$. The work done by pressure and capillary force is defined by [49]

$$dW = -p_O dV_O - p_W dV_W + \sigma_{OW} dA \tag{1.33}$$

with the increase in volume $dV_O = 4\pi R^2 dR = -dV_W$ and in surface $dA = 8\pi R dR$ and the pressure of the oil and water drop, p_O and p_W. The greater the inner pressure, the smaller the drop. Finally, the Laplace's theorem yields

$$\Delta p = \sigma\left(\frac{1}{R} + \frac{1}{R'}\right) \tag{1.34}$$

with the radii R and R' of the curvature of the corresponding surfaces [49].

The effect of miscibility on the impact outcome is studied in Chen et al. [35]. Chen et al. observed that miscibility suppresses the formation of the corona as well splashing due to the enhancement of the kinetic energy transfer between drop and wall film. This leads to an decrease of the kinematic discontinuity. Independently, high Weber numbers enhances splashing, while high viscous wall films suppress splashing. In contrast, for less viscous wall films having a higher film thickness promotes splashing. In case of immiscible drop impact onto high viscous wall films advancing is comparable to impacts onto solid substrates. Also, immiscibility could influence the receding phase [35].

Drop impacts with very high Reynolds and Weber numbers (up to $Re_d = 1100$, $Re_f = 39000$ and $We_d = 5600, We_f = 10500$) of miscible liquids were studied by Thoroddsen et al. [174] in 2006. Under these conditions crown breakup by Marangoni holes have been observed and studied. Water/glycerine drops impacting onto a very thin sheet of ethanol lead to a two-stage splashing phenomenon. First, very fine secondary droplets are ejected very fast from the ethanol sheet. Afterwards, the viscous drop starts to form a bowl out of the wall film. This bowl contains also two parts, since the less viscous wall film liquids shows a different dynamic behaviour than the higher viscous drop liquid. The upper part of the corona consisting of the wall film liquid collapses and forms secondary droplets, while the bowl, formed by the drop, is still intact. The secondary droplets close to the wall puncture holes in the crown. After the secondary drop contact this part thins, driven by solute Marangoni flow, and finally ruptures to a hole. These growing holes form a net-like structure. This phenomenon was also observed for other wall film liquids of low surface tension [174]. Aljedaani et al. [6] continued this study by varying the liquids of drop and wall film and also the wall film thickness. Furthermore, for better visualization, dye was added to the liquid of the drop in some of the presented experiments. Aljedaani et al. confirmed the hypothesis of [174] that secondary droplets impacting on the corona wall lead to the formation of these holes. The influence of the viscosity and surface tension of both liquids as well as of the film thickness on the formation of hole was investigated in this study. Three different velocity regimes have been observed during hole formation: spreading speed of the Marangoni patches, rupture speed of the sub-micron thin film and the growth rate of the film. Since in the study of Thoroddsen et al. [174] the surface tension of the wall film liquid was always smaller than the surface tension of the drop, Aljedaani et al. observed that the formation of holes is driven by compressive Marangoni stresses if the surface tension of the wall film is bigger [6].

Martson and Thoroddsen [119] investigated the impact of a viscous drop onto a

less viscous pool forming vertical jetting from the apex. An ejected sheet is formed from the free surface of the pool moving up and wrapping the surface of the drop. A thin, fast upward jet is produced when the liquid sheet converges and collides. This phenomenon can be only observed in a limited range of conditions. A thin ejecta sheet can be generated on a low viscous pool. The minimum Reynolds number for miscible liquids in this study is approximately 3400. For small inertia separation of the sheet from the drop surface is avoided [119].

Banks et al. [11] investigated the effect of viscosity for both miscible and immiscible liquids during drop impact onto a pool $\delta = 1$. The authors observed that splashing is dependent on the properties of the drop liquid, while the corona propagation is governed by the properties of the pool liquid. Even if the authors do not change the film thickness, they proposed that the viscosity of the film could influence also the effect of the film thickness [11].

Recent studies by Fujimatsu et al. [56], Lhuissier et al. [108] and Shaikh et al. [163] are devoted to the impact of a liquid drop onto a deep pool/thin film of another immiscible liquid. Fujimatsu et al. [56] investigate the interfacial deformation resulting from a water drop impacting onto a silicone oil pool of different viscosities. Seven different patterns of cavity have been observed. The limit of drop disintegration can be correlated with Oh and Re. Lhuissier et al. [108] have shown that at some threshold velocity, the impact leads to a disintegration of the drop into several fragments, and thus to the liquid emulsification. Similar phenomena could occur after drop impact onto a liquid film, if the impact velocity is high enough. Contrary to Lhuissier et al. [108] Shaikh et al. [163] observed that the mean diameter of the secondary droplets increases with increasing Weber number of the impacting drop. Using a power law the dependency is described by $d_{mod} \sim \mathrm{We}^{-1/4}$.

Murphy et al. [129] investigated the production of marine aerosol by raindrop impact on the sea surface due to splashing. This complex process consists of three interacting liquids, which are miscible and immiscible in each other: the impacting water droplet, the sea water and a thin oil layer floating on top the sea water. In this study the deep pool consists of sea water covered by different kinds of oil. The effect of the oil layer on the impact outcome is investigated and dependent on the thickness of this layer different regimes of splashing were observed. Several phenomena have been observed such as double corona, bubble canopy, jetting and cavity formation. The oil layer behaviour can divided into immediate rupture, delayed rupture or no rupture [129].

Che and Matar [32] observed the influence of surfactant on the impact outcome. Surfactants are used to lower the local surface tension and therefore to alter the impact process. The drop motion during the impact is tracked by adding dye to

the liquid of the drop. Surfactants are added either to the drop, to the film or to both drop and film, what changes significantly the impact outcome. Occurring surface tension gradients lead to a strong radial flow due to the Marangoni effect in the case of surfactant droplets. For surfactant wall films a stabilisation of the flow in the liquid film, flower patterns could be observed. Furthermore, the propagation of the capillary waves, the evolution of the corona and the formation of secondary droplets are altered [32].

Recent numerical studies by Blais et al. [19] and Guo and Lian [71] investigated the effect of the density of the drop and wall film. However, both studies focussed the numerical methods such as interface reconstruction and used drop impact as verification test case. Guo and Lian considered the oblique impact and observed that higher tangential velocity leads to lower lamella height on the backside of the drop. Furthermore, lower densities of the film liquid can lead to earlier splash and corona break up [71].

Recent studies of Geppert et al. [61–64] and Bernard et al. [14] focused on the investigation of hexadecane/hypsin combinations. Based on these liquids the impact parameters are varied systematically covering a wide range. Using this parameter space the formation of corona regarding corona base diameter and height as well as total number and size distribution of secondary droplets and the splashing threshold are investigated in terms of $\mathrm{We_d}$ and δ. The observed phenomena are consequently classified in regime maps in terms of $\mathrm{We_d}$ and δ. For the liquid combination hexadecane/hypsin an empirical correlation describing the splashing threshold has been determined

$$\mathrm{We}_d^{5/8}\mathrm{Oh}_{\overline{\mu}}^{-1/4} = 114 + 163\delta^{6/5}, \tag{1.35}$$

with the arithmetic mean of the fluid properties used in [61]

$$\mathrm{Oh}_{\overline{\mu}} = 0.5\frac{(\mu_d + \mu_f)}{\sqrt{\rho_d D_0 \sigma_d}}. \tag{1.36}$$

The authors observed that an increasing wall film thickness leads to a suppressing of splashing. With increasing film thickness the required kinetic energy increases simultaneously. For a very narrow range of film thickness $0.03 < \delta < 0.14$ Geppert et al. observed the detachment of the corona as a special kind of splashing. The authors assume that partial wettability and surface roughness could induce the rupture in the wall film [63].

Terzis et al. [172] investigated the impact of an AdBlue (Diesel exhaust fluid) droplet onto thin films of urea water solutions motivated from the exhaust gas system. According to [61] the classification of impact outcomes is presented in a

regime map. Terzis et al. modified Eq. 1.35 for the combinations of urea water solutions.

$$\mathrm{K} = \mathrm{We}_d \left(\tilde{\mathrm{Oh}}_{d,f}^{-1/4} \right) = 1413 + 9347\delta^{1.2} \tag{1.37}$$

with $\tilde{\mathrm{Oh}}_{d,f} = \frac{1}{2}(1+\kappa)$ in the range of $0.1 < \delta < 0.6$. Furthermore, the total number of secondary droplets can be estimated by

$$N_{sec} = 0.0392\delta^{-0.078}\mathrm{We}_D^{1.26}\left(\frac{\mu_f}{\mu_d}\right)^{-0.078}. \tag{1.38}$$

In [92] the splashing threshold of a liquid drop impacting onto a solid substrate wetted by another liquid is studied. Three main regions are identified. In the case when the viscosity of the wall film is much higher that the viscosity of the drop, the properties of the drop govern the process of splash. In the case of drop viscosity much higher than the film viscosity, the splash is governed by the properties of the film. In the case when the viscosities of the film and of the drop are comparable, the splashing threshold depends on the viscosity ratio. This approach is discussed more in detail in Chapter 5.

1.5 Thesis outline

The main objective of the present thesis is to enhance the understanding of the physics of drop impact on thin wall films of different liquids and to develop theoretical models predicting the splashing threshold and corona evolution. Therefore, the experimental investigation of the single drop impact on thin wall films of different liquids is in focus of this study. The outline of this study is mainly organized into the parts phenomena of drop impact, splashing consisting of splashing threshold, corona detachment and content of multicomponent corona and secondary droplets.

In **Chapter 2** the different experimental setups and the corresponding measurement technique principles including the measurement of the liquid properties, high speed imaging and confocal chromatic imaging are described in detail. The corresponding uncertainty of measurement is discussed and the post processing method is briefly explained.

Chapter 3 gives an overview of the different outcomes of drop impact and the influencing parameters. Drop spreading on high viscous and soft substrates is discussed. For less viscous wall films, the evolution of the corona is described and discussed.

Chapter 4 shows the effect of inclination on the drop impact outcome and the corresponding non-axisymmetrical corona evolution is discussed. The formation of holes resulting from concentration differences in drop and wall film is discussed.

In **Chapter 5** the mechanisms of splashing are described. The splashing threshold is investigated for several drop impact combinations and finally, a theoretical model predicting the splashing threshold is introduced covering a big range of viscosity ratios. The developed model is used for first recommendations for action for the combustion engine. This chapter concludes with splashing threshold for drop impacts onto soft substrates.

In **Chapter 6** the newly discovered phenomena corona detachment is described and discussed. The required conditions are discussed regarding the impact parameters and the physics are described.

In **Chapter 7** the distribution and content of multicomponent corona and secondary droplets are investigated. A calibration method is introduced to determine the content ratio of multicomponent secondary droplets.

Chapter 8 concludes the present thesis and presents an outlook for future research.

2 Experimental method

In this chapter the experimental methods are described. Different experimental setups have been designed to investigate the different drop impact phenomena: horizontal drop impact, impact of dyed drops, inclined drop impact and horizontal drop impact observed from below and sideways. Section 2.1 describes the experimental setup of the horizontal drop impact. This setup is used under different configurations in Section 2.1.5 for the impact of dyed drops, in Section 2.1.6 for the drop impact on soft substrates and in Section 2.1.7 for the additionally observation of the drop impact from below. Section 2.2 describes the experimental setup of the inclined drop impact, and, finally, in Section 2.3 the different measurement techniques are discussed. Parts of this chapter have been published in [90–92, 160]. Furthermore, parts of the experimental methods have been described in the theses of Brulin [26] and Youn [203] and several student project works.

2.1 Experimental method of the horizontal drop impact

The experimental setup consists of three main parts, the drop generator, the impact substrate and the observation system and is schematically shown in Fig. 2.1. Each part is described in detail in the following sections. All experiments are conducted at standard ambient conditions ($p \approx 1$ bar, $T \approx 295.65$ K).

The observation system allows detailed observations of the drop impact dynamics onto liquid films. These observations allow the qualitative and quantitative investigation and characterisation of the drop impact dynamics.

2.1.1 Drop generation

The drop generator is based on a drop-on-demand method. A micro-pump transports the fluid from a tank to the cannula. The fluid forms a drop at the end of the tip of the cannula. The drop drips off the cannula tip by gravity if the critical mass is reached. In order to vary the initial drop diameter, different cannula diameters d_c are used in the range from 0.3 mm to 0.8 mm. The initial drop diameter D_0 is

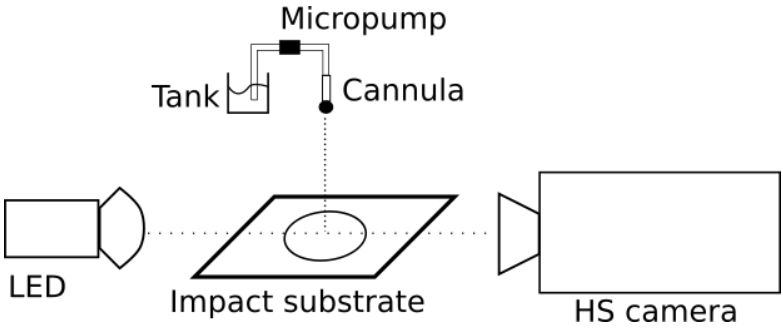

Figure 2.1: Scheme of the experimental setup: drop generator consisting of cannula, micro pump and tank, the observation system consisting of the high-speed camera (HS camera) and illumination source (LED), and impact substrate. Reprinted figure with permission from [92]. Copyright 2018 by the American Physical Society.

dependent on the cannula diameter d_c, on the surface tension σ as well as on the density ρ as shown in Eq. (2.1) [104].

$$D_0 = \sqrt[3]{\frac{6\sigma d_c}{\rho g}} \tag{2.1}$$

Therefore, the initial drop diameter varies in this study between: 1.45, 1.7 and 2 mm in the case of silicone oil/hexadecane droplets, 1.8, 2.4 and 2.8 mm in the case of water/water-urea solution droplets. Due to gravity the drop is accelerated and the impact velocity is determined by height difference between the cannula and the impact substrate. The following impact velocities are reached: 1.7 m/s, 2.8 m/s, 3 m/s and 3.2 m/s. The maximum measurement uncertainty of D_0 is $\pm$ 21.8 μm and of U_0 $\pm$ 0.048 m/s.

The micro pump *mp6*, or respectively *mp6-pp* (higher media compatibility), (*Bartels micro components*) is connected to a *mp-x* control unit and controlled by *LabVIEW* [12]. The principle of these micro pumps is based on a piezoelectric diaphragm combined with passive check valves. A piezo ceramic is mounted on a coated brass membrane. When voltage is applied, the piezo is deformed. The fluid is displaced out of the pump chamber from the resulting down stroke. Both used kinds of micro pumps are miniaturised double diaphragm pumps ran by two piezo actuators. Backflow valves between the micro pump and the cannula prevent the liquid to flow back when not in use [12].

2.1.2 Impact substrate

The impact substrate is a horizontal glass plate. A foil with a recess of a diameter of 60 mm is glued onto the glass plate in order to define a wall film of a given thickness. The unsealed area is used to create the wall film. In this study the film thickness is varied between 0.1 mm and 0.5 mm and is measured using a micrometer screw. First, the tip of the screw is lowered till it touches the glass substrate to determine the reference value. After the liquid is filled in the screw is lowered till it reaches the liquid surface. The difference of both values determines the film thickness. It is assured that an uniform film is generated. The impact substrate is located between the observation system.

Uncertainty of the measured film thickness Using a micrometer screw to measure the film thickness, special diligence of the user is required. The used micrometer screw has a resolution of 10 μm and the outer diameter of the measuring tip is 5 mm. The accuracy of the measurement depends highly on the diligence of the user. When the tip of the screw is coming closer to the surface of the wall film, the liquid is pulled upwards towards the tip at one point due to adhesion. Therefore, the tip needs to be lowered slowly and its distance to the surface is controlled by the high-speed camera. The systematical part of the measuring uncertainty is the uncertainty of the micrometer screw, the statistical part the diligence of the user, which is hard to quantify. Therefore, only the measurement uncertainty of the micrometer screw is considered yielding $\pm$ 5 μm in this case. The total measurement uncertainty is at least $\pm$ 5 μm.

2.1.3 Observation system

The observation system consists of a high-speed video camera and an illumination source. Three different high-speed cameras have been used in this study: Photron Fastcam SA1.1, Photron Fastcam SA-X2 in monochrome and in colour. The frame rate of the high-speed video camera is varied between 12500 and 50000 fps depending on the specific requirements of each experiment. The resulting resolution varies in a range from 576×480 px and 1024×1024 px and the shutter speed from 5 μs and 30 μs. The high-speed camera has been equipped with a 60 mm macro lens (Nikon AF NIKKOR 1:2.8 D). An aperture of 32 was used in order to gain a biggest possible depth of focus. Using this system a spatial resolution of 30μm/px has been achieved. A light-emitting diode (LED, Veritas Constellation 120E, 12,000 Lumen) is used as an illumination source. In front of the illumination source a diffusion screen is placed, yielding a uniform back lighting.

2.1.4 Test liquids

The physical properties of the liquids used in the experiments are shown in Table 2.1. In the case of water - silicone oil combinations the liquids are immiscible while the silicone oil - silicone oil combinations and the water - urea-water solution combinations are miscible. The temperature of the fluids has been measured using a thermocouple, type k. This study includes drop impacts with different liquids of drop and film as well as drop impacts of the same liquid. All fluids used in this study are Newtonian and have been purchased at *Sigma-Aldrich*.

2.1.4.1 Measurement of the fluid properties

In the case of silicone oil, kinematic viscosity ν and density ρ are reported in the safety sheet provided by *Sigma-Aldrich*. If the fluid properties are not available or dyes are added to the fluids, the properties are measured as described in the following. Each measurement is repeated at least 5 times.

Density The density ρ is measured by using a specific gravity bottle. The specific gravity bottle by *BLAUBRAND* got a measured volume of 5.0817 $cm^3 \pm 0.0100$ cm^3 referred to 20°C on the basis of ISO 4787 (Certificate of Performance). The liquid is filled into the gravity bottle and its weight is measured using a precision balance of *KERN*, PLS 1200-3A, with a reproducibility of 0.001 g. The measurement of the density is done at an ambient temperature of 22.5°C. The measurement uncertainty consists of a statistical and a systematical part. The statistical measurement uncertainty is calculated in Eq. (2.2) using the correction factor $t_p = 2.78$ for $n = 5$. This correction factor is necessary due to the sample size $n < 10$ [93].

$$\Delta\rho_{stat} = t_p \frac{s_\rho}{\sqrt{n}} \tag{2.2}$$

with the standard deviation s_ρ.

The systematical measurement uncertainty is calculated by the Gaussian propagation of uncertainty of the weight and the volume [93].

$$\Delta\rho_{sys} = \left.\frac{\partial\rho}{\partial m}\right|_{m_0} \Delta m + \left.\frac{\partial\rho}{\partial V}\right|_{V_0} \Delta V \tag{2.3}$$

The resulting propagation of uncertainty

$$\Delta\rho_{total} = \sqrt{\Delta\rho_{stat}^2 + \Delta\rho_{sys}^2} \tag{2.4}$$

The maximum measurement uncertainty is ± 3.7 kg/m^3.

Table 2.1: Fluid properties. W - for water, H - for hexadecane, Sxxx - for different silicone oils (xxx representing the kinematic viscosity), Uxx for different urea-water solutions and Gxx for different glycerine-water solutions (xx representing the respective urea or respectively glycerine water ratio in weight percentage), measured at 25 °C.

Fluid No.	Kinematic viscosity ν [mm^2/s]	Surface tension σ [mN/m]	Density ρ [kg/m^3]
W	1	72.2	997
H	4.11	27.61	769.15
S1	1	19.1	820
S5	5	17.72	920
S10	10	18.29	930
S20	20	18.2	945
S25	25	18.19	950
S50	50	18.69	960
S65	65	18.69	970
S350	350	18.56	972
S500	500	18.83	972
S750	750	18.78	970
S1000	1,000	18.59	972
S10000	10,000	18.81	972
S30000	30,000	18.81	972
S100000	100,000	18.81	972
AdBlue	1.27	64.89	1082
U10	1.1	68.5	1018
U20	1.16	66.5	1049
U30	1.27	65.5	1078
U40	1.42	64.1	1105
U50	1.72	63.5	1138
G5	1.38	68.0	1010.15
G10	1.47	67.0	1020.7
G20	1.72	61.0	1045.25
G30	2.33	60.0	1070.7
G40	3.37	55.0	1097.1
G50	5.34	55.0	1123.75
G90	177.76	53.0	1232

Viscosity The dynamic viscosity μ is measured by the cone/plate rheometer *BROOKFIELD DV-Ultra III+Ultra CP* at an ambient temperature of 22.5°C. The rheometer measures the shear stress at a defined shear rate using a torsional spring. The shear stress is applied on the fluid over a rotating plate. By twisting of the spring the shear stress can be determined. This precise torque measuring device is driven at rotational speeds and consists of a calibrated beryllium-copper spring which connects the drive mechanism to the rotating cone. The resistance to rotation is measured and is caused by the presence of the fluid between the cone and the flat plate. A torque proportional to the shear stress in the fluid is produced by this resistance. The viscosity can be obtained by either calculating from the known geometric constants of the cone, rotation rate and stress related torque or by converting to absolute centipoise units from pre-calculated range charts [24].

The accuracy is ±1.0% and the reproducibility is ±0.2%, whereas the temperature can be controlled in the range from 0° and 100°. The maximum measurement uncertainty for the dynamic viscosity is $\pm 0.5\,\mu\mathrm{m}^2/\mathrm{s}$. Exemplary, measurement results of different silicone oils show no dependency of the dynamic viscosity μ of the shear rate $\dot{\gamma}$ as shown in Fig. 2.2.
The kinematic viscosity ν is calculated using the measured values μ and ρ as shown in Eq. (2.5).

$$\nu = \frac{\mu}{\rho} \tag{2.5}$$

The resulting measurement uncertainty of the kinematic viscosity yields

$$s_\nu = \sqrt{\left(\left.\frac{\partial \nu}{\partial \rho}\right|_{\rho_0} s_\rho\right)^2 + \left(\left.\frac{\partial \nu}{\partial \mu}\right|_{\mu_0} s_\mu\right)^2} \tag{2.6}$$

with

$$\Delta\nu_{stat} = \sqrt{\frac{n-1}{n-3}}\frac{s_\nu}{\sqrt{n}} \tag{2.7}$$

and

$$\Delta\nu_{sys} = \left.\frac{\partial \nu}{\partial \rho}\right|_{\rho_0} \Delta\rho + \left.\frac{\partial \nu}{\partial \mu}\right|_{\mu_0} \Delta\mu. \tag{2.8}$$

The maximal measurement uncertainty is $\pm 0.63\,\mu\mathrm{m}^2/\mathrm{s}$.

Surface tension The surface tension σ is measured by the pendant drop method using an optical contact angle measurement and drop contour analysis device, *dataphysics OCA*.

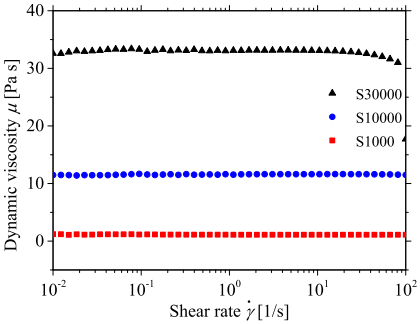

Figure 2.2: Dynamic viscosity μ of different silicone oils plotted over the shear rate $\dot{\gamma}$.

A pendant drop (generated by a dosage needle) is captured by a camera and its shape is analysed. The surface tension can be obtained by the hydrostatic pressure and the analysis of the curvature radii. The Young-Laplace equation is used for the analysis of the contour of the drop. The Young-Laplace equation, shown in Eq. (2.9), describes the pressure difference, also called the Laplace pressure, between the areas inside and outside of the curved fluid surface with the principle curvature radius R_i and the mean curvature $H_c = \frac{1}{2}\left(\frac{1}{R_1} + \frac{1}{R_2}\right)$.

$$\Delta P = (p_{int} - p_{ext}) = 2\sigma_{lf} H_c = \sigma\left(\frac{1}{R_1} + \frac{1}{R_2}\right) \tag{2.9}$$

The shape of the formed drop is mainly determined by surface tension and gravity force. The surface tension tries to minimise the surface area and consequently tries to form a sphere. The gravitational force stretches the drop to a pear body shape and causes a pressure gradient along the z axis of the drop according to the Pascal's law (hydrostatic pressure). This leads to following expression for the Laplace pressure $\Delta P(z)$:

$$\Delta P(z) = \Delta P_0 \pm \Delta\rho g z \tag{2.10}$$

At the pendant drop $R_1 = R_2 = R$ applies for the principle curvature radii at the apex. Therefore, the reference plane is set in this point leading to $\Delta P_0 = \sigma\frac{2}{R}$. At each point above the apex applies $R_2 = \frac{x}{\sin\Phi}$ as shown in Fig. 2.3. Resulting from the above shown equations it leads to:

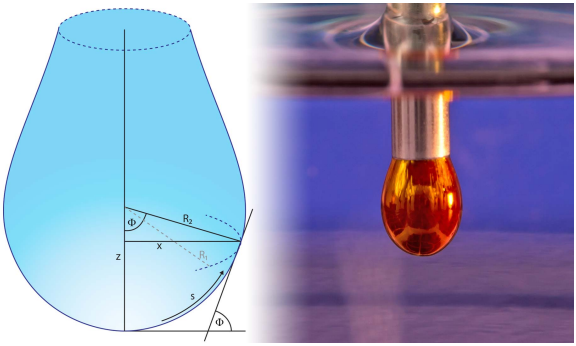

Figure 2.3: Schematic description of the Young Laplace equation of a pendant drop [47].

$$\frac{1}{R_1} + \frac{\sin\Phi}{x} = \frac{2}{R} \pm \frac{\Delta\rho g z}{\sigma} \tag{2.11}$$

Introducing of a parametrisation over the arc length s of the drop contour leads finally to following system of equations of three coupled first order differential equations with three boundary conditions, which can be solved numerically [47]:

$$\begin{aligned} \frac{d\Phi}{ds} &= -\frac{\sin\Phi}{x} + \frac{2}{R} \pm \frac{\Delta\rho g z}{\sigma} \\ \frac{dx}{ds} &= \cos\Phi \\ \frac{dz}{ds} &= \sin\Phi \\ 0 &= x(s=0) = z(s=0) = \Phi(s=0) \end{aligned} \tag{2.12}$$

The same approach can be used for the determination of the interfacial tension of two liquids.

Calculating the statistical and systematical measurement uncertainties the same approaches shown in Eq. (2.2) and Eq. (2.3) are used. The resulting maximum measurement uncertainty yields ±0.17 mN/m.

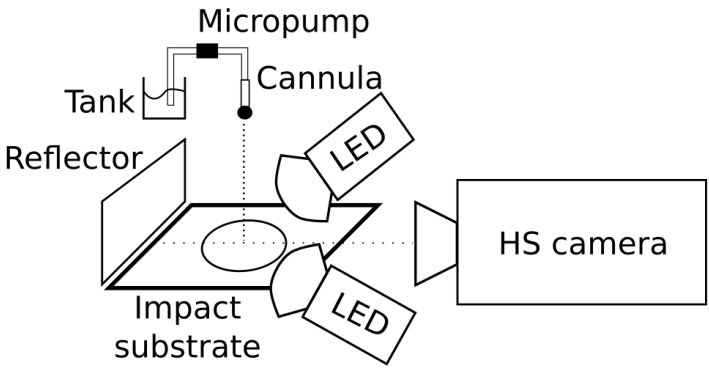

Figure 2.4: Scheme of the experimental setup: drop generator consisting of cannula, micro pump and tank, the observation system consisting of the high-speed camera (HS camera), two illumination sources (LED) and a reflecting white sheet, and impact substrate.

2.1.5 Experimental configuration for the impact of dyed drops

In order to investigate the impact of dyed drops, the experimental setup, described in Section 2.1, is adapted as shown in Fig. 2.4. In this case the observation system consists of a color high-speed video camera (Photron Fastcam SA-X2) and two illumination sources. The frame rate of the camera is set to 12 500 fps, with a resolution of 1024×560 px, and the shutter speed is set to 30 μs. The illumination sources are light-emitting diodes (LED, Veritas Constellation 120E, 12 000 Lumen). A reflecting white plate is placed as a background, reflecting the light of the LEDs to create an uniform illumination and avoiding glare points.

In order to delineate the interfaces of both liquids after the impact, dye is added to the fluid of the droplet. In this study, different dyes are used depending on the liquid of the drop. For water, Fuchsin is used with a concentration of 0.024 wt.%, in the case of glycerine, Bromphenol Blue with 0.1 wt.% and for silicone oil, 0.022 wt.% Sudan II. All dyed liquids were placed at least 15 minutes in an ultrasound bath and were filtered before use. The physical properties of the dyed liquids are given in Table 2.2.

Table 2.2: Fluid properties of the dyed liquids, measured at 25 °C.

Fluid No.	Fluid	Kinematic viscosity ν [mm^2/s]	Surface tension σ [mN/m]	Density ρ [kg/m^3]
FuW	Water w/ Fuchsin	0.953	70.2	998
BrGl	Glycerine w/ Bromphenol Blue	814.8	64	1251
SuS10	Silicone oil w/ Sudan II	10.1	18	931

2.1.6 Experimental configuration of drop impact onto a solid substrate coated by a thin soft layer

The same experimental setup described in Sec. 2.1 is used. A frame rate of 40 000 fps and a shutter time of 12.5 μs are used with a resolution of 768×480 px in this case. In this section two initial drop diameter of $D_{01} = 2.3$ mm and subsequently $D_{02} = 3$ mm are used. Deionized water and water-glycerin mixtures are used as liquids. The fluid properties can be found in Table 2.1. The impact velocity varies from $U_0 = 1.3$ m/s to $U_0 = 3.5$ m/s. The impact substrate is varied, glass and PDMS (polydimethylsiloxane) with different mixing ratios, which yield different rates of softness, are used. The images were then processed with a custom made *MATLAB* script in order to determine the height and the diameter of the spreading drop.

In order to generate the soft substrates, PDMS Sylgard 184 (*Dow Corning Corporation*) is linked with a base solution and the cross-linking agent and cured with heat. The base and the cross-linking agent are mixed at different ratios to obtain different rates of softness of the substrates. The pre-polymer and the cross-linking agent are mixed manually for 5 minutes under laboratory conditions and afterwards degassed in desiccator for 40 minutes. After degassing, 2 ml of the mixture was poured on quartz glass slides (GVB GmbH, Germany) of 20 mm × 20 mm × 1 mm. The glass slides were prior to coating cleaned with isopropyl alcohol (*Sigma-Aldrich*) and acetone (*Sigma-Aldrich*) and then dried by blowing nitrogen. The glass slides are then placed inside an oven at 80 °C for 12 hours. The glass slides were spin coated at 1000 rpm for 120 s in a spin coater (WS-400B-6NPP, Laurell, North Wales, USA).

Substrate characterization Soft PDMS is used for the fabrication of the substrate. The rate of cross-linking density determines the softness of the polymer [190].

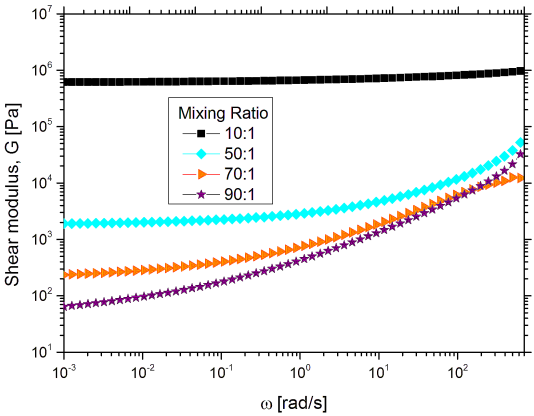

Figure 2.5: Complex shear modulus of the samples prepared with different monomer/cross-linking agent ratios. (Reprinted from [90].)

The thickness, surface wetting and rheological properties are determined. The thickness of the prepared PDMS layers has been measured using a scanning electron microscopy (*Phillips XL 30 FEG*) at the cross section. Since PDMS layers are non-conductive, gold was sputtered on top of the layers to facilitate the imaging. The samples were cut into two parts and SEM (scanning electron microscope) images were taken at the cross-section [2]. Advancing θ_{ad} and receding θ_{re} contact angles were measured with a Krüss Instrument (Model DSA 100). For the measurements, a water drop of 3 μl was created and then expanded to 10 μl at a rate of 0.4 μl/s. After this the water was sucked out of the drop at the same rate.

Rheological characterization of the samples used for this study was carried out with a strain controlled MCR 302 rheometer (Anton Paar, GmbH). The prepolymer and cross-linker mixture was placed between a 25 mm parallel plate with a gap in-between of 1 mm. The temperature of the lower plate was set at 80 °C. The curing was performed for 12 hours and after that, the temperature was set to 25 °C. All the frequency sweeps were conducted at 25 °C with 0.1% strain. The strain values were obtained with a strain sweep measurement of the samples and the value of the strain for the oscillation measurements was chosen in a manner that the strain is within the linear viscoelastic region. A detailed description and discussion of the rheology of the substrates can be found in [90].

Fig. 2.5 shows the complex shear modulus against the applied angular fre-

Table 2.3: Substrate thickness, wetting and elastic properties. The complex modulus of the substrates are shown at 1 Hz rheological frequency

Substrate Number	Mixing Ratio	Thickness [μm]	Contact angle θ_{ad}/θ_{re} [°]	Shear modulus G [kPa]
S1	10:1	40	116/95	703.43
S2	50:1	45	128/30	4.28
S3	70:1	45	-	1.14
S4	90:1	45	-	0.23

quency. Table 2.3 shows the thickness, the contact angles, θ_{ad},θ_{re}, measured using water, and the shear modulus of the substrates at 1 Hz.

2.1.7 Experimental configuration for the observation from below

In order to observe the drop impact from below and sideways simultaneously, two high-speed cameras are used. Additionally to the experimental setup in Section 2.1 a further high-speed camera is added to the setup as shown in Fig. 2.6. For the observation from below a second high-speed camera is placed below the impact substrate orthogonally. The LED is placed over the top of the cannula. In order to generate a homogenous background a diffusing plate is placed right underneath the cannula. In this diffusing plate a hole is thrilled just big enough to let the drop pass through. Nevertheless, small shadows from connecting tube and cannula can be observed in the images. As impact substrate anti-reflection coated high efficiency glass are used to minimise reflectance.

2.2 Experimental setup for the drop impact on an inclined substrate

Additionally to the previous described setup, the impact substrate wetted by the wall film is inclined as shown in Fig. 2.7. The frame rate of the high-speed video camera is set in this case to 22 500 fps with a resulting resolution of 1024× 600 px and the shutter time is set to 5μs. The high-speed camera has been equipped with a 100 mm macro lens (Tokina MACRO 100 F2.8D). An aperture of 32 was used in order to gain a big depth of focus. Using this system a spatial resolution of 31μm/px can been achieved.

The physical properties of the fluids can be found in Table 2.1.

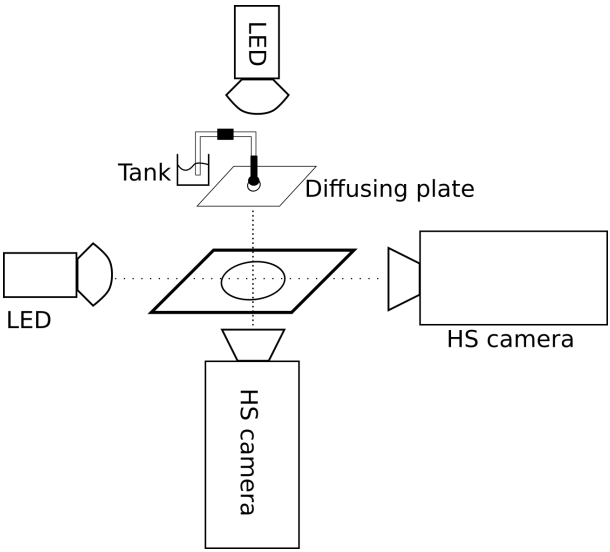

Figure 2.6: Scheme of the experimental setup: drop generator consisting of cannula, micro pump and tank, the observation system consisting of two high-speed cameras (HS camera), two illumination sources (LED) and diffusing plate, and impact substrate

2.2.1 Generation of the flowing wall film

The impact substrate is a sapphire glass plate. To generate a wall film, a special designed film generating unit is used as shown in Fig. 2.8. This film generating unit is 3D sintered. A pump transports the fluid from a tank to the container of the film generating unit. The liquid is retained until the container is completely filled. Afterwards, the liquid flows over an edge through a gap onto the impact substrate. Since only water-based fluids are studied in this case, the fluid wets the sapphire glass plate only in rivulets. In order to create a stable, homogenous wall film, two filaments are spanned downstream bounding the future wall film. Using a small plate, the fluid is spread until it reaches the filaments. When the filaments are completely wetted, the fluid builds a wall film. The film thickness is set by the mass flow of the pump in combination with the angle of inclination.

The film thickness is varied from 0.1 mm and 0.5 mm. The angle of inclination α_{incl} is varied in a range of 10° till 60°.

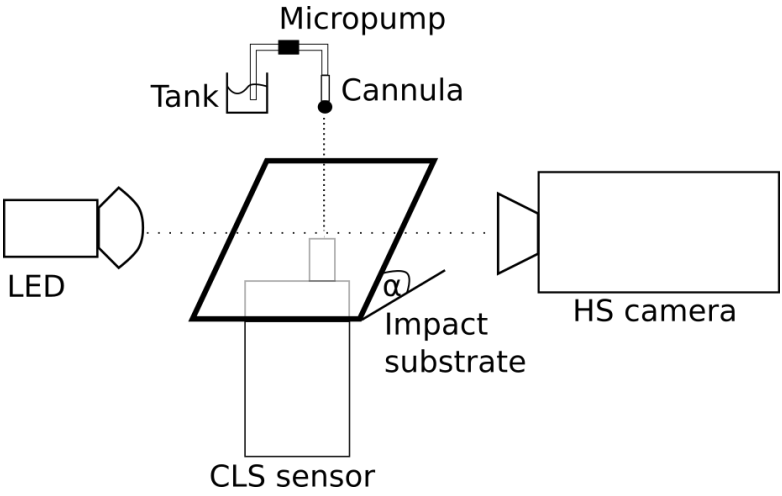

Figure 2.7: Scheme of the experimental setup: drop generator consisting of cannula, micro pump and tank, the observation system consisting of the high-speed camera (HS camera) and illumination source (LED), and inclined impact substrate (with inclination angle α) including the confocal chromatic line sensor (CLS).

2.2.1.1 Measurement of the film thickness

In order the measure the film thickness during the experiments, a chromatic confocal line scan sensor, *Precitec CHRocodile CLS*, is used. The measurement technique is explained in Section 2.3.2. The sensor is placed orthogonal under the impact substrate and measures the film thickness simultaneously at 192 points on a line of 1.91 mm with a frequency of 200 Hz. The measurable range of film thickness of the optical head *CLS1*, which is used in this study, is between 75μm and 1.35 mm with a axial resolution of 200 nm. Exemplary, Fig. 2.9 (a) shows the temporal evolution of the mean film thickness $h = 200\mu$m during the drop impact at $t = 5$ s. This experimental setup has been used to validate a newly developed absorption based laser sensor as reported in [160]. It can be seen in Fig. 2.9 (b) that the film thickness is rather homogenous at the drop impact point over the complete 192 measuring points.

Uncertainty of the measured film thickness The maximum measurement uncertainty of the mean film thickness, which is averaged over all 192 channels,

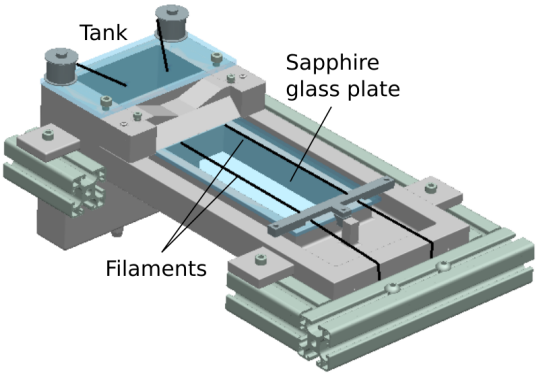

Figure 2.8: CAD image of the wall film generator with the filaments, which are bounding the wall film.

for $h = 200$ μm is 2.5 μm yielding a uncertainty of 1.25 %. This uncertainty was approximately observed for all film thicknesses. Using a chromatic confocal line scan sensor allows a better reproducibility and smaller uncertainty.

2.2.2 Computer control unit

A computer control unit is used for controlling the experiment and data acquisition. All components of the experimental setup are connected to the computer and controlled by using *LabVIEW*. A specifically developed *LabVIEW* script is used for controlling of the experimental procedure. For each experiment images are obtained and stored by using the high-speed camera and a *TDMS*-file containing following information is stored:

- Date and time
- Temperature of drop and wall film in ° C
- Inclination angle in degree
- Film flow data consisting of density and volume flow rate of the pump
- Wall film thickness data consisting of averaged film thickness, derivation, raw data of the film thickness of each of the 192 channels of the *CHRocodile CLS* sensor for each time step

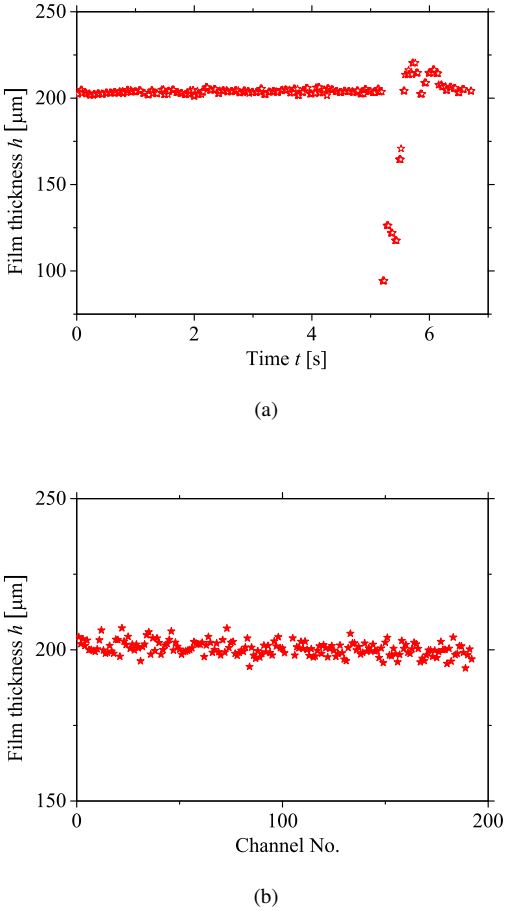

Figure 2.9: Temporal evolution of the mean film thickness $h = 200\mu$m during the drop impact at $t = 5$ s (a). Instantaneous film thickness measurement of each channel (total number of channels 192) of $h = 200\mu$m (b).

Finally, the obtained images are post-processed by using *MATLAB*, which is described more in detail in Section 2.3.1.

2.3 Measurement technique principles

In this section, the measurement techniques used in this study are described and discussed. Shadowgraphy is used to capture the dynamics of drop impact, confocal chromatic imaging is used to measure the film thickness.

2.3.1 High-speed imaging and shadowgraphy

High speed imaging allows the direct imaging and observation of the drop impact process. The process of drop impact occurs rather fast. Starting from the initial impact velocity of at least $U_0 = 1$ m/s, the complete drop impact process takes only a few milliseconds. Resulting secondary droplets are rather small in size due the initial minimum drop diameter of $D_0 = 1.45$ mm. In order to capture all necessary details the temporal as well as the spatial resolution need to be rather high. Therefore, a high speed imaging system is used to satisfy both requirements as good as possible.

Five issues need to be considered in setting up a high-speed imaging system [201]:

- Sensitivity/Contrast
- Spatial resolution
- Depth of field (DOF)
- Field of view (FOV)
- Temporal resolution/Motion blur

The illumination of an object can be either done by front illumination as shown in Fig. 2.4 or by back illumination as shown in Fig. 2.1 . In case of front illumination, the light source is placed in front of the object and the light is reflected by the object on the camera sensor. This type of illumination is common in photography and is used to visualize colours. If the light source is placed behind the object, the image on the camera sensor is related to the shadow of the image. This shadow forms a big contrast to the bright light from the illumination system. This contrast enables the precise detection of the geometry of the drop impact phenomena. This type of illumination is called *shadowgraphy* [176].

Table 2.4: Specifications of high-speed cameras.

Camera	Sensitivity (ISO)	Bit	Electronic shutter [μs]	Pixel size [μm]	Spatial resolution [px]	Frame rate [fps]
Photron SA1.1	10 000	12	1	20	1024×1024	5 400
Photron SA-X2	25 000	12	0.293	20	1024×1024	12 500
Photron SA-X2C	10 000	36	0.293	20	1024×1024	12 500

The brightness depends on the frame rate and illumination in high-speed imaging. With increasing frame rate, the time of collecting photons on the sensor decreases and therefore the images are less bright.

Sensitivity/Contrast Each application determines the choice of type of camera, CCD (charged coupled device) or CMOS (complementary metaloxide semiconductor) camera, due to its specific requirement. In case of visualizing of drop impact dynamics the CMOS cameras provides a higher frame rate, while CCD cameras obtain a higher image quality. Since the frame rate depends on the readout, smaller images lead to higher frame rates. By decreasing the spatial resolution higher frame rates can be achieved [201]. Therefore, in most cases compromises between temporal and spatial resolution need to be found. An overview of different imaging techniques for hydrodynamic application can be found in [173]. The specifications of the cameras used in this study can be found in Table 2.4.

Spatial resolution The spatial resolution of the system determines the minimum size of the objects to be investigated. The optical lens determines the spatial resolution, but the possible working distance provided by the experimental setup and the sensor size of the camera determine the choice of the optical lens. Therefore, compromises are often indispensable and magnification and diffraction limit need to be considered.

The Gaussian thin lens formula describes, that if the condition

$$\frac{1}{s_0} + \frac{1}{s_i} = \frac{1}{f} \tag{2.13}$$

is satisfied, the image is in focus with the focal length f. For this system the transversal magnification yields

$$M_T = \frac{y_i}{y_0} = \frac{s_i}{s_0} = -\frac{x_i}{f} = -\frac{f}{x_0} \tag{2.14}$$

and the longitudinal magnification

$$M_L = \frac{dx_i}{dx_0} = -\frac{f^2}{x_0^2} = -M_T^2. \tag{2.15}$$

The diffraction limit limits the spatial resolution. The resolving capacity describes the minimum distance of two points that can be resolved from the optical system. This is called the Frauenhofer diffraction. The diffraction arises from light passing a small circular aperture and describes the physical resolution limit of a lens [75, 138]. The diffraction results in a diffraction pattern instead of a point on the camera sensor. The maximum intensity peak of this pattern the well-known Airy disk and is given by

$$D_s = 1.22\frac{R\lambda}{2a} \tag{2.16}$$

with the wavelength of light λ. The *diffraction limited spot* contains 84 % of the light and is the central intensity peak. D_s yields to

$$D_s = 1.22\lambda f^{\#} = 1.22\lambda/\mathrm{NA} \tag{2.17}$$

with $f^{\#} = f/2a$ and the numerical aperture NA, if the distance R is approximated with f. D_s is the minimum diameter on the image plane, independent of the size of the object on the object plane $\sum$.

According to the Rayleigh criterion two objects are no longer resolvable, if they are too close to each other, that their Airy disks become closer than half their width. The Rayleigh criterion determines the resolution limit and is independent of the available pixel number of the sensor. This condition defines the resolving capacity.

The Airy disk should not be smaller than one pixel, which determines the choice of magnification. As shown in Eq. (2.16) the spatial resolution can be improved by increasing the diameter of the focusing lens, reducing R or $f^{\#}$ and increasing NA [201].

Therefore, a higher resolution of the camera cannot improve the spatial resolution if pixel size and resolving capacity are identical [23].

Depth of Field The depth of field quantitatively defines the observation volume and is defined as the forward and backward area surrounding the focal plane until

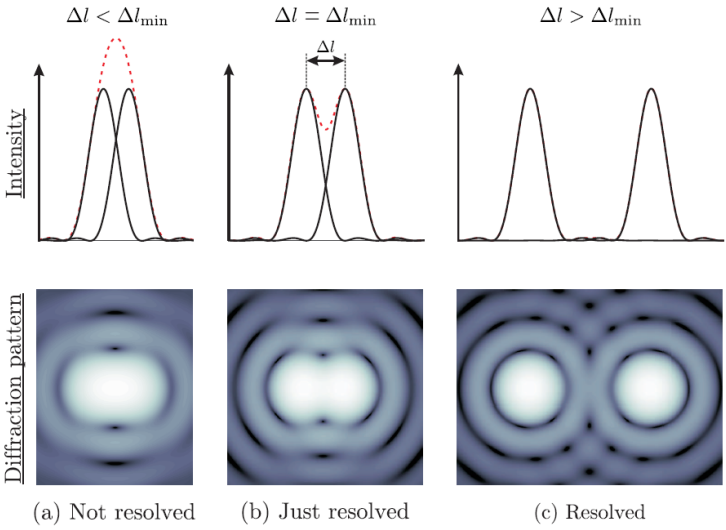

Figure 2.10: Airy pattern of two point sources at different distances: (a) both points are closer than the resolving capacity, (b) both points are equal to the resolving capacity and (c) both points are further away than the resolving capacity [23].

the loss of sharpness is not negligible anymore. The depth of field strongly depends on the optical aperture consisting of focal length and f-number.

The depth of field can be described as the distance between two points with acceptable sharpness. The circle of confusion c is used to quantify the depth of field. The *circle of confusion* is defined as the minimum loss of sharpness noticeable for the human eye and is given by [29]

$$c = \frac{\text{inch}}{1000} = 0.0254\text{mm}. \tag{2.18}$$

Usually a circle of confusion is set to 0.25 mm. The depth of field can be obtained by

$$\text{DOF} = 2c\frac{f}{D}\left(\frac{\text{M}_T + 1}{\text{M}_T^2}\right) \tag{2.19}$$

with f as focal length of the lens, M_T the magnification of the optical system, D the lens diameter and c the *circle of confusion*. DOF can be increased by decrea-

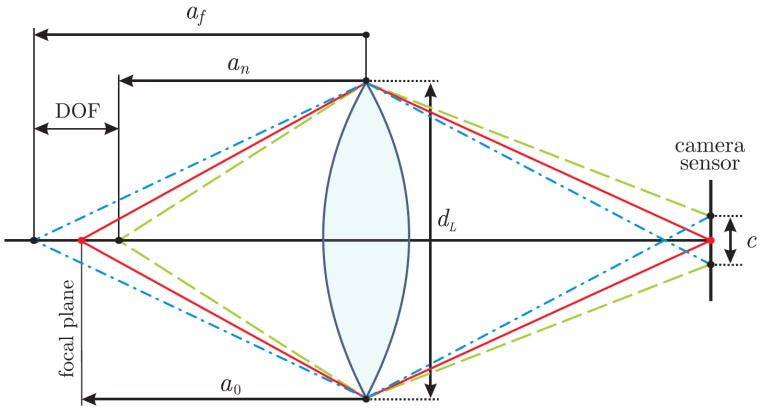

Figure 2.11: Schematic illustration of the ray diagram of the depth of field for a symmetrical lens [23].

sing the numerical aperture leading to a decrease of light intensity. Increasing the magnification leads to a decrease of DOF [201].

DOF can also be approximately expressed by [201]

$$\mathrm{DOF} \approx 4\lambda \left(1 + \frac{1}{\mathrm{M}_T}\right)^2 f^{\#2}. \tag{2.20}$$

The depth of field for the system used in this study is determined experimentally using a DOF target (*Edmund optics DOF 5-15*). The measuring surface of the target is angled at 45° and shows a millimeter scale. Exemplary, an image taken by the observation system is shown in Fig. 2.12(a). This image is analysed to determine the depth of field. The intensity profile is determined along the scale marked in Fig. 2.12(b). The depth of field can be estimated from the intensity profile shown in Fig. 2.12 and yields DOF ≈ 10 mm.

Field of View The field of view depends on the magnification and the working distance. An increasing magnification in combination with a shorter working distance lead to a smaller field of view. The field of view in this study is chosen to satisfy at least a 18 mm × 15 mm optical observation area.

Temporal resolution/Motion blur The temporal resolution depends on two aspects, motion blur, which should be minimised, and the necessary frame rate

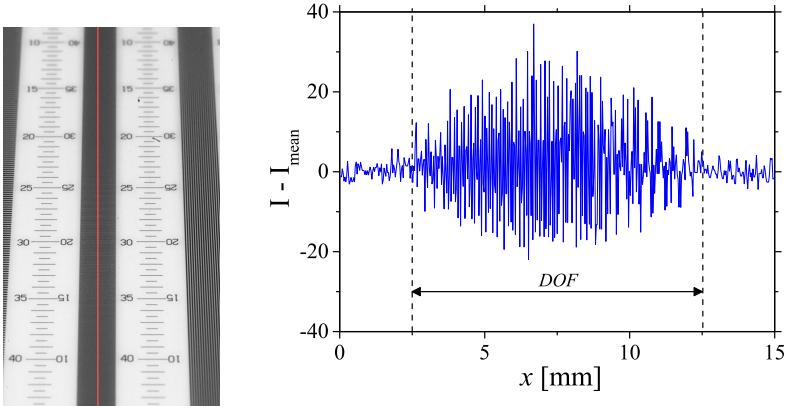

(a) (b)

Figure 2.12: Experimental determination of the depth of field using the DOF target (a) and the analysis of the intensity profile along the marked line (b).

resolving the dynamic process. Motion blur occurs if the moving object is blurred, although it is in focus. That means, that the motion of the object is captured by the blur.

In theory, an infinitesimally small exposure time is used for obtaining images, whereas in reality the used exposure time determines the motion blur. The energy is integrated over the pixel area (spatial resolution) and exposure time (temporal evolution). That means that the image is taken over a finite amount of time. The energy is averaged, when the aperture is open for a specific time window. Due to this averaging objects of different speeds result in different kinds of blur. Using the assumption of diffuse reflection spatial properties like shape and motion can be recovered by the analysis of the images. Motion blur is just about insignificant, if the motion of the object is less than one pixel during a time sequence. Time limited illumination and short shutter speed can be used to minimise motion blur [54, 201].

In these experiments, a continuous light source is used and the exposure time of the camera is adapted for each kind of experiment. The exposure time varies between 5 μs and 30 μs depending on the setup conditions.

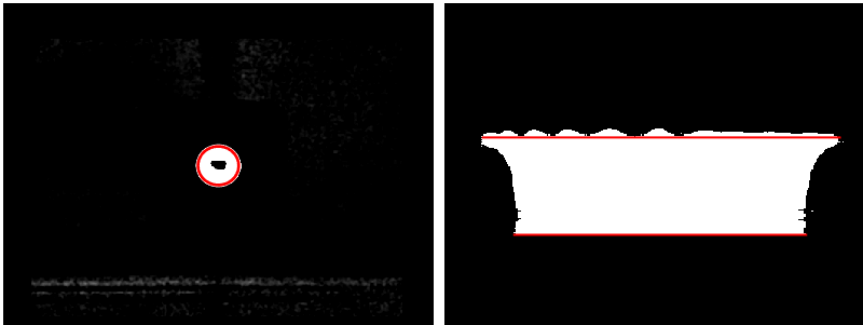

Figure 2.13: Binarized images showing the detection of the drop (left) and of the corona (right).

Image post processing In order to determine the characteristic parameters such as initial drop diameter D_0 in each experiment, the captured images need to be analysed. Therefore, the obtained images are post processed by using the software *MATLAB*. Custom made codes are used to analyse following desired parameters:

- Inital drop diameter D_0
- Impact velocity U_0
- Temporal evolution of the corona: corona base diameter D_B, corona height H and corona rim diameter D_C
- Number of secondary droplets N_{sec} and content distribution

The post processing algorithm is briefly described in the following. For each experiment a reference image (before the initial drops enters the field of view) is taken. This reference images is subtracted from all images of its experimental set to remove noise. The grey scale images are converted into binary images, based on a defined threshold. Finally, the shape of the initial drop can be detected. The average of at least 15 images are used for the determination of D_0 and U_0. The center of the drop is determined. From the center of the drop, the radius and the velocity of the drop (over the time displacement) are obtained. In order to analyse the corona, geometry the geometry is detected and filled with pixels. The reflection of the wall film is removed and finally, the corona geometry is analysed.

The trajectories pictured in Fig. 2.14 were computed considering some validation criteria. From one frame to the next, a sequential image of a droplet was only

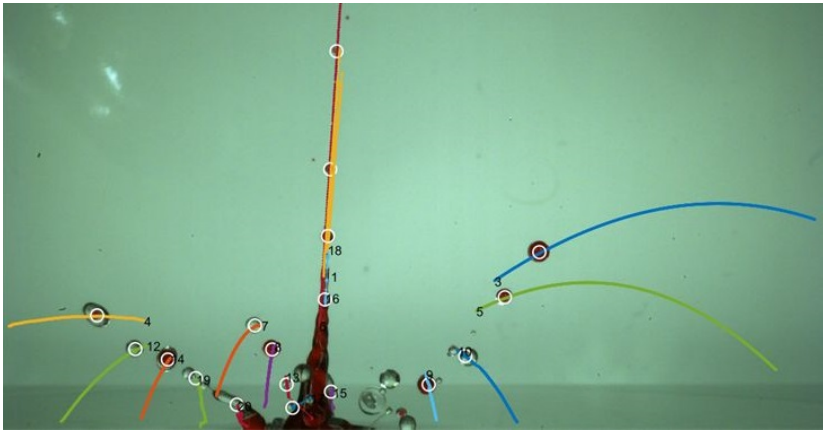

Figure 2.14: Trajectories of splashed secondary droplets.

validated if the midpoint of the drop did not move more than four pixels, the *s*hape does not change more than 0.5 and the projected area does not change by more than 30%. If more than 10 images in one trajectory are available, then this *a* priori data is used to forecast the next position. The next droplet image must lie within two pixels of the forecasted position. The trajectories are used to determine the total number of secondary droplets as well as their size, velocity and dye content in case of dyed droplets.

Colour high-speed imaging In comparison to the monochrome high-speed camera the colour high-speed camera provides 36 bit and the obtained images contain additional information. The colour information is stored in the *RGB* colour model in a 3×3 array. In Chapter 7 the content of secondary droplets is investigated using dyed drop liquids. Therefore, the specific colour of the dyed liquids needs to be detected during the post processing algorithm. Considering exemplary a droplet consisting of a transparent and a dyed liquid which are immiscible. Only the drop is detected, the background is already subtracted. Each pixel is analysed regarding its value of *hue*. The centrum of the *HSI* colour system (*Hue, Saturation, Intensity*) is the white point. Using a polar coordinate system the angle is proportional to the hue, the radius is proportional to the saturation and the height to the intensity [80, 192] as shown in Fig. 2.15.

Grey scale values as well as black and white are not included in the *HSI* colour system. The colour *red*, which is used in most experiments, is described by the

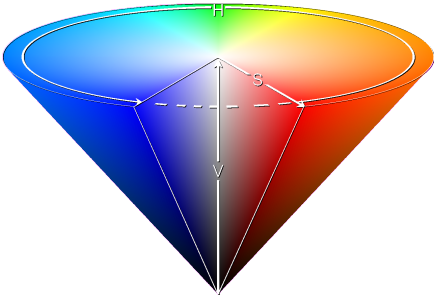

Figure 2.15: The cone of the *HSI* colour system with the hue **H**, the saturation **S** and the intensity **V** [25].

colour angle $0° < 60°$ and $300° > 360°$ corresponding to the values $0 - 0.1665$ and $0.8335 - 1$ in *MATLAB*.

Refraction of light at a two-phase drop Determining the *droplet in droplet* volume requires the consideration of the law of refraction. Beams of light are refracted at the surface of the drop at the transition if the refraction index of drop and surrounding medium are different. This refraction is described by the Snell's law of refraction shown in Fig. 2.16 [176].

$$n_1 \sin \alpha_1 = n_2 \sin \alpha_2 \tag{2.21}$$

with the corresponding refraction index n and entrance/exit angle α. If the beam is coming from the medium of the lower n For $n_1 < n_2$ Snell's law yields $\sin \alpha_1 > \sin \alpha_2$ and therefore $\alpha_1 > \alpha_2$ and vice versa [75].

2.3.2 Confocal chromatic imaging

White light is emitted from the optical head of the chromatic sensor. This optical head shows the longitudinal chromatic aberration. Using a very small pinhole aperture with a diameter of only a few micrometer yield a white spot light source. This light source is focussed with a lens with the chromatic aberration on the substrate. The emitted light of different wavelengths is focused on the substrate. Depending on the substrate, only one certain wavelength is focused. Each focus point covers only a diameter of a few μm. The light is reflected by the substrate and is received by a spectrometer. The intensity profile shows a clear peak for

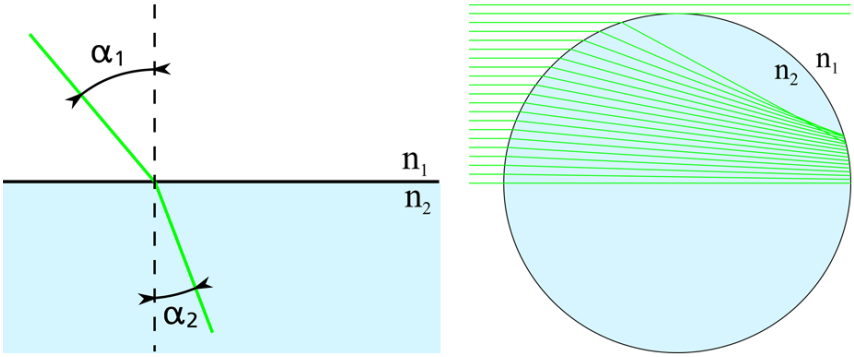

Figure 2.16: Scheme of Snell's law with the refraction indices n_1 and n_2 and refraction angles α_1 and α_2 and the diffraction of light in a drop.

the focused wavelength as shown schematically in Fig. 2.17. Due to the reflected wavelength the distance or respectively the thickness can be determined extremely precisely. Two wavelengths are reflected from both surfaces of the thickness. Each peak corresponds to one specific wavelength. Considering the refraction index of the material the thickness of the subject can be determined. Using the line sensor *Precitec CHRocodile CLS* 192 measuring points on a line are used simultaneously. Measuring the thickness of a material two peaks are found in the intensity profile. This measurement principle uses two characteristics [141].

Chromatic aberration This method uses an optical error of a lens, which is known as the axial chromatic aberration. The focal length f of a lens depends also on the refraction index of the glass and therefore, f is also a function of the wavelength. Different wavelengths of the light are focused at different focal points. In the case of white light the colours *violet* (λ_{min}) and *red* (λ_{max}) describe both ends of the visible spectrum. All colours, and respectively wavelength, which are in between *violet* and *red*, are focused between these two focal points. Consequently, the distance of lens and image differs for different wavelengths leading to different magnifications [138, 141]. Using this optical error, the distance from the optical head to the substrate can be determined.

Confocality A confocal optical system uses an illumination point source and a pinhole. The pinhole is located at the confocal point and allows only light which is from the focal point to pass through the detector. Therefore, the pinhole acts as

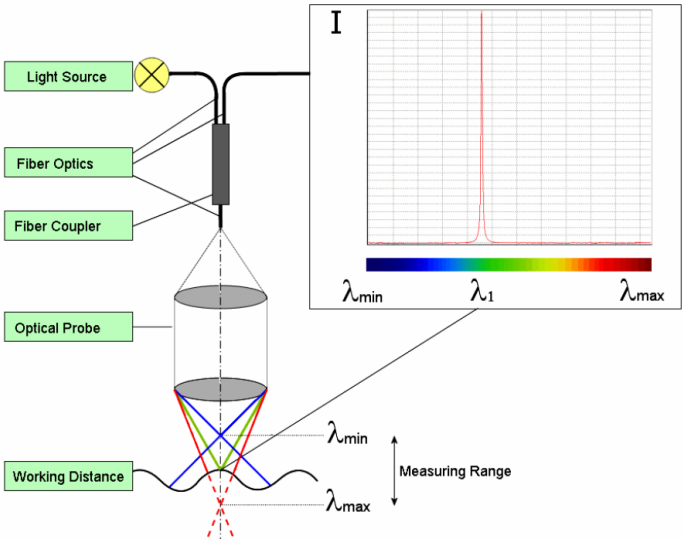

Figure 2.17: Measurement principle of the confocal chromatic imaging for the distance measurement [141].

a spatial filter blocking light which is out of focus or light from an external light source. This spatial filtering improves the lateral and axial resolution [141, 178].

3 Phenomena of normal drop impact with and without corona

In this chapter the various phenomena of drop impact under different conditions are shown. Section 3.1 focuses on the different impact outcomes and the influencing parameters. A qualitative description of the different outcomes and parameters is given. Section 3.2 focuses on the drop spreading and receding resulting from drop impact onto high viscous wall films and soft substrates. In Section 3.3 the evolution of the corona is discussed. Parts of this chapter have been published in [89, 92]. Furthermore, parts of the experimental investigations have been described in the thesis of Brulin [26].

3.1 Different outcomes of drop impact

Drop impact can lead to several outcomes. Among them deposition, corona, splash and partial rebound. The phenomena observed in this study are shown and discussed in the following. The experimental method is described in Chapter 2.1.

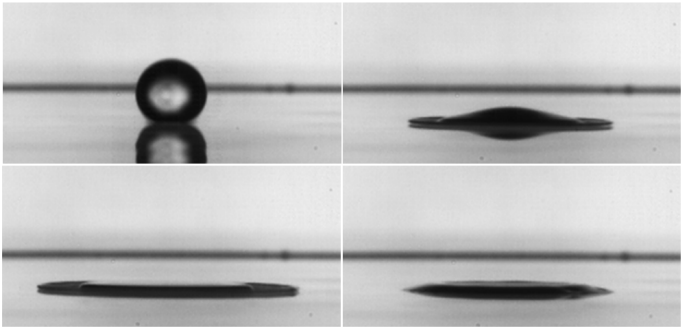

Figure 3.1: Temporal evolution of the impact outcome deposition: S20 drop impacting onto a S750 film with $\kappa = 37.5$, $U_0 = 3$ m/s, $D_0 = 1.4$ mm and $h = 0.1$ mm.

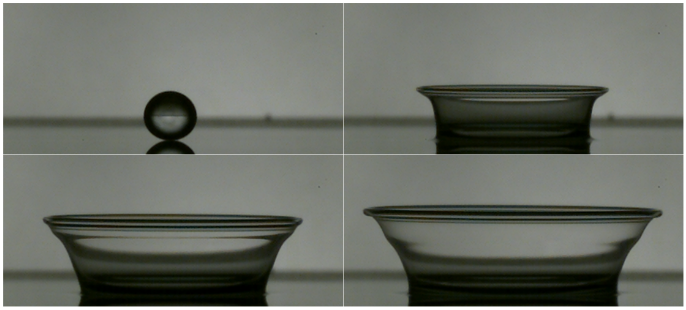

Figure 3.2: Temporal evolution of the impact outcome corona: S20 drop impacting onto a S20 film with $\kappa = 1$, $U_0 = 3$ m/s, $D_0 = 2$ mm and $h = 0.5$ mm.

Deposition In the case of deposition the impacting drop spreads on the wetted wall comparable to a dry wall and forms a disk-like shape as shown in Fig. 3.1. The wall film is uninfluential, no corona is build. Nevertheless, secondary droplets can be produced if the rim gets unstable. This phenomenon is discussed in more detail for drop impacts on soft substrates in Section 5.2.

Corona After the impact the droplet generates an expanding flow in the lamella. Drop impact onto a thin film leads to a kinematic discontinuity as described in Section 1.3.3. Its interaction with the outer film leads to the appearance of the uprising liquid sheet bounded by a Taylor rim. The corona grows in diameter and height till a maximum corona diameter is reached and the corona starts to collapse. This expansion of the corona is dependent on inertia and viscous forces. The rim bounding the free liquid sheet may show some instabilities, but no formation of secondary droplets in this case.

Splash Two kinds of splashing have been observed: prompt splash and corona splash. In the case of prompt splash directly after the drop impact, in the jetting phase, very fine secondary droplets are produced and can be observed for low Ohnesorge numbers. The corona splash can be observed for high Ohnesorge numbers. First a corona is build as described and shown in the previous paragraph. In this case the rim of the fully developed corona gets unstable and finger like jets are generated. Finally, secondary droplets detach from these jets. Splashing can be divided into four stages: corona formation, rim instability and jet formation, break up of the jets and formation of secondary droplets and collapse of the corona [42]. The different stages are shown in Fig. 3.3.

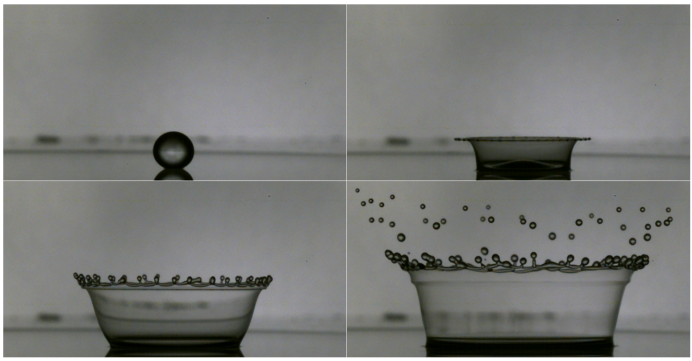

Figure 3.3: Temporal evolution of the impact outcome splash: S5 drop impacting onto a S5 film with $\kappa = 1$, $U_0 = 3$ m/s, $D_0 = 2$ mm and $h = 0.25$ mm.

Partial rebound In Fig. 3.4 the temporal evolution of partial rebound is shown. The corona rises, the generation of secondary droplets is possible, but not necessary. After the corona is collapsed the liquid merges back to the center of impact and rebounds in form of a central jet. If the energy is high enough, satellite droplets can detach from the central jet.

3.1.1 Influencing parameters on the impact outcome

Drop impact onto a liquid wall film results in a radially spreading lamella of the fluid of the droplet in a crater formed in the wall film. The resulting crown diameter and height as well as the impact phenomenon itself are highly influenced by many parameters like the impact velocity, the fluid viscosity and the surface tension, for example, a higher viscosity slows down the spreading of the droplet after the impact compared with a fluid with lower viscosity. In the case of different fluids as droplets and as wall films, investigated in this study, the influence of the fluid properties is even more complex. In order to understand the influence on the impact outcome of the parameters, each parameter is varied systematically. The influencing parameters are divided into the impact parameters (initial drop diameter D_0, impact velocity U_0 and film thickness h) and fluid properties of both liquids (kinematic viscosity ν, surface tension σ and density ρ), among which the focus is on the kinematic viscosity in this study.

Initial drop diameter The influence of the drop diameter on the impact outcome is shown in Fig. 3.5. A larger drop enhances splashing due to the higher

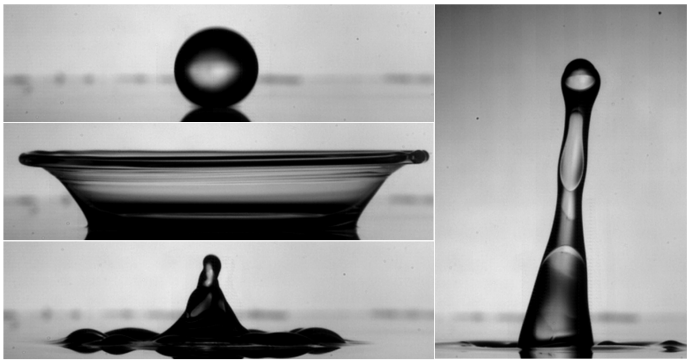

Figure 3.4: Temporal evolution of the impact outcome partial rebound: A water drop impacting onto a S65 film with $\kappa = 65$, $U_0 = 2.7$ m/s, $D_0 = 2.8$ mm and $h = 0.25$ mm.

kinetic energy at impact due to a bigger initial drop.

Impact velocity As shown in Fig. 3.6 the impact velocity also enhances splashing. The impact velocity has a significant influence on the impact phenomena, as expected. In the case of the lower impact velocity no splashing occurs. The crown is elevated and then falls down on the wall. After expanding the crater starts to recede due the action of capillary forces and gravity. Crater then merges and its implosion leads the generation of a central jet and partial rebound. In the case of higher impact velocity the crone instability leads to splash. The central jet is much weaker, than in the case with smaller impact velocity. This can be explained that splashing consumes the kinetic energy to an extent that the remaining kinetic energy for rebound is minor compared to the case of no splashing.

Film thickness The influence of the film thickness on the impact outcome in the regime of thin films ($\delta < 1$) is not as strong. As shown in Fig. 3.7, the impact outcome is comparable for different film thicknesses. Also the differences in the corona diameters and heights are minor compared to the effect of D_0 and U_0. Nevertheless, the wall film can also influence the impact outcome. In total thicker wall films can prevent splashing. Especially, in the very thin wall film regime a new phenomenon was observed, *corona detachment*, which is discussed in Chapter 6.

In Fedorchenko and Wang [55] the angle β of the corona inclination to the target

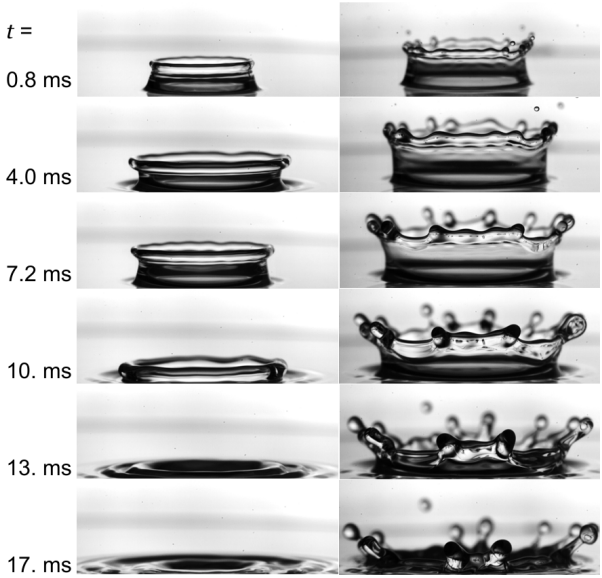

Figure 3.5: Drop size influence on corona development: S65 drop impacting onto a water film with $\kappa = 0.015$, $U_0 = 2.3$ m/s and $h = 0.5$ mm. Drop diameter is $D_0 = 1.8$ mm (left) and 2.2 mm (right) resulting in dimensionless film thicknesses of $\delta = 0.28$ and 0.23. Reprinted figure with permission from [92]. Copyright 2018 by the American Physical Society.

plane is predicted in the form

$$\cos\beta = 1 - 4\delta. \tag{3.1}$$

However, in this study the observed angle of the corona inclination is about $\beta \approx 80°$ for all three film thicknesses in Fig. 3.7 during corona propagation ($t = 2 - 5$ ms), which differs significantly from the prediction given in Eq.(3.1).

Apart from the aforementioned impact parameters, inclination of the substrate also plays a role. Inclination leads to a asymmetric propagation of the corona. The effect of inclination on the drop impact is discussed in the following Chapter 4.

Fluid viscosity The viscosity also influences the impact outcome as shown in Fig. 3.8 and Fig. 3.9. The increment in the viscosity slows down the motion of

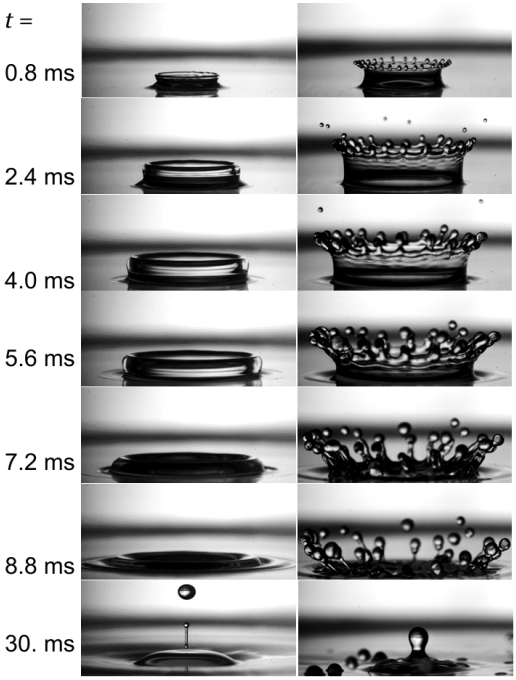

Figure 3.6: Impact velocity influence on corona development: water drop ($D_0 = 2$ mm) impacting onto a S10 film with $h = 0.5$ mm and $\kappa = 9.9$. Impact velocity is $U_0 = 1.7$ m/s (left) and 2.3 m/s (right). Reprinted figure with permission from [92]. Copyright 2018 by the American Physical Society.

the crown in the lamella and stops the expansion of the corona in the wall film. Prompt splash can be observed for low viscosity liquids due to the jetting flow in the lamella. On dry surfaces a shock wave propagates into the apex of the drop after its impact. When this shock wave reaches the contact point of drop and surface, an expanding wave is generated leading to the jetting flow. This jetting flow also occurs in drop impact onto thin films [42]. For high viscous liquids only corona splash can be observed.

If different fluids are used for the drop and wall film, then one can expect that the properties of both fluids must be considered when discussing their influence on the outcome. However, not only the fluid properties are important, but also which liquid is used for the drop or wall film is important, as can be seen in Fig. 3.8. The

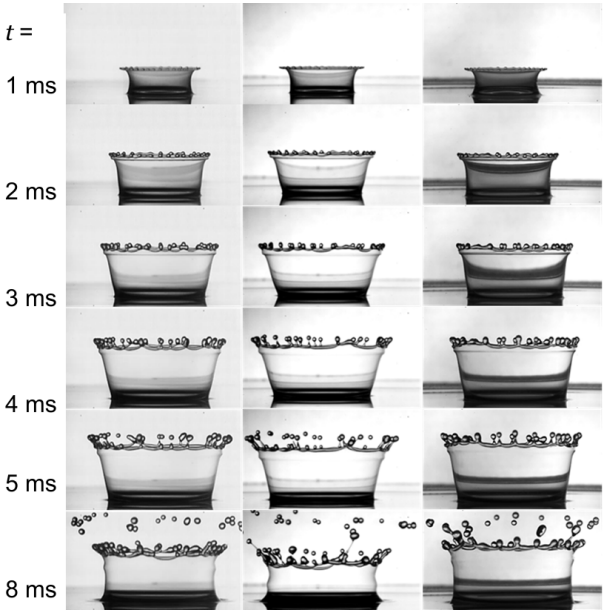

Figure 3.7: Film thickness influence on the corona development: A S5 drop impacting onto a S10 wall film with from left to right $\delta = 0.04$, 0.11 and 0.23. The impact velocity is $U_0 = 3.2$ m/s, the drop diameter $D_0 = 2.2$ mm and the viscosity ratio $\kappa = 0.5$. Reprinted figure with permission from [92]. Copyright 2018 by the American Physical Society.

impact outcome as well as the temporal evolution of the corona are strongly determined by which liquid is used for the drop and which for the wall film. With increasing viscosity of the wall film the corona evolution becomes slower due to the increasing resistance force of the wall liquid. Conversely, a less viscous wall film yields more easily and promotes the evolution of the corona. Therefore, corona splash occurs more readily in the case of a less viscous wall film. The influence of the drop viscosity is not as obvious.

Fig. 3.9 shows the impact outcome for different viscosity ratios. It can be seen that the impact outcome differs for different viscosity ratios. However no clear correlation between the viscosity ratio and the impact outcome can be discerned. Although the impact outcome is clearly influenced by the viscosity ratio, the viscosity ratio itself cannot be used to predict the impact outcome.

Especially, if high viscous liquids are involved the behavior differs significantly

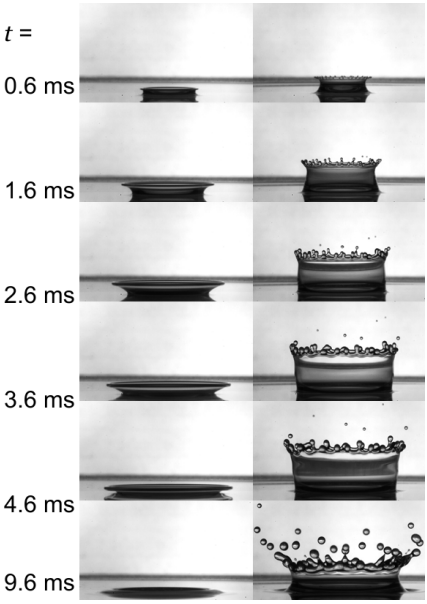

Figure 3.8: Influence of fluid combination on the corona development: Impact of a S5 drop onto a S65 film (left) with $\kappa = 13$ and of a S65 drop impacting onto a S5 film (right) with $\kappa = 0.08$ for $\delta = 0.25$, $U_0 = 2.3$ m/s and $D_0 = 2$ mm. Reprinted figure with permission from [92]. Copyright 2018 by the American Physical Society.

and builds an own regime. The effect of high viscous liquids is discussed in the following Section 3.1.2. For a highly viscous wall film the drop cannot evolve to a corona since the resistance of the wall film is too high and does not permit the evolution of a spreading lamella and subsequent corona. The drop barely penetrates or deforms the wall film; thus, the drop spreads like on a solid surface. If the wall film is less viscous the impact leads to a corona or even to corona splash. In both cases the maximum spreading diameter and the maximum corona diameter vary, depending on the viscosity of the drop.

Fluid temperature The temperature of the liquids as well as of the ambient gas can influence the impact outcome and cannot be neglected due to typical conditions in technical applications such as the combustion engine and spray cooling. The impacts onto heated [23] or cooled dry walls [161] have been investigated rather

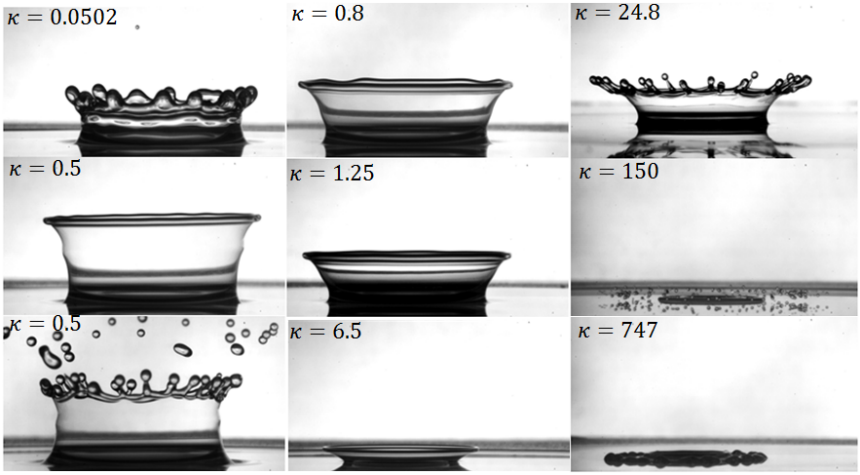

Figure 3.9: Effect of viscosity ratio (κ) on the outcome of drop impact with $\delta = 0.25$, $D_0 = 2$ mm and $U_0 = 2.3$ m/s. Reprinted figure with permission from [92]. Copyright 2018 by the American Physical Society.

often so far. Recent studies focused on the heat transfer during drop impact onto a wetted wall, while drop and wall film liquid have different temperature [60, 110]. In Fig. 3.10 the effect of temperature on the outcome is shown, while drop and wall film have the same temperature [26]. The influence of the temperature is minor in these experiments and only results in the change of the temperature dependent liquid properties. However, for high temperature the wall film starts to show instabilities. Comparable instabilities of the wall film have been observed in [60] in case of a temperature gradient of drop and wall film.

3.1.2 Drop impact of high viscous liquids

In order to investigate the transition from the outcome of drop impact onto a solid wall to a high viscous liquid film the kinematic viscosity of the wall film is varied up to 100 000 mm^2/s. A solid surface can be considered as a substrate with infinite viscosity.

High viscous wall film If the impact substrate is covered by a very high viscosity liquid or is a solid surface the drop spreads on the surface, as it can be seen in Fig. 3.11. The maximum spreading diameter $D_{max,spread}$ as well as the maxi-

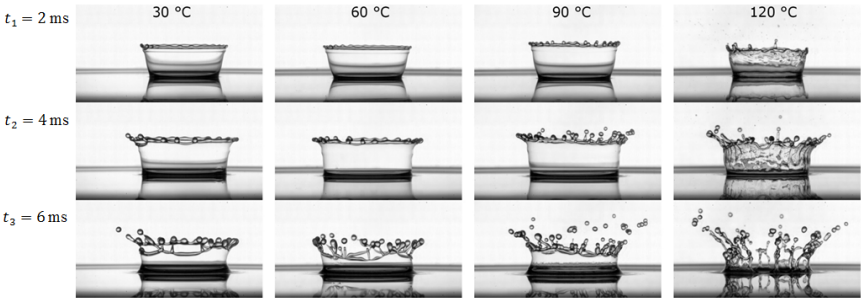

Figure 3.10: Effect of liquid temperature T on the outcome of a Hexadecane drop impacting onto a Hexadecane wall film with $\delta = 0.1$, $D_0 = 2$ mm and $U_0 = 3$ m/s [26].

mum spreading time t_{max} are mainly determined by the viscosity of the drop and the kind of the impact substrate. In this case the viscosity of the wall film determines the phenomenon itself, deposition, but the viscosity of the drop determines the geometrical and temporal parameters like $D_{max,spread}$ and t_{max}. Comparing the outcomes of the same drop impacting onto different wall film liquids, as it can be seen in Fig. 3.11, the outcome does not differ much from each other, whereby comparing the outcomes of the same wall film liquid but different drop liquids the outcomes differ significantly from each other. The impact substrate determines the motion of the drop after the impact, whether the drop can build a corona or the fluid of the drop is stopped and end in deposition. The higher viscous the film gets the less motion of the drop is enabled due to the viscous forces. In the case of deposition the higher viscous the drop gets the less spreading occurs also due to the viscous forces. The motion of the drop is stopped due to the inaction of the drop. Directly after the drop impact a very high viscous drop only sits on the impact substrates, but does not spread what is caused by the high viscosity and its loss of ambition to change its shape. During the first few milliseconds a very high viscous drop gets only compressed breadth wise, then the motion of the drop is stopped. In the second phase which lasts much longer, several seconds, the contact angle decreases slowly. Due to this damping behaviour the viscosity of the liquids highly influences the impact outcome [89].

If the wall film is very viscous, the film thickness is not influencing the impact outcome at all since the viscosity is preventing any motion in the wall film and the penetration of the drop into the wall film is insignificantly small.

The outcome of less viscous drops impacting onto high viscous wall films is

discussed separately in Section 3.1.4.

High viscosity drop If the liquid of the impact substrate is less viscous the drop impact leads to the evolution of a corona. Furthermore, corona splash can also be observed. The impact outcome itself is influenced by the viscosity of the wall film whereby the maximum spreading diameter $D_{max,spread}$ and maximum corona diameter D_{max} are highly influenced by the viscosity of the drop as it can be also observed in the case of deposition. It can be observed that with increasing viscosity of the drop D_{max} decreases whereas the increase of the viscosity of the wall film does not significantly influence D_{max} as shown in Fig. 3.11.

The fluid of the drop seems to predominate the impact outcome as well as the corona propagation. In the case of splashing though it can be observed that the fluid of the wall film determines the splashing threshold as it can be seen in Fig. 3.11. In the case of a highly viscous drop the splashing threshold is already reached at a wall film viscosity of $\nu_f = 20$ mm^2/s. For a high viscous wall film the drop cannot evolve to a corona since the resistance of the wall film is too high and does not admit the evolution of a corona. The drop can only slightly penetrate the wall film. Therefore, the drop spreads on the high viscous wall film alike on a solid surface such as glass. If the wall film is less viscous the drop impact leads to corona or even to corona splash. In this case the drop is able to penetrate into the wall film, the liquid of the wall film is pushed aside and a corona is built. In both cases the maximum spreading diameter and the maximum corona diameter vary dependent on the viscosity of the drop. Similar to a high viscous wall film a high viscous drop does not change its shape too much. In contrast a less viscous drop extends into the wall film [89]. The liquid combinations in Fig. 3.11 are miscible. In Fig. 3.12 a silicone oil drop impacts onto a water film. In these case the liquids are immiscible. At the instant of the impact a corona is formed with an early secondary droplet production. After about 0.1 ms the corona angle changes from pointing outwards of the impact center to pointing inwards. The drop penetrates the wall film liquid and spreads on the impact substrate (smooth glass), probably similar to the impact on glass, while the wall film liquid is covering the drop. It seems that the wall film liquid forms an inbound corona around the spreading drop. Finally, the corona collapses and the covering liquid flows downwards into the wall film. No obvious effect of the film thickness (within the *thin film* regime) can be observed in this case. Solely the depth of immersion of the drop changes due to the different film thicknesses. Since both liquids are immiscible no interaction between both liquids occur. Due to the high viscosity of the drop liquid the drop can be compared with a slightly formable particle.

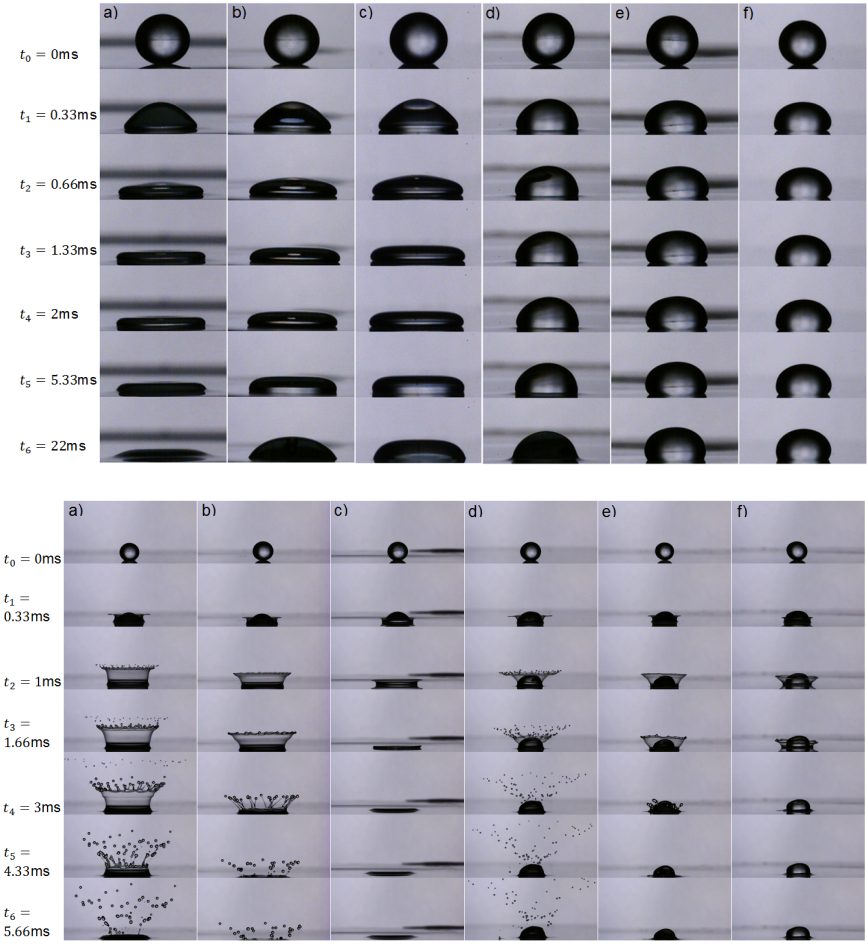

Figure 3.11: Temporal development of the drop spreading of a S350 drop (a)-c)) and a S10000 drop (d)-f)) impacting onto different impact substrates, wall film of S1000 (a), d)) and of S100000 (b), e)) with the same relative film thickness $\delta = 0.227$ and glass (c), f)) (a) and impacting onto different impact substrates, wall film of S5 (a), d)), S10 (b), e)) and S20 (c), f)) for the same relative film thickness $\delta = 0.045$ (b). Reprinted figure with permission from [92]. Copyright 2018 by the American Physical Society.

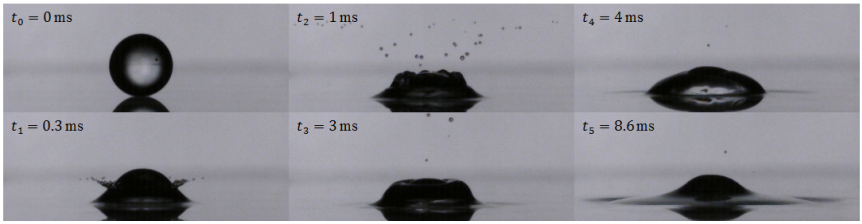

Figure 3.12: Temporal evolution of a S350 drop impacting onto a water wall film with $\kappa = 0.0028$, $U_0 = 3$ m/s, $D_0 = 2.2$ mm and $h = 0.1$ mm.

3.1.3 Outcomes of drop impact on soft substrates

Solid substrates can be classified by such as soft or hard, structured or smooth. In order to investigate the effect of the softness of the substrate the complex shear modulus of the substrates is systematically varied. A short description of the substrate generation can be found in Section 2.1.6 and a detailed description in [90]. The properties of the soft substrates can be found in Table 2.3. Furthermore, the effect of the viscosity of the impacting drop is investigated by varying the drop liquid. Water and seven different glycerine-water solutions have been used, listed in Table 2.1. The Reynolds number is varied in the range from 33 to 5485 and the Weber number from 296 to 480.

The temporal evolution of the drop impacts at different Reynolds numbers on the same soft substrate with the mixing ratio 10:1 is shown in Fig. 3.13. The process of drop impact onto a dry substrate can be subdivided into three phases: initial drop deformation, spreading and receding. During the spreading phase the drop spreads radially immediately after its impact. The thin spreading liquid lamella is bounded by a rim [157], which is formed by surface tension and viscous forces. Rim instabilities can lead to the formation of secondary droplets under certain conditions. Different impact outcomes on the same deformable substrate with the mixing ratio 10:1 are shown in Fig. 3.13, partial rebound is observed for Reynolds numbers $Re > 5114$. Secondary droplets appear as a result of splash for the Reynolds numbers $Re \leq 2050$. In the intermediate range of Reynolds number drop collision leads to the deposition without breakup [90].

3.1.4 Dancing droplets

If silicone drops of low viscosity impact onto a high viscous silicone oil film or on soft PDMS substrate as described in Chapter 2.1.6, dancing secondary droplets can

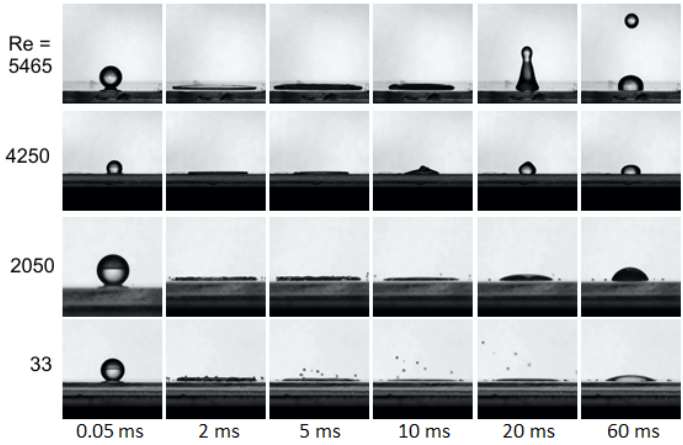

Figure 3.13: Temporal evolution of impacts of drops of different viscosities on a deformable substrate with the mixing ratio 10:1 (complex shear modulus at 1 Hz is 703.43 kPa as shown in Table 2.3). The liquids are the water-glycerin mixtures of 5, 20, 40 and 90 wt. % (from the upper to the bottom raw). The impact velocity is $U_0 = 3$ m/s and the initial drop diameter is $D_0 = 2.3$ mm. The Weber number ranges from $We = 300$ to 490. (Reprinted from [90].)

be observed after detaching from the finger-like jets. In both cases the drop spreads on the impact substrate and finger-like jets are produced. When the receding phase starts the finger like jets are pulled back towards the impact center. Finally, the drops, which are still attached to the finger-like jets, detach from the jets. Due to this pulling back the secondary droplets get a momentum in the direction towards the impact center, which leads to dancing droplets. According to our observation this behaviour is only observed if the material of drop and impact substrate if the material of drop and impact substrate are similar in chemical nature. Since PDMS is based on silicone oil, the drop liquid and the substrate material are related to each other.

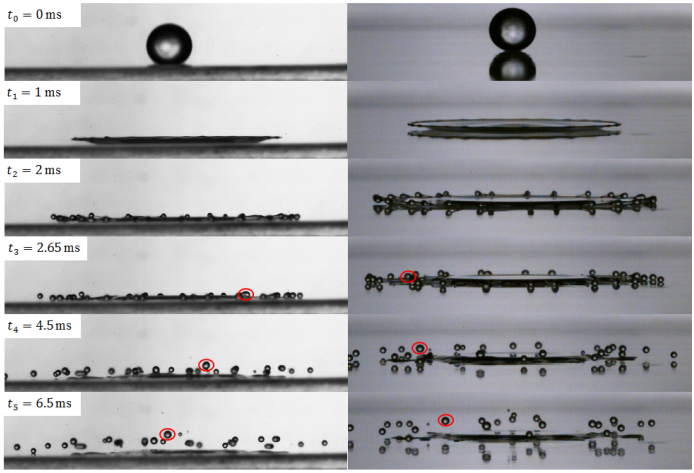

Figure 3.14: Temporal evolution of spreading and splashing including the *dancing droplets* of a S10 drop impacting onto the soft substrate S4 (left) and a S100000 wall film of $h = 0.1$ mm (right) with $D_0 = 2.8$ mm and $U_0 = 3$ m/s. For both image sequences one *dancing droplet* is tracked and marked with a red circle exemplary.

3.2 Kinematics of drop spreading without corona

3.2.1 Drop impact on a highly viscous wall film

In case of wall films of high viscous liquids the maximum spreading diameter $D_{max,spread}/D_0$ is determined by the viscosity of the drop as shown in Section 3.1.2. In order to determine the effect of a high viscosity liquid on the process of spreading the dimensionless maximum spreading diameter $D_{max,spread}/D_0$ and the dimensionless maximum spreading time τ_{max} are evaluated. The dimensionless maximum spreading time τ_{max} is defined below in Eq. (3.2),

$$\tau_{max} = t_{max} \frac{U_0}{D_0} Re_d^{-1/5} \tag{3.2}$$

with the impact velocity U_0, the initial drop diameter D_0. $\frac{U_0}{D_0} Re^{-1/5}$ is the typical time of expansion of the boundary layer in the drop [153].

In Fig. 3.15 the dimensionless maximum spreading time τ_{max} is shown as a function of the viscosity ratio κ. For a range of viscosities the value of τ is near to

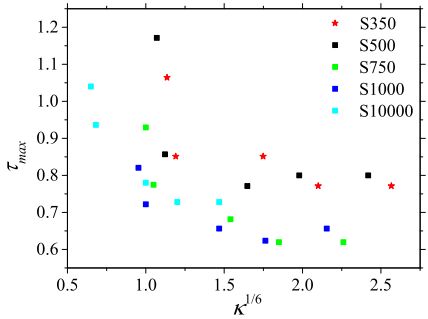

Figure 3.15: τ_S as given in Eq. 3.2 as a function of the viscosity ratio κ for different impacting drop liquids.

unity. Therefore the time of drop deformation is determined by the expansion of the boundary layer. It can be seen that with increasing viscosity of the impacting drop onto different high viscous liquids the dimensionless time τ_{max} decreases respectively its dependence on $\kappa^{1/6}$.

The dependency of the dimensionless time $t_{max}U_0/D_0$ as a function of the Reynolds number of the drop on the viscosity of the drop in the case of glass as impact substrate is shown in Fig. 3.16. In the transition region of low and high viscous liquids expressed by the Reynolds number a jump can be seen. Due to the characteristic of low viscous and high viscous liquids the liquid moves very fast and accordingly stops its motion very fast. This leads to comparable dimensionless spreading times in the case of glass as impact substrate and therefore to the gap of the transition region.

The effect of the viscosity of the wall film on the dimensionless maximum spreading diameter is shown in Fig. 3.17. A clear correlation between D_{max}/D_0 and Re_d can be seen for the different impact substrates. Furthermore all results are rather in line with each other. In this parameter range the viscosity of the wall film does not influence the spreading behaviour. This shows that the drop impact onto a high viscous wall film can be compared to the drop impact onto a glass substrate. The experimental results are compared with a model of the dimensionless maximum spreading diameter by Roisman [153] shown in Eq. (1.13) and is valid for high Reynolds numbers. Due to the high viscous liquids the corresponding Reynolds numbers are rather small. Therefore, the following simplified expression of

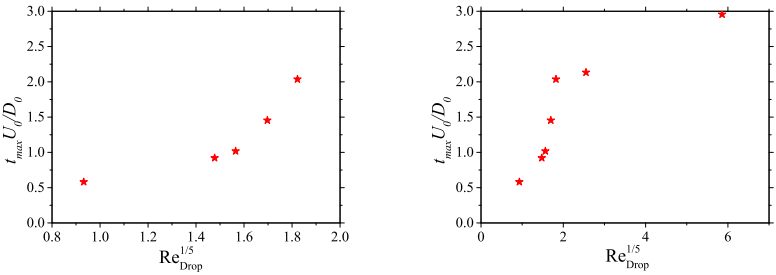

Figure 3.16: Dimensionless spreading time $t_{max}U_0/D_0$ as a function of the Reynolds number of the drop for different drops impacting onto glass: in the viscous regime Re < 20 (left) and including the transition region of low and high viscosity (right).

Eq. (1.13) is used.

$$\overline{D}_{max} \approx 0.87 Re^{1/5} \tag{3.3}$$

The theoretical $\overline{D}_{max}$ matches the experimental data rather well. For $Re \geq 0$ the theoretical $\overline{D}_{max}$ and the experimental $D_{max,spread}/D_0$ differ slightly from each other.

3.2.2 Drop impact on soft substrates

Immediately after impact onto a solid substrate a viscous boundary layer is formed and starts to expand [153]. As soon as the thickness of the boundary layer is equal to the thickness of the thinning, radially spreading lamella, the flow in the drop is governed mainly by the balance of inertia and viscosity. The velocity of spreading is quickly damped by the viscous stresses. The drop spreads until it reaches its maximum spreading diameter $D_{max,spread}$. For hydrophobic substrates the capillary forces associated with the surface wettability induce a receding motion. The time scales for spreading and receding differ significantly from each other. While the spreading phase only lasts about 2 ms in these experiments, the receding phase takes much longer depending on the impact substrate, as it can be seen in Fig. 3.18 for various substrate materials. The spreading phase is almost not influenced by the substrate material leading to approximately the same dimensionless maximum spreading diameter. However, the influence of the deformable coating on the velocity of the rim propagation becomes very significant during receding. In fact the

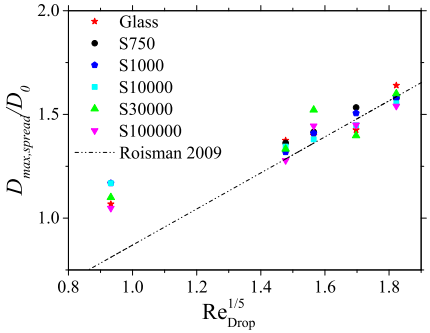

Figure 3.17: Dimensionless maximum spreading diameter as a function of the Reynolds number of the drop for different impact substrates. The relative film thickness is $\delta = 0.23$ and the impact velocity $u = 3.2$ m/s.

phenomenon of drop spreading on deformable viscoelastic substrates is very similar to the drop spreading on dry solid substrates of different wetting properties. It is very probably that the flow in the neighborhood of the moving contact line is a decisive factor, also in the case of drop receding on a deformable substrate [90].

The spreading diameter is non dimensionalised by dividing the instantaneous spreading diameter D by the initial diameter D_0. Partial rebound occurs when the dimensionless spreading diameter falls below the value 1. The initial spreading phase is comparable for the entire range of the Reynolds number. The receding phase, which starts after 5 ms in these experiments, is influenced by the underlying substrate. After reaching the maximum spreading diameter all the drops are slowed down and reach a final equilibrium diameter. This final equilibrium diameter depends significantly on the impact substrate as it can be seen in Fig. 3.18.

Fig. 3.18 shows the evolution of the spreading diameter against time for different substrates. Both the spreading diameter and the time are non dimensionalised. The figure shows that there is hardly any difference in the spreading behaviour until the drop reaches a maximum diameter. The spreading phase therefore is not significantly influenced by the elasticity of the substrate or by the Reynolds number of the drop. The receding phase though is significantly influenced by the softness as the impact energy is absorbed by the deformable substrate and the drop does not have the energy to retract back and rebound. It is also seen that the final contact diameter increases with increasing of mixing ratio, i.e. increasing of

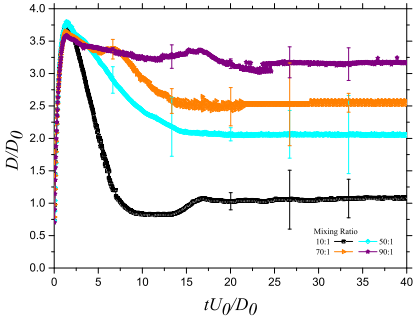

Figure 3.18: Evolution of the dimensionless spreading diameter as a function of the dimensionless time for the water drop impacting substrates of different shear modulus.

softness. This effect can be attributed to the substrate deformation in the vicinity of the three-phase contact line. This deformation provides additional friction to the contact line motion thereby reducing the velocity of receding phase [90]. Similar observations were made in the previous studies on deformable substrates as well [77, 103].

3.3 Kinematics of the corona expansion

The previous Section 3.1 illustrates clearly that the outcome of drop impact onto a film of a different liquid depends not only on the impact parameters but also on the viscosities of drop and film. It is very difficult to understand or analyse experimental data if so many parameters influence the problem. Therefore, some fundamental discussion about the dynamics of drop impact is necessary prior to any analysis of the experimental results.

3.3.1 Dynamics of a drop impact onto a liquid layer

If the impact velocity is high enough, which means that both Reynolds and Weber numbers are much larger than unity, the flow in the spreading lamella can be subdivided into an outer solution and the near-wall viscous boundary layer. In the outer solution the influence of the viscous and capillary terms are negligibly small in comparison with the dominant inertial terms. This solution determines the flow in

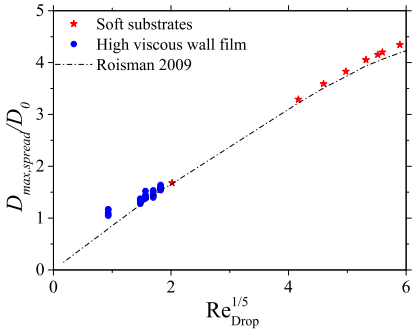

Figure 3.19: Dimensionless maximum spreading diameter as a function of $Re_{Drop}^{1/5}$ compared with the theoretical model of Roisman [150]. (Reprinted from [90].)

the lamella whenever the thickness of the viscous boundary layer is much smaller than the thickness of the lamella. At later stages viscous terms become dominant. In the next sections the main flow regions and impact phases are considered in more detail.

3.3.2 Inertia dominated flow in the spreading lamella: Outer solution

When a drop impacts onto a liquid layer, the dynamic pressure at the drop/film interface leads to the generation of a crater. The liquid layer between the expanding crater and the substrate consists of the two liquid films. The upper film corresponds to the drop liquid and the lower film corresponds to the liquid of the initial wall film. If the impact Reynolds and Weber numbers are much larger than unity, the flow in the radially expanding liquid layer is inertia dominated. The remote asymptotic solution for potential flow in the spreading lamella, valid for large times, has been obtained in [202] from the mass and momentum balance equations

$$u_r = \frac{r}{t + \tau D_0/U_0}, \quad u_z = -\frac{z}{2(t + \tau D_0/U_0)} \tag{3.4}$$

where r and z are the radial and axial coordinates in the system with the origin fixed at the point of impact on the substrate, u_r and u_z are the radial and axial components of the velocity vector, τ is a dimensionless constant, which depends

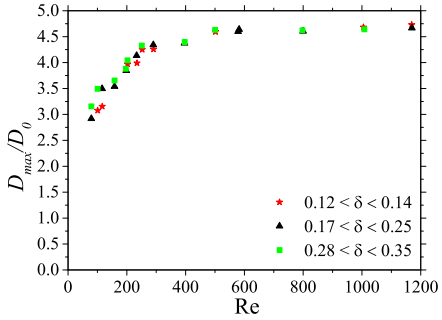

Figure 3.20: Dimensionless maximum corona diameter for drop impact onto a thin wall film $0.12 < \delta < 0.36$. Drop diameter is between 1.45 and 2 mm while the impact velocity is almost constant, $U_0 \approx 2.8$ m/s. Liquid viscosity is varied in the range $5 \times 10^{-6} < \nu < 5 \times 10^{-5}$ m^2/s, while $\kappa = 1$. The Weber number is varied from 550 to 900. (Reprinted from [90].)

only on the relative film thickness. The thickness of the lamella at large times is obtained in the form [202]

$$h_{\text{lam}} = \frac{\eta D_0^3}{U_0^2 (t + \tau D_0/U_0)^2} \tag{3.5}$$

where η is a dimensionless constant. This scaling has been confirmed by experiments on drop impact onto a spherical target [10].

The expanding film in the lamella interacts with the outer unperturbed liquid film. In the study of Yarin and Weiss [202] this interaction has been described as a propagation of a kinematic discontinuity, associated with the corona. The thickness of the sheet in the expanding corona is obtained from a mass balance of the kinematic discontinuity. This thickness is physically the sum of the thicknesses of the outer film and of the instantaneous thickness of the lamella in the crater region. The evolution of the corona radius is described using the mass and momentum balance equations and is expressed in the form

$$R_{\text{corona}} = \beta U_0^{1/2} D_0^{1/2} \left(t + \frac{\tau D_0}{U_0} \right)^{1/2} \tag{3.6}$$

where β is a dimensionless constant determined mainly by the dimensionless initial

film thickness.

In the work of Roisman et al. [158] the expression for $R_{\mathrm{corona}}(t)$ has been generalized by taking into account the effects associated with the surface tension and gravity. It is shown that the dimensionless maximum corona diameter, scaled by the drop diameter, is determined only by the impact Weber number and by the relative initial wall film thickness.

3.3.3 Viscous regime of corona propagation

For relatively thin liquid films in the range $0.05 < \delta < 0.2$ the splashing threshold and the threshold associated with the corona/deposition limit depend weakly on δ. This important observation of [146] contradicts the correlations for the critical K number (1.25), which are probably more applicable to the cases for film thicknesses $\delta > 0.2$.

In the case of drop impact onto a relatively thin liquid film the maximum corona diameter is mainly determined by the Reynolds number while the influence of the Weber number is small, as can be seen in Fig. 3.20 and Fig. 3.21. The value of the maximum corona diameter is defined not by the instant before corona receding but by the instant when the corona falls down onto the liquid film and deposits on it. The film thickness only weakly influences the value of D_{max} in this regime as shown in Fig. 3.20.

The values of the Reynolds number corresponding to the data in Fig. 3.20 are much smaller than their values corresponding to the data used in [158]. Therefore, drop impact onto a thin viscous liquid film occurs in a regime which is completely different from the regime governed by surface tension and gravity, studied in [158]. The corona propagation in the fully developed viscous film flow has not yet been analysed in the literature.

During fast drop impact, leading to splash, viscosity becomes important only in the viscous boundary layer [153], whose thickness increases in time, $h_\nu \sim \sqrt{\nu t}$. At some instant, $t_{\mathrm{visc}} \sim h^2/\nu_f$, the thickness of the boundary layer is equal to the initial film thickness. At this instant the viscosity starts to damp the propagation of the corona at the film. The values of t_{visc}, of the film thickness h_{visc} and the corona radius R_{visc} at this instant can be estimated with the help of (1.18)

$$t_{\mathrm{visc}} = \frac{D_0}{U_0} Re^{1/5}, \quad h_{\mathrm{visc}} = D_0 Re^{-2/5}, \quad R_{\mathrm{visc}} = D_0 Re^{1/10}. \tag{3.7}$$

In this study t_{visc} and R_{visc} are considered as time and length scales, while h_{visc} is the scale for the lamella thickness. Constants are omitted in expressions (3.7). The scales (3.7) are suitable for the description of the fully developed flow in the liquid lamella since $h_{\mathrm{visc}}^2 = t_{\mathrm{visc}}\nu$.

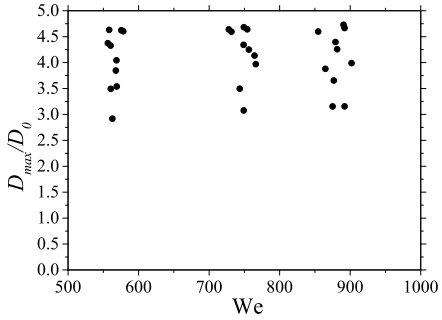

Figure 3.21: Dimensionless maximum corona diameter for drop impact onto a thin wall film $0.12 < \delta < 0.36$ as a function of the Weber number. Drop diameter is between 1.45 and 2 mm while the impact velocity is maintained approximately at $U_0 \approx 2.8$ m/s. Liquid viscosity is varied in the range $5 \times 10^{-6} < \nu < 5 \times 10^{-5}$ m^2/s, while $\kappa = 1$.

The fully developed flow in the lamella at large times is roughly described by assuming a parabolic profile of the radial velocity component in the form

$$u_r = \frac{rU_0}{D_0}\left(\frac{2y}{h} - \frac{y^2}{h^2}\right) F(t), \tag{3.8}$$

where $F(t)$ is a dimensionless function which satisfies the initial conditions

$$F(t_{\text{visc}}) = \lambda_f \frac{D_0}{U_0 t_{\text{visc}}}, \quad h(t_{\text{visc}}) = \lambda_h h_{\text{visc}}, \tag{3.9}$$

where λ_f and λ_h are dimensionless constants determined by the film relative thickness.

The momentum balance equation can be satisfied only in an integral form

$$\int_0^h \left(\frac{\partial u_r}{\partial t} + u_r\frac{\partial u_r}{\partial r} + w\frac{\partial u_r}{\partial y} - \nu\frac{\partial}{\partial r}\left[\frac{1}{r}\frac{\partial r u_r}{\partial r}\right] - \nu\frac{\partial^2 u_r}{\partial y^2}\right) \mathrm{d}y = 0, \tag{3.10}$$

where the axial component of the velocity field is determined from the continuity equation

$$w = -\frac{1}{r}\int_0^y \left(\frac{\partial r u_r}{\partial r}\right) \mathrm{d}y. \tag{3.11}$$

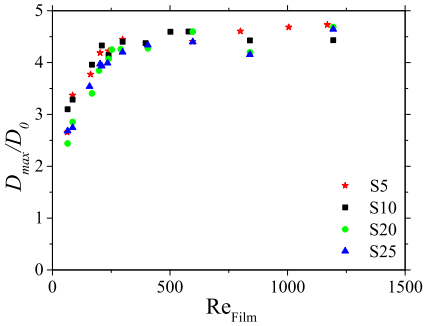

Figure 3.22: Dimensionless maximum corona diameter for different drop liquids onto a thin wall film of $0.12 < \delta < 0.17$ as a function of the Reynolds number of the wall film. Drop diameter is between 1.45 and 2 mm while the impact velocity is almost constant, $U_0 \approx 2.8$ m/s. Liquid viscosity is varied in the range $5 \times 10^{-6} < \nu < 5 \times 10^{-5}$ m^2/s.

Substitution of (3.8) in (3.11) and (3.10), and noting that $h'(t) = w(y = h)$, yields the following system of two ordinary differential equation for the function $f(t)$ and $h(t)$

$$45\frac{D_0 U_0}{h(t)^2 Re}F(t) + \frac{16U_0}{D_0}F(t)^2 + 15F'(t) = 0, \quad h'(t) = \frac{4hU_0}{3D_0}F(t). \tag{3.12}$$

The solution of this equation is straightforward, therefore we exclude algebraic transformations to simplify the readability of this study. Moreover, we are more interested in a correct scaling of the problem is than in an exact explicit solution.

The remote asymptotic solution of (3.12) valid for large times yields

$$h = h_{\text{visc}}\frac{\sqrt{3}}{\lambda_h A^{1/2}}\left(1 + \exp\left[-\frac{At}{t_{\text{visc}}}\right]\right), \quad F(t) = \frac{3A\lambda_f}{4\lambda_t Re^{1/5}}\exp\left[-\frac{At}{t_{\text{visc}}}\right], \tag{3.13}$$

where A is a dimensionless constant, determined from the conditions at $t = t_{\text{visc}}$.

The average radial velocity in the lamella at large times is $u_r \sim rU_0F(t)/D_0$. The propagation of the corona we describe as a kinematic discontinuity [202], neglecting the viscous losses at the base of the corona. The Bernoulli equation in this case yields $R_b'(t) = u_r(r = R_b)/2$. Solution of this ordinary differential

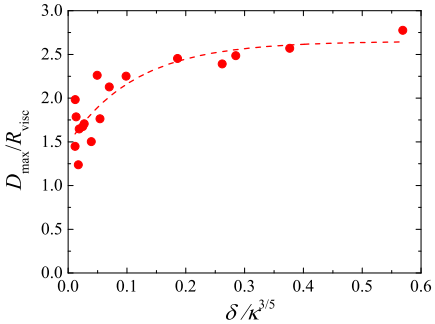

Figure 3.23: Dimensionless maximum corona diameter for drop impact onto a thin wall film $0.05 < \delta < 0.25$, scaled by R_{visc} as a function of the scaled interfacial velocity $\delta\kappa^{-3/5}$. The expression for R_{visc} is given by (3.7). The impact Reynolds number is in the range $230 < Re < 1300$.

equation with the help of (3.13) yields

$$R_b \sim R_{visc} \exp\left(-B \exp\left[-\frac{At}{t_{visc}}\right]\right), \tag{3.14}$$

where B is another dimensionless constant.

If the viscosities of the drop and of the film are not equal, the flows in both layers, of the drop and of the film liquids, have to be considered. At large times, corresponding to the viscous flow in both layers, and very thin liquid films the main additional influencing parameter is the relative interfacial flow. The value of this interfacial flow can be estimated from the condition of the continuity of the viscous shear stresses at the interface. The shear stress in each layer at larger times can be estimated as $\tau_{id} \sim \mu_d(u_d - u_i)/h_d$ and $\tau_{if} \sim \mu_f u_i/h_f$, respectively. The thicknesses of the layers can be estimated as $h_d \sim h_{viscd}$, $h_f \sim \delta h_{viscf}$. Neglecting the density difference of two liquids and assuming $u_i \ll u_d$ yields the following expression for the relative interface velocity

$$\frac{u_i}{u_d} \sim \frac{\delta}{\kappa^{3/5}}. \tag{3.15}$$

The dependence of the scaled maximum corona diameter D_{max}/R_{visc} on the relative interfacial velocity, defined in (3.15), is shown in Fig. 3.23 for different values of the initial film thickness $0.05 < \delta < 0.25$. Only cases of relatively

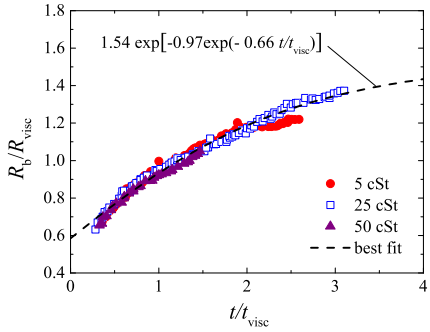

Figure 3.24: Evolution of the scaled corona radius at the wall, R_b/R_{visc}, for various liquid viscosities. The liquids of drop and wall film are the same. The relative film thickness is $\delta = 0.166$ and the impact velocity $u = 3.2$ m/s. The form of the best fit of the data is defined in (3.14).

high Reynolds numbers are shown in Fig. 3.23, $Re > 230$, to ensure that the drop spreading is inertia dominated at the initial stage of collision and that the time of corona spreading is much higher than t_{visc}.

For the initial thicknesses $\delta < 0.05$ the distinct dependence of $D_{\mathrm{max}}/R_{\mathrm{visc}}$ mainly on κ is disrupted. The flow in such thin films (of thicknesses around 50 micrometers or thinner) is probably influenced by additional factors, like substrate roughness or presence of micro-bubbles, etc.

In Fig. 3.24 the evolution of the scaled corona radius is shown as a function of a scaled time for three different liquid viscosities. The scaled curves coincide for all viscosities, which confirms our assumption that in the regime considered in these experiments, the propagation of the corona is governed by the inertia and viscosity. Moreover, the fit for the corona propagation in the form expressed in (3.14), $R_b/R_{\mathrm{visc}} = 1.54 \exp\left[-0.97 \exp\left(-0.66 t/t_{\mathrm{visc}}\right)\right]$, agrees very well with the experiments. The fitting parameters B and A are both of the order of unity. This result can also be considered as an indirect confirmation of the theory for viscous corona propagation.

If a high viscous drop impacts onto a less viscous wall film, a corona is evolved as shown in Fig. 3.11. The maximum corona diameter D_{max} is for this combination highly dependent on the viscosity of the drop as it can be seen in Fig. 3.25. Since all results are rather in line with each other the viscosity of the wall film does not seem

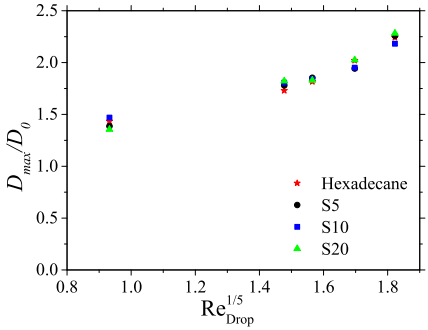

Figure 3.25: Dimensionless maximum corona diameter as a function of the Reynolds number of the drop for different wall film liquids. The relative film thickness is $\delta = 0.045$ and the impact velocity $u = 3.2$ m/s.

to influence D_{max}/D_0 significantly. Solely the impact outcome itself, corona or corona splash, is influenced by the viscosity of the wall film as shown in Fig. 3.11. Splashing is already suppressed at less viscous wall film such as $\nu_f = 20$ mm^2/s for a S350 impacting drop. A high viscous drop does not tend to spread after the drop impact what can already be seen in Fig. 3.11 in the case of deposition. Due to its contour accuracy which comes from the high viscosity the drop only pushes the liquid of the wall film aside but does not extend itself. Due to the kinetic energy resulting from the impact the shape of the corona is determined by the film liquid which is pushed aside while the drop nearly keeps its initial form. Therefore the maximum corona diameter decreases with decreasing Reynolds number of the drop.

3.4 Conclusions

Drop impact on a wetted wall leads to several impact outcomes. The different impact outcomes and the influencing parameters are presented and discussed in this chapter. High viscosity liquids as drop and respectively wall film are investigated as limiting cases. In case of drop spreading on high viscous wall films and soft substrates is mainly influenced by the Reynolds number. The viscosity of the drop and wall film are varied up to 100 000 mm^2/s as well as the relative film thickness. The dependency of the maximum spreading diameter in the case of deposition and maximum corona diameter in the case of corona on the Reynolds number is

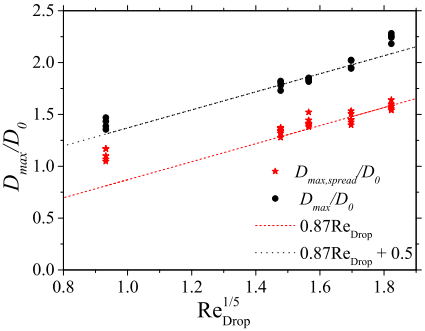

Figure 3.26: Dimensionless maximum corona and spreading diameter as a function of $Re_{Drop}^{1/5}$ compared with the theoretical model of Roisman [150].

shown. The viscosity of the wall film only influences the impact outcome itself, but the viscosity of the drop determines maximum spreading diameter and maximum corona diameter. In the case of a high viscous drop impacting onto a high viscous wall film, the outcome is comparable to the impact on glass except for its final resting shape. The dimensionless maximum spreading time τ has been introduced to determine the effect of the viscosity of the drop. In the case of a high viscous drop impacting onto a less viscous wall film the maximum corona diameter decreases with increasing drop viscosity. Dancing droplets were observed for silicone oil droplets of low viscosity impacting onto high viscous silicone oil wall films as well as on soft PDMS substrates. Since both liquids and respectively drop liquid and PDMS substrate are similar in chemical nature, during the receding stage the finger-like jets are pulled back towards the center leading to a momentum in the direction of the impact center. When the secondary droplets detach from the jets, they are moving inwards.

The expansion of the corona is described. It has been shown that drop impact onto a relatively thin layer of a viscous liquid, whose initial thickness is smaller or comparable with the viscous thickness $h_{\mathrm{visc}} \sim D_0 Re_f^{-2/5}$, is special. The flow in the lamella and the propagation of the corona in this regime are governed mainly by the balance of inertia and viscous stresses. Characteristic time and length scales for this regime are determined. The corresponding scaling of the corona radius is validated by the experimental data of impacts of drops of different viscosities.

4 Drop impact onto an inclined flowing wall film

In the present chapter the dynamics of drop impact onto an inclined, flowing wall film are shown and discussed. The normal impact of a drop onto a wetted substrate can lead to several outcome phenomena, depending on the impact parameters and fluid properties as discussed in Chapter 3. If the impact velocity is high enough the impact leads to the development of an axisymmetric corona bounded by a rim. The corona appears as a result of interaction of a radially expanding liquid film with the outer initially static wall film. Drop impact onto an inclined flowing wall film results in the expansion of a non-axisymmetric corona. In case of urea-water solutions as drop and wall film liquid, the formation of holes can be observed.

4.1 Observations of drop impact and corona expansion

In the case of the oblique impact the inclination angle also influences the impact outcome. The effect of the inclination angle and therefore the effect of the tangential component of the impact velocity is shown in Fig. 4.1 for the same dimensionless film thickness $\delta = 0.091$. At relatively small inclination angles the shape of the corona slightly deviates from the axisymmetric form. At higher impact angles the influence of the tangential component of the impact velocity becomes significant, which leads to an earlier collapse of the corona and finally no corona can be build anymore.

Additionally to the impact parameters and fluid properties the corona threshold and the splashing threshold are dependent on the angle of inclination. As it can be seen in Fig. 4.1 with increasing angle of inclination a corona cannot be built decreasingly.

The rear angle of the corona decreases significantly with increasing angle of inclination. Especially the rear part of the corona is influenced by the inclination. The front angle of the corona is not as much influenced by the inclination ratio. For the same impact parameters and fluid properties the drop impact cannot lead to the rise of a corona for higher angles of inclination anymore.

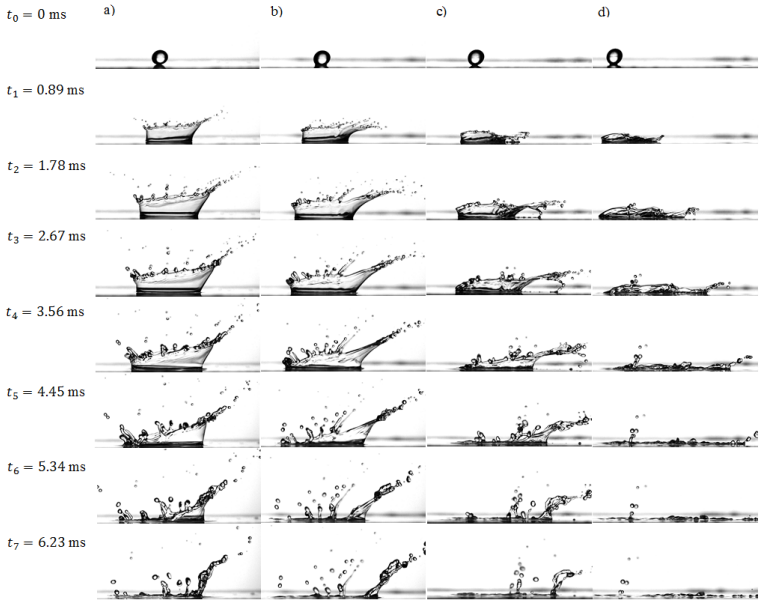

Figure 4.1: Development of a corona generated by an inclined impact of an S5 drop onto a W film of the dimensionless thickness $\delta = 0.091$ for different angles of inclination: α_{incl} a) 20°, b) 30°, c) 40° and d) 50°. The liquids and their properties are listed in Table 1.

The instant of the corona collapse is also significantly influenced by the relative film thickness δ and the fluid properties. For higher film thickness, $\delta = 0.18$, the time until corona collapse is higher than for thinner film thickness, $\delta = 0.091$, as can be seen in Fig. 4.2. To investigate the effect of the drop viscosity, the fluid of the drop is varied and the fluid of the wall film is kept constant. The outcome of the impact of different drop fluids for the same impact parameters (impact velocity and angle of inclination) and do not differ significantly from each other.

4.2 Analysis of corona propagation

Due to the inclination and therefore the influence of inertia the base of the corona is not axisymmetric anymore. This requires a different approach regarding the geometry of the corona.

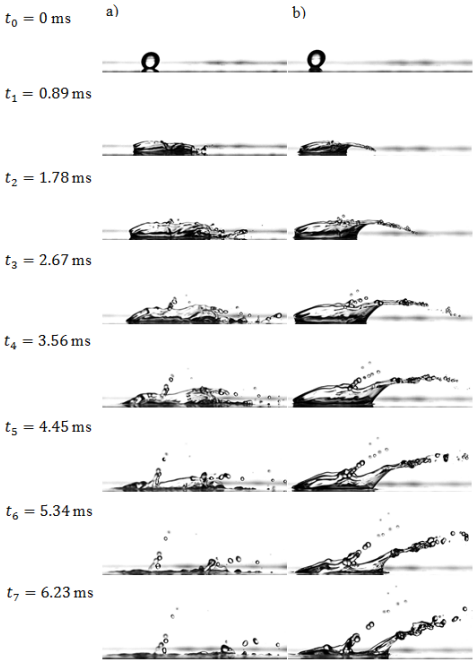

Figure 4.2: Development of a corona generated by an inclined impact of an S5 drop onto a W film for different relative film thicknesses δ a) 0.091 and b) 0.18. The impact angle is $\alpha_{incl} = 45°$ for both cases.

4.2.1 Geometry of the expanding corona

The main geometrical parameters of the expanding corona are defined in Fig. 4.3. The width of the corona is considered separately for the rear and the front part X_r and X_f, which are scaled by the initial drop diameter D_0, starting from the center of the impact point of the drop.

The impact parameters and fluid properties influence the geometry of the expanding corona differently. In Fig. 4.4 the effect of the drop viscosity on the corona spreading respectively (X_f and X_r) is shown for two different angles of inclination. It can be seen that the drop viscosity does not influence the corona spreading. The corona spreading is therefore dominated by the impact parameters and the liquid of the wall film, but not by the liquid of the drop. However, the viscosity of the drop determines the corona threshold, whether a corona will build or not. For

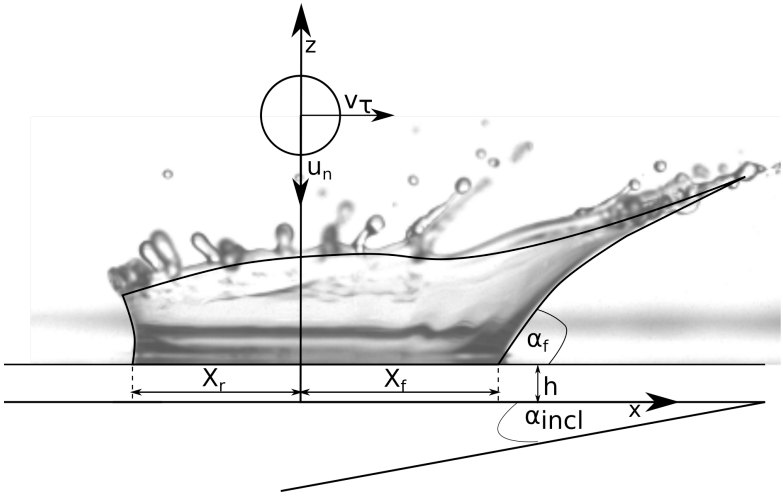

Figure 4.3: Definition of the main geometrical parameters of the corona.

higher drop viscosities the corona threshold is already reached at lower inclination angles. Since the corona expansion is not significantly influenced by the drop viscosity, the corona threshold seems to be dependent on the drop viscosity and the inclination angle only.

It can be seen that the viscosity of the drop does not influence D_{max}/D_0, as already shown in Fig. 4.4 (a). The angle of inclination additionally results in a decreasing D_{max}/D_0 for increasing α_{incl}. In Fig. 4.4 (b) the effect of the relative film thickness δ is shown for two different fluid combinations. The corona spreading is not influenced by the relative film thickness, but the maximum spreading time is influenced. For a smaller relative film thickness the spreading stops much earlier.

Since drop viscosity and relative film thickness do not influence the corona spreading, the influence of the angle of inclination is shown in Fig. 4.5. The front diameter X_f increases with increasing α_{incl} while the rear diameter X_r decreases with increasing α_{incl} for both relative film thicknesses.

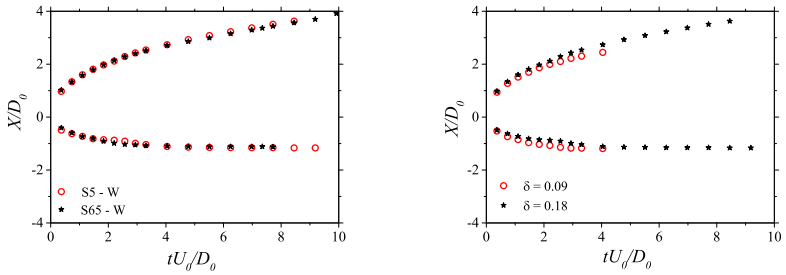

(a) (b)

Figure 4.4: Effect of drop viscosity ν_d on the corona propagation for $\alpha_{incl} = 30°$ (a) and of relative film thickness δ on the corona propagation for S5 - W (b).

4.2.2 Theoretical model for the propagation of the corona base

The evolution of the corona has been considered in Roisman et al. [158] for normal impact of a drop onto a wall film of the same liquid. The evolution of the corona is governed by the inertial forces and surface tension. The inertial forces are dominant if both the Reynolds and Weber numbers are much larger than unity. The velocity of the corona expansion is obtained from the Bernoulli equation [158] in the following approximate, dimensionless form

$$U_{cr} = \frac{dX}{dt} = \frac{u_x}{2} - \frac{G}{2\delta u_x}, \quad G = \frac{\delta^2}{Fr} + \frac{4}{\mathrm{We}}, \tag{4.1}$$

where u_x as x-component of the velocity field u in the lamella inside the cavity, δ is the dimensionless film thickness and X is the x-coordinate of the corona base, both scaled by the drop diameter, U_{cr} is the dimensionless crater expansion velocity, scaled by the normal component of the impact velocity. In the computation of the Weber and Froude numbers the normal component of the impact velocity is used.

In the case of oblique impact the velocity in the lamella can be expressed as a superposition of the translational motion with the velocity V in the x-direction defined as

$$V = \frac{v_\tau}{u_n} = \tan\alpha \tag{4.2}$$

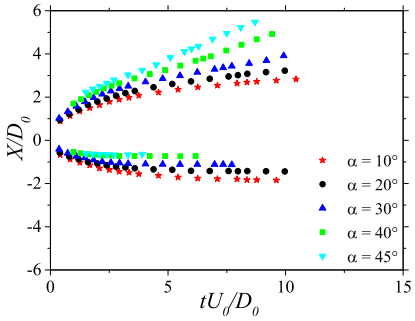

Figure 4.5: Effect of inclination on the corona propagation for the fluid combination S65 - W for $\delta = 0.18$.

and the radial expansion velocity [151]

$$u = V\mathbf{e}_x + \frac{(x - Vt)\mathbf{e}_x + y\mathbf{e}_y}{t - \tau} \tag{4.3}$$

the x-component of the flow in the lamella is therefore

$$u_x = \frac{\tau V + x}{t - \tau} \tag{4.4}$$

where τ is a dimensionless parameter which depends on the wall film thickness. The empirical expression

$$\tau \approx 0.8\ \delta^{1.7} \tag{4.5}$$

is obtained in Roisman et al. [158] by fitting the experimental data for normal impact.

Substituting Eq. (4.3) in the ordinary differential equation Eq. (4.1) yields

$$X_f = \tau V + \sqrt{\beta_f T - \frac{GT^2}{\delta}}, \quad X_r = \tau V - \sqrt{\beta_r T - \frac{GT^2}{\delta}}, \quad T = t - \tau, \tag{4.6}$$

valid for the cases of thin wall film, $\delta \ll R_{cr,max}$. Here $X_f(T)$ and $X_r(T)$ are the frontal and rear positions of the corona, β_f and β_r are dimensionless parameters, depending on δ and on the inclination angle.

The time instants associated with the duration of the corona expansion are

$$T_{max,f} = \frac{\beta_f \delta}{2G}, \quad T_{max,r} = \frac{\beta_r \delta}{2G} \tag{4.7}$$

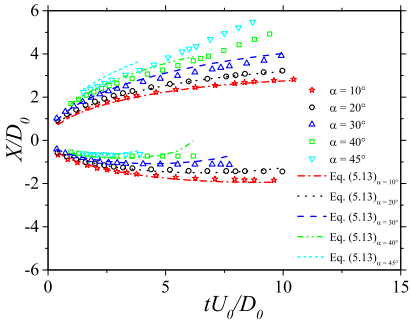

Figure 4.6: Comparison of the theoretical model X_r and X_f with the experimental data for the liquid combination S65 - W and $\delta = 0.18$.

and the coordinates, corresponding to the maximum corona expansion are

$$X_{max,f} = \tau V + \frac{\beta_f \sqrt{H}}{2\sqrt{G}} - \frac{H}{GWe}, \quad X_{max,r} = \tau V - \frac{\beta_r \sqrt{H}}{2\sqrt{G}} + \frac{H}{GWe}. \tag{4.8}$$

In Fig. 4.6 the experimental data is compared with the model defined in Eq. (4.6). The continuous line in the respective colour represent the model as a function of the angle of inclination. For both X_f and X_r good agreement can be seen. The values for β_f and β_r are obtained by fitting the experimental data

$$\beta_f = 0.66\, \delta^{-0.33} \cos^{25\,\delta} \alpha, \quad \beta_r = 0.527\, \delta^{-0.33} \cos^{-25\,\delta} \alpha. \tag{4.9}$$

These parameters determine the rate of initial corona spreading. However the model in Eq. (4.6) agrees excellently also for the later periods of corona spreading during the stages when X deviates from the square root expansion.

The model is not valid for the corona receding, free motion under the action of gravity, and collapse. This stage of corona dynamics has to be treated separately.

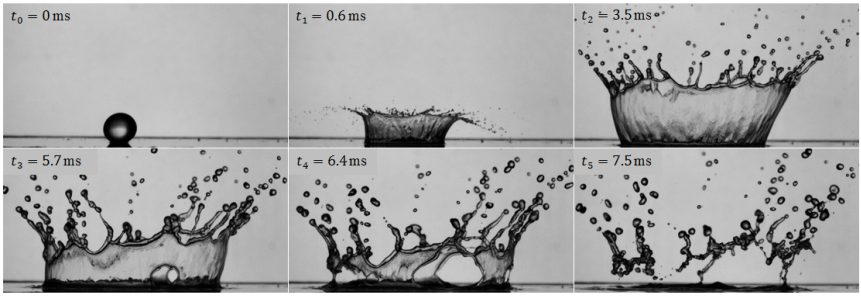

Figure 4.7: Temporal evolution of an *AdBlue* drop impacting onto a water wall film with $\delta = 0.08$, $U_0 = 4$ m/s and $\alpha_{incl} = 10°$ with hole formation.

4.3 Hole formation in the corona wall

In the exhaust gas treatment system of a Diesel combustion engine a Diesel exhaust fluid is used for a selective catalytic reduction reducing the NO_x concentration of the emissions produced by a Diesel combustion engine. This Diesel exhaust fluid *AdBlue* is made by 32.5 wt.% urea and 67.5 wt.% deionized water. In this section different urea-water solutions are investigated.

In Fig. 4.7 the temporal evolution of an *AdBlue* drop impacting onto a water film is shown. The corona wall shows instabilities starting from the corona formation. These instabilities seem to come from the urea concentration in the liquid. At same time small holes appear in the corona wall, which are growing till the corona is completely destroyed. These holes can be observed at any position of the corona. The formation and growth of holes is shown exemplary in Fig. 4.8. Starting from the first formed hole several holes appear and grow. The occurrence of holes can only be observed for a limited range of parameters, such as rather small film thicknesses. In these experiments it can be observed in the range of $0.04 < \delta < 0.1$. Furthermore, the hole formation can only be observed if the urea concentration of drop and wall film is different and therefore a concentration gradient is required. In cases of a water drop impacting onto a water film or respectively an *AdBlue* drop impacting onto an *AdBlue* film in the same range of parameters no hole formation is observed. Hole formation can also be observed for different inclination angle, as long as a corona arises. In Fig. 4.9 the dimensionless break up time of the first formation of holes is plotted against the urea concentration difference of wall film and drop. It can be clearly seen that the dimensionless break up time is dependent on the concentration gradient. Consequently, the break up time can also be shown as a function of the viscosity ratio κ.

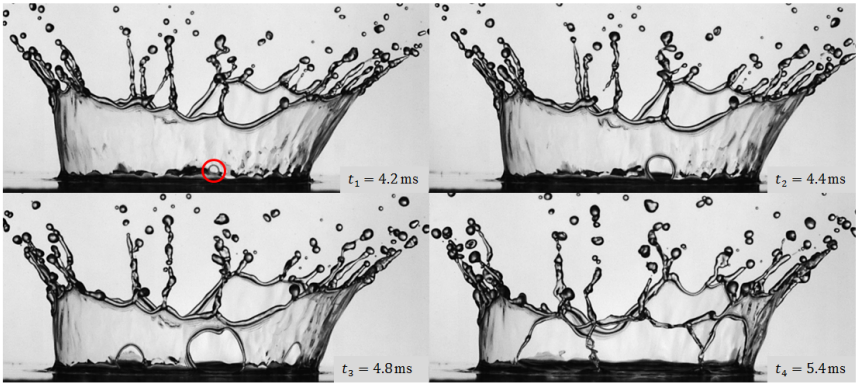

Figure 4.8: The formation of holes in the corona wall resulting from an U40 drop impacting onto an *AdBlue* wall film with $\delta = 0.06$, $U_0 = 4$ m/s and $\alpha_{incl} = 10°$.

Since the hole formation is clearly dependent on the concentration difference of drop and wall film, the hole formation seems to be influenced by the Marangoni driven instability, which was observed by Thoroddson et al. [6, 174] and Geppert et al. [64]. Thoroddson et al. and Aljedaani et al. observed hole formation in the corona wall for high viscous drop impacting onto low viscous wall film liquids. The Marangoni holes are formed after previous produced secondary droplets hit the corona wall [6, 174], which is not the case in these experiments. Furthermore, hole formation can be observed for a range of viscosity ratios $0.7 < \kappa < 1.1$. This shows that holes are formed for both combinations, whether the drop is more viscous or the wall film. Geppert et al. observed the formation of holes also for small relative film thicknesses, but only for high Weber numbers ($We > 1000$), while hole formation can be observed in these experiments for Weber numbers of the drop varying in the range from $We_D = 380$ to $We_D = 760$. Although, Terzis et al. investigated the splashing behaviour of different urea-water concentrations, no hole formation was observed due the higher relative film thickness $\delta > 0.2$ [172].

In these experiments the concentration difference seems to implicate local Marangoni driven flow in the corona wall. This flow finally leads to the formation of holes. The implicated Marangoni driven flow flows from the higher to the lower concentration. It can be seen that if the urea concentration of the wall film is higher than the concentration of the drop the hole formation begins earlier. This shows that not only the urea concentration gradient determines the formation time but also which liquid is higher concentrated. Since in the exhaust gas system *Ad-*

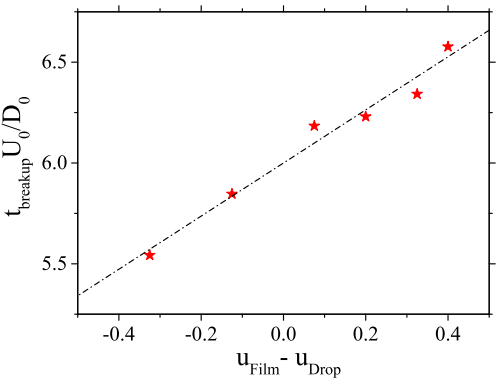

Figure 4.9: Dimensionless break up time as a function of the concentration gradient

Blue is injected, the resulting wall film will have a higher urea concentration than *AdBlue* with increasing time. In the exhaust gas system the effect of high temperatures and also temperature gradient influence additionally the hole formation, which need to be investigated in the future. Therefore, it can be assumed that in the exhaust gas system the formation of holes starts very early, which leads to an additional atomisation.

4.4 Conclusions

This chapter focuses on the expansion and propagation of the corona produced by the drop impact onto an inclined flowing wall film. Viscosity, relative film thickness and the impact angle are varied in the experiments to identify the main influencing factors governing inclined drop splash. It is interesting that the effect of drop viscosity and relative film thickness on the corona propagation is minor. The geometry of the corona is highly dependent on the angle of inclination. Furthermore, the corona threshold is dependent on the angle of inclination. Additionally, the dynamics of corona expansion are modelled theoretically. It is described as a propagation of the kinematic discontinuity [149, 158, 202]. A semi-empirical model is developed for the evolution of the corona base, which predicts the rear and frontal jet coordinate, X_r and X_f, as a function of the angle of inclination and the relative film thickness. The agreement between the theory and the experiments

is rather good.

In case of different water-urea solutions as drop and wall film liquid, the formation of holes can be observed for small relative film thicknesses. The concentration difference of drop and wall film seem to lead to Marangoni-driven flows and finally to the formation of holes. The corona completely collapses due to the hole formation.

5 Description of drop splashing

In this chapter the focus is on splashing resulting from drop impact on wetted walls and soft substrates. The splashing threshold is discussed and determined. Section 5.1 discusses the principles of splashing resulting from drop impact onto liquid films. Three different regimes related to the viscosity ratio are determined for the splashing threshold. In Section 5.2 the splashing threshold in the case of drop impact on soft substrates is determined. Parts of this chapter have been published in [90, 92], including the text and figures.

5.1 Mechanisms of splashing on a wetted solid substrate

In this study four different impact outcomes have been observed as shown in Chapter 3. In order to understand the dynamics of drop impact and to be able to develop a theoretical model predicting the impact outcome, the influencing parameters are identified and their effects are determined in Chapter 3.1.1. Summarising as shown in Chapter 3.1.1 a higher initial drop diameter and impact velocity enhance splashing, a thicker wall film and higher kinematic viscosity approximately prevent splashing. The effect of viscosity on splashing is discussed in the following.

5.1.1 Enigmatic viscosity effect on splash

Several experiments [13, 17, 158] demonstrate that for high Reynolds number the viscosity influence on the corona spreading is minor. On the other hand, the size of the secondary droplets produced by splashing of an impacting spray on a wall, is scaled well by the size of the viscous boundary layer developing under the spreading lamella, which is expressed in [155] in the form

$$\frac{D_{\text{secondary}}}{D_{\text{primary}}} \sim Re^{-1/2}. \tag{5.1}$$

Moreover, the use of the K number, defined in Eq. (1.28), for quantifying the splashing threshold is justified in [42], also using the concept of the viscous boundary layer. The effect of viscosity on the splashing threshold and on the mechanism

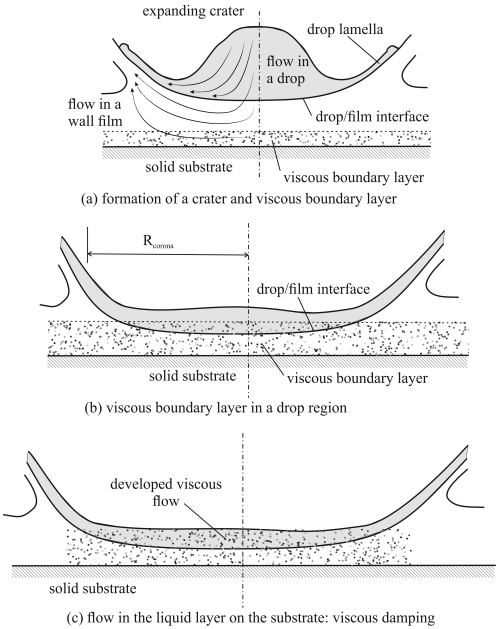

Figure 5.1: Consecutive stages of drop impact onto a wetted substrate: (a) initial drop deformation and penetration into the wall film, inception of the viscous boundary layer on the wall; (b) boundary-layer growth leads to intersection with the drop/film liquid interface; (c) liquid layer in the crater is thinner than the viscous boundary layer. Reprinted figure with permission from [92]. Copyright 2018 by the American Physical Society.

of splash is thus unequivocal, if perhaps not very transparent. Why then does the viscosity not strongly affect corona spreading? This question will be addressed in the following with the aid of Fig. 5.1.

At the initial stage of corona expansion the viscosity influences only the formation and growth of a viscous boundary layer near the substrate. When the thickness of the boundary layer is much smaller than the thickness of the spreading lamella, the influence of the viscosity on the kinematics of drop impact and corona expansion is minor. This situation is the same for the case of drop impact onto a dry substrate (considered in [153],[150]) and a wetted substrate, as shown schematically in Fig. 5.1.

Assuming that splash occurs when inertial effects, associated with flow disturbances in the corona, are much larger than capillary effects [202]. The pressure associated with the inertial effects can be estimated as $p_{\text{inert}} \sim \rho u_r^2$. The pressure associated with surface tension is estimated using the Young-Laplace equation $p_\sigma \sim \sigma \partial h/\partial r^2 \sim \sigma h_{\text{lam}}/R_{\text{corona}}^2$. The condition for splash, $p_{\text{inert}} \gg p_\sigma$, with the help of Eqs. (3.4) and (3.6) can be expressed in the form

$$\frac{D_0 \text{We}}{h_{\text{lam}}(t)} \gg 1, \tag{5.2}$$

valid for long times, $t \gg \tau D_0/U_0$.

The thickness of the lamella $h_{\text{lam}}(t)$ reduces with time. The instant at which splash occurs can be estimated from Eqs. (5.2) and (3.5) as $t_{\text{splash}} \sim D_0/U_0$. The corresponding lamella thickness is $h_{\text{splash}} \sim D_0 We^{-1}$.

On the other hand, at larger times the boundary-layer thickness becomes comparable with the lamella thickness. At these times the inviscid solution (3.5) is no longer valid. The flow is damped by viscosity and the velocity field vanishes. This situation leads to the appearance of a nearly stationary residual wall film.

The similarity solution for the expansion of the viscous boundary layer has been obtained in [150] for the case of drop impact onto a dry smooth substrate. It is obvious that the same analysis can be applied to the case of drop impact onto a wall layer of the same liquid, since it is unimportant whether the fluid exists on the wall before impact or arrives with the drop, a boundary layer still develops. The thickness of the lamella, determined in Eq. (3.5) for large times, is scaled as $h_{\text{lam}} \sim D_0^3 U_0^{-2} t^{-2}$, while the thickness of the viscous boundary layer scales as $h_{\text{visc}} \sim \sqrt{\nu t}$. Therefore, the time at which the viscous boundary layer reaches the free surface of the lamella, $h_{\text{lam}} = h_{\text{visc}}$, can be estimated as $t_{\text{visc}} \sim D_0/U_0 Re^{1/5}$. The thickness of the wall film at this instant is correspondingly $h_{\text{visc}} \sim D_0 Re^{-2/5}$. In the experimental study [182] this scaling has been successfully confirmed. The measured and computed residual film thickness at the bottom of the crater is proportional to h_{visc} and depends also on the relative initial thickness of the wall film.

An impacting drop splashes when the residual lamella thickness, which is scaled well by h_{visc}, is smaller than the critical lamella thickness h_{splash}. It can be shown that the threshold condition $h_{\text{visc}} = h_{\text{splash}}$ leads to

$$\text{WeRe}^{2/5} \gg 1, \tag{5.3}$$

This condition is very close to the widely used threshold criterion $K > K_{\text{splash}}$, which allows us to assume that our description of the mechanisms of splash accounts for the main physical factors.

5.1.2 Evolution of the drop/liquid interface at large times: Drop and film liquids are the same.

At large times, the flow in the spreading lamella includes two layers, that of the drop and that of the film. The velocity field is described using the similarity solution [150]

$$u_r = \frac{r}{t} f' \left[\frac{z}{\sqrt{\nu t}} \right], \quad u_z = -\frac{2\sqrt{\nu}}{\sqrt{t}} f \left[\frac{z}{\sqrt{\nu t}} \right]. \tag{5.4}$$

where $\xi \equiv z/\sqrt{\nu t}$ is the similarity variable.

The velocity field satisfies the continuity equation. The dimensionless function $f(\xi)$ is obtained from the momentum balance equation [150] and has to satisfy the boundary conditions

$$f(0) = 0, \quad f'(0) = 0, \quad \lim_{\xi \to \infty} f'(\xi) = 1. \tag{5.5}$$

It has been shown in Section 5.1.1 that the height h_i of a liquid interface at long times approaches a residual thickness, which is scaled as $h_i = \chi(\delta) D_0 Re^{-2/5}$, where $\chi(\delta)$ is a dimensionless constant. This conclusion is valid also for the drop/liquid interface. The constant χ is determined by the relative initial film thickness δ. The value of ξ corresponding to the height $z = h_i$ is small at large times. Therefore, the velocity profile can be linearized, $f(\xi) \approx B\xi^2/2$, where $B = f''(0)$. Correspondingly, the velocity and the shear stress at the drop/film interface are

$$u_{ri} = \frac{B\chi D_0^{3/5} r}{\nu^{1/10} t^{3/2} U_0^{2/5}}, \quad \tau_i = \frac{B\rho\sqrt{\nu} r}{t^{3/2}}, \quad \text{at} \quad z = \chi \frac{D_0^{3/5} \nu^{2/5}}{U_0^{2/5}}. \tag{5.6}$$

In the case when the liquids of the drop and of the wall film are the same, the velocity and the shear stress near the drop/film interface are smooth, continuous functions.

5.1.3 Splashing threshold: Drop and film of different liquids

When the drop and wall film are different liquids the similarity solution described in Section 3.3.2 is not valid for larger times, when the thickness of the viscous boundary layer is of the same order as the height of the drop/film interface.

Viscosity of the film is much larger or much smaller than the viscosity of the drop liquid If the viscosity of the drop is much larger than the viscosity of the wall film, the time t_{visc} is determined mainly by the time the viscous boundary-layer takes to propagate into the film region. In this case it is possible to assume that the splashing threshold is determined mainly by the properties of the wall film liquid. The limiting case of such a situation is an impact of a solid particle onto a wetted wall.

Analogously, if the viscosity of the wall film is much larger than the viscosity of the drop, the time for the viscous boundary-layer expansion in the film layer is much shorter than the time of boundary-layer expansion in the drop. In this case we can assume that the splashing threshold is determined mainly by the drop properties.

It is therefore prudent to define two dimensionless K numbers

$$K_{\mathrm{d}} = We_{\mathrm{d}}^{1/2} Re_{\mathrm{d}}^{1/4}, \quad K_{\mathrm{f}} = We_{\mathrm{f}}^{1/2} Re_{\mathrm{f}}^{1/4}, \tag{5.7}$$

where the subscripts d and f denote the use of the drop or wall film liquid properties respectively.

The experimentally obtained outcome map for drop impact is shown in Fig. 5.2 for the range of the dimensionless thickness of the initial wall film $0.036 < \delta < 0.29$ and for the range of the viscosity ratio $10^{-4} < \kappa < 10^{4}$. Two splashing regions can be clearly identified. Region I defined by $\mathrm{K_d} < 80$ and $\mathrm{K_f} > 155$ corresponds to the case when the viscosity of the drop is much higher than the viscosity of the film. The splashed liquid consists mainly of liquid from the wall film.

Region II, associated with $\mathrm{K_d} > 135$ and $\mathrm{K_f} < 70$, corresponds to conditions when the wall film viscosity is much larger than the drop viscosity. Then the splashed liquid consists of liquid from the drop.

When the viscosity of the drop and the wall film liquids are of the same order of magnitude, the splash cannot be described by $\mathrm{K_d}$ and/or $\mathrm{K_f}$ separately. Further analysis is required for this range of parameters, which is designated Region III in Fig. 5.2.

The properties of both liquids are of the same order of magnitude, $\kappa \approx 1$ Consider a similarity solution for the flow in the drop and in the wall film at large times. The type of this similarity is the same as described in Section 5.1.1. The solution has to satisfy the continuity of the radial velocity and of the shear stress at the drop/film interface. This condition can be written with the help of Eq. (5.6)

$$\frac{B_d \chi_d}{{\nu_d}^{1/10}} = \frac{B_f \chi_f}{{\nu_f}^{1/10}}, \quad B_d \rho_d \sqrt{\nu_d} = B_f \rho_f \sqrt{\nu_f}, \tag{5.8}$$

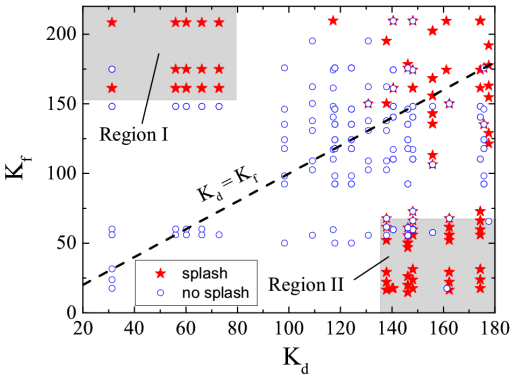

Figure 5.2: Map of the experimentally observed outcomes of drop impact. Region I of splash occurrences corresponds to very viscous drops, and Region II corresponds to splash occurrences on a very viscous wall film. The relative film thickness varies in the range $0.036 < \delta < 0.29$ and the viscosity ratio in the range $10^{-4} < \kappa < 10^{4}$. Reprinted figure with permission from [92]. Copyright 2018 by the American Physical Society.

where B_d and χ_d are dimensionless constants determining the solution in the drop layer, while B_f and χ_f determine the solution in the wall film layer.

The roots of the system of linear equations (5.8) are

$$\chi_d = \chi_f \frac{\rho_d \nu_d^{3/5}}{\rho_f \nu_f^{3/5}}, \quad B_f = B_d \frac{\rho_d \nu_d^{1/2}}{\rho_f \nu_f^{1/2}}. \tag{5.9}$$

The constant positive displacement Δ of the velocity field in the drop layer in the axial direction due to the difference in viscosity in the film can be found using the expression for h_i from (5.6) and the expression for χ_d from (5.9)

$$\Delta = \chi_f \frac{D_0^{3/5} \nu_f^{2/5}}{U_0^{2/5}} - \chi_d \frac{D_0^{3/5} \nu_d^{2/5}}{U_0^{2/5}} = \chi_f \frac{D_0^{3/5} (\mu_f - \mu_d)}{U_0^{2/5} \rho_f \nu_f^{3/5}}. \tag{5.10}$$

It can be shown that the residual film thickness is determined by the dimensionless parameter $\Delta/(D_0 Re_d^{-2/5})$, associated with the difference of the liquid viscosities.

In the case when the densities of the liquids are comparable, the dimensionless parameter can be reduced to

$$\frac{\Delta}{D_0 Re_d^{-2/5}} \sim \frac{\kappa - 1}{\kappa^{3/5}}. \tag{5.11}$$

Next, since the viscosities of two liquids are comparable, the flow in the corona consists of both liquids. The capillary pressures in the film and in the drop liquids are determined using the Young-Laplace equations: $p_{\sigma d} \approx \sigma_d h / R^2_{\text{corona}}$ and $p_{\sigma f} \approx \sigma_f h / R^2_{\text{corona}}$, respectively. The splash therefore occurs first in the region with smaller surface tension. Following this assumption the effective splashing parameter can be defined:

$$K^* = Re_d^{1/4} We^{*1/2}, \quad We^* = \frac{(\rho_f + \rho_d) D_0 U_0^2}{2 \min\{\sigma_d; \sigma_f\}}. \tag{5.12}$$

It should be noted that the flow in a spreading drop is influenced also by the interfacial tension σ_{df}. The value of σ_{df} and the pressure difference $p_{\sigma d} - p_{\sigma f}$ determine the curvature of the drop/film interface near any triple point common to two liquids and gas. Following this assumption the effect of the interfacial tension σ_{df} on the splashing threshold is negligibly small and is not considered in this study.

Since the densities of all the liquids in the experiments are comparable, it is not possible at this stage to identify experimentally the influence that a density difference may have on the impact. Therefore, in the present case simply an average density is used for computing the Weber number We* in Eq. (5.12).

The map of the drop impact outcomes shown in Fig. 5.3 is based on experimental data for impacts of drops onto a wall film with comparable viscosity. The range of the relative initial wall film thickness is $0.05 < \delta < 0.22$. This range is chosen, since for the same drop and wall film liquids the threshold value of the K number depends in this range only very weakly on δ [146]. The data belonging to the Region I and Region II (determined from Fig. 5.2) are excluded from the graph. It is evident from this map that the splashing threshold is determined by the dependence of the critical number K* on the viscosity ratio parameter $(\kappa - 1)/\kappa^{3/5}$.

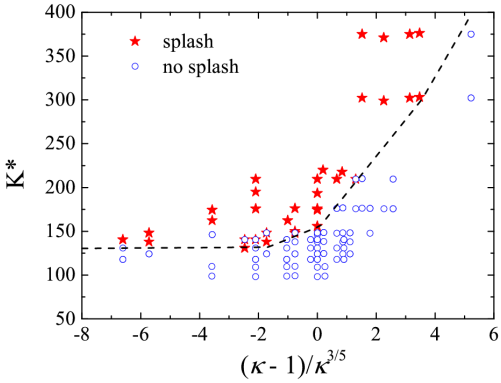

Figure 5.3: Map of the experimentally observed outcomes of drop impact for Region III, when the viscosities of the drop and wall film liquids are comparable and $K_d > 100$ and $K_f > 100$. The relative initial wall film thickness varies in the range $0.05 < \delta < 0.22$. The data belonging to the Regions I and II (determined from Fig. 5.2) are not included. Reprinted figure with permission from [92]. Copyright 2018 by the American Physical Society.

5.1.4 Influence of splashing on pre-ignition in combustion engines

Pre-ignition (PI) is the premature and uncontrolled flame initiation in combustion engines and is a significant problem in the development of spark ignited engines. Pre-ignition is an abnormal combustion, which hinders progress in engine downsizing and therefore inhibits the development of more efficient engines. This phenomenon is mainly observed in highly turbo charged spark ignited (SI) engines in the full load regime at low engine speeds. This leads to extremely high peak pressures, which can potentially cause severe engine damage [94].

The mechanisms, which trigger pre-ignition events, are not fully understood. However, it can be assumed that a multi phase process is responsible for the pre-ignition event. The interaction between the injected fuel spray and the oil film on the cylinder wall can influence the occurrence of pre-ignition. Under certain conditions, splashing can occur and leads to the formation of secondary droplets, which can contain both liquids. These multicomponent droplets can lead to pre-ignition at the droplet surface towards the end of the compression phase. The

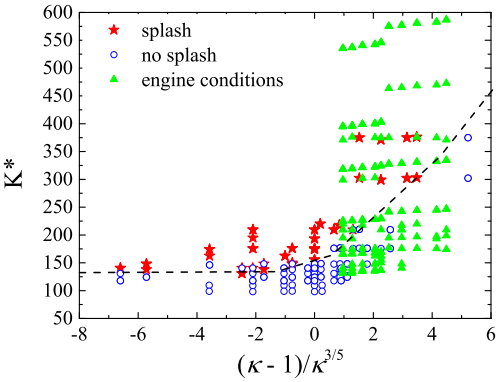

Figure 5.4: Map of the experimentally observed outcomes of drop impact for Region III compared with typical engine conditions. The relative initial wall film thickness varies in the range $0.05 < \delta < 0.22$.

content and distribution of multicomponent droplets is discussed in more detail in Chapter 7.

After initiation of the ignition self-ignition occurs resulting from ignition sparks in the end gas area in the case of knocking. Large pressure gradients and peak pressures occur due to high heat release rates. Since motor oil has a higher ignition propensity than fuel, under certain conditions self-ignition can occur [52, 85, 100, 120, 130]. However, in contrast the enthalpy of vaporization can cause local cooling. Takeuchi et al. [169] and Luef et al. [99] focused on the influence of the base oil composition and additives. Furthermore, they have shown that particularly low viscosities and high calcium content can promote pre-ignition events. Low viscosity enhances detaching of droplets from the lubricating oil film, while the influence of calcium is not clear yet. Moriyoshi et al.[126] assumed that a chemical conversion involving an exothermic reaction can cause pre-ignition. Luo et al. focused on the influence of the oil on the turbocharger lubrication and the crankcase ventilation on pre-ignition [113]. No direct proof of ignition due to oil droplets, such as imaging, has been published so far. Many studies show the dependency of the pre-ignition rate on the fuel/motor oil interaction [66, 72, 79, 113, 204]. The deposition of fuel on the cylinder wall varies with the timing of the injection. The motor oil can be enriched by fuel over time, which leads to different properties of the film on the cylinder wall. In general, splashing becomes more likely resulting

from decreasing viscosity and surface tension. Magar et al. [116] assumed that the mixture of oil and fuel is deposited on the top land and finally detaches from the head land due to inertial forces during piston deceleration in the compression stroke. This could subsequently lead to a pre-ignition [84].

In order to understand the possible connection between drop impacts resulting in splashing and pre-ignition, typical properties of the fuel drop and oil film found in the engine are compared with the results from the generic drop impact experiments by using dimensional analysis. The Sauter mean drop diameter in fuel spray of $D_{32} = 15 - 30$ μm, film thicknesses in the range of $h = 2 - 10$ μm and impact velocities of $U_0 = 10 - 20$ m/s as impact parameters are used. Isooctane and RON 95 E10 is used as a drop liquid and for the wall film 5W-30 and 15W-50 motor oil. The experimental results from Section 5.1 are compared with dimensionless data obtained by dimensional analysis for the typical combustion conditions in Fig. 5.4. It can be seen that both regimes, splash and no splash, can occur. Especially for higher relative film thicknesses splashing occurs rather rarely. Nevertheless, with an increase of K^*, splashing occurs preferentially. Increasing the drop diameter or the impact velocity, as well as decreasing the film thickness enhances splashing, which is already shown in Chapter 3. Especially, the film thickness of the oil film influences the impact outcome in this case. Increasing the oil film thickness decreases the probability of splashing. Therefore, the film thickness of the oil film should be rather big, to prevent pre-ignition. Furthermore, a very fine fuel spray with consequently very small drops will rather rarely lead to splashing. Smaller drops would lead to a smaller impact velocity additionally. Nevertheless, with increasing impact velocity of the drops splashing cannot be prevented at some point anymore. Increasing viscosity of the wall film decreases the probability of splashing. However, the impact parameters like film thickness predominate the impact outcome concerning the engine conditions. For this comparison, the temperature is only considered in the fluid properties, since these are dependent on the temperature. Further temperature effect, especially in the range, which can be found in the combustion engine, cannot be neglected for a fundamental understanding. Nevertheless, this comparison, under which conditions splashing occurs or not, can be helpful in preventing pre-ignition [94].

5.2 Mechanisms of splashing on a soft substrate

Drop impact onto dry substrates can also result in splashing. The properties of the impact substrate influence significantly the impact outcome. Similar to splashing resulting from drop impact onto a wetted wall, *prompt splash* and *corona splash* can be observed.

At large times the viscous stresses near the wall lead to flow damping in the spreading lamella. The residual film thickness is determined mainly by the impact velocity and liquid viscosity as described in Section 1.3.3. The expression for the dimensionless residual thickness, $h_{\text{res}} = D_0 Re^{-2/5}$ has been obtained in [153] from the exact solution for the expansion of the boundary layer and the long-time solution for the viscous flow in the lamella and is discussed in Section 1.2.

The typical pressures governing the splash phenomena, can be estimated in the lamella: pressure associated with the liquid inertia, $p_i \sim \rho U_0^2$, and the pressures associated with the capillary forces. The capillary pressures has been estimated in [202] as $p_{\sigma 1} \sim \sigma h_\nu / D_0^2$, with the viscous length scale $h_\nu \sim D_0 Re^{-1/2}$. The capillary pressure can be expressed by the length scale associated and the residual lamella thickness, $p_{\sigma 2} \sim \sigma / h_{\text{res}}$.

The corona formation from the spreading lamella and the following splash can be observed if the pressure associated with inertia is much larger than both capillary pressures. If the ratio of the inertial and capillary stresses is much larger than unity, the splashing conditions is given by [202]

$$\mathrm{K} = \left[\frac{p_i}{p_{\sigma_1}}\right]^{1/2} = \mathrm{We}^{1/2}\mathrm{Re}^{1/4}, \quad \mathrm{L} = \frac{p_i}{p_{\sigma_2}} = \mathrm{WeRe}^{-2/5}, \tag{5.13}$$

Existing experimental data was used to describe a splashing threshold for impact outcome on dry solid substrate as shown in Fig. 5.5. The deposition/corona splash boundary can be indeed described by the curves $\mathrm{K} = 84.0$ and $\mathrm{L}_{\text{dry}} = 12.0$. For larger Reynolds numbers also the prompt splash is observed. In this region of impact parameters also the substrate roughness [156] and the aerodynamic forces [196] play significant role. However, the results, presented in this chapter, do not agree with the regime map shown in Fig. 5.5.

Different outcomes of drop impact onto soft, deformable substrate S1 (defined in Table 2.3) are shown in Fig. 5.6 for the liquids of different viscosities. It can be seen that for relatively high Reynolds number the deposition/corona splash boundary can also be described well by the condition $\mathrm{L} = \text{const}$. However, in this case the splashing threshold is $\mathrm{L}_{\text{soft}} = 16.8$. Therefore, the critical threshold value is larger than the corresponding threshold for a dry solid substrate $\mathrm{L}_{\text{dry}} = 12.0$ shown in Fig. 5.5. This indicates that the mechanisms of splash are similar, but

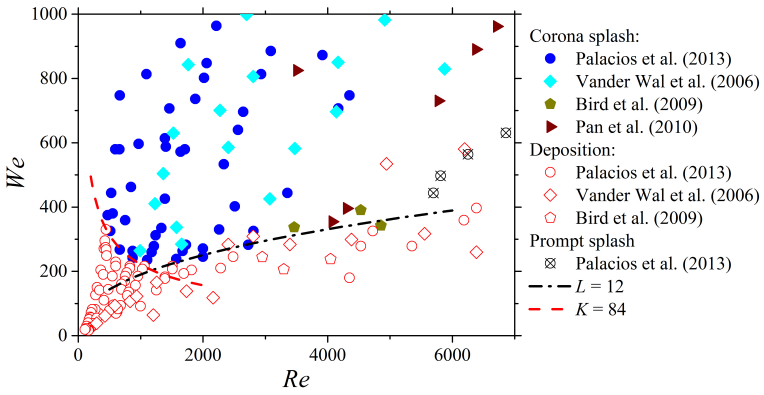

Figure 5.5: Regime map of outcomes for drop impact onto a dry solid substrate. The experimental data are from [16, 132, 135, 183]. The deposition/corona splash boundary is described by the curves K = 84.0 and L = 12.0. (Reprinted from [90].)

deformable surfaces suppresses splashing, which was also observed by Howland et al. [77].

For smaller Reynolds numbers the threshold on the deformable substrate yields $We_{soft} = 410$. In this region the splashing threshold is independent on the liquid viscosity due to aerodynamic effects close to the advancing contact angle.

An expression for the splashing threshold is developed from the balance of the aerodynamic lift force and the inertia of the liquid in the lamella in the recent study of Riboux et al. [145]. The viscosity of the surrounding gas is included in this expression. For smaller Ohnesorge numbers the predicted splashing threshold does not depend on the liquid viscosity, which agrees with the observations in this study. However, for higher Reynolds numbers the viscous and capillary forces are probably significantly higher than the aerodynamic forces and the splashing threshold is described well by a constant L value [90].

Interestingly, no clear difference can be found on the onset of the splashing phenomena on S2, S3 and S4 with various material properties. Although the substrates vary in shear modulus, which are significantly lower than S1 Table (2.3), no difference in the outcome can be observed. All observed outcomes are presented in Fig. 5.7 for the different mixing ratios of the substrates. Besides the partial rebound phenomena only observed on S1 no further outcomes can be observed

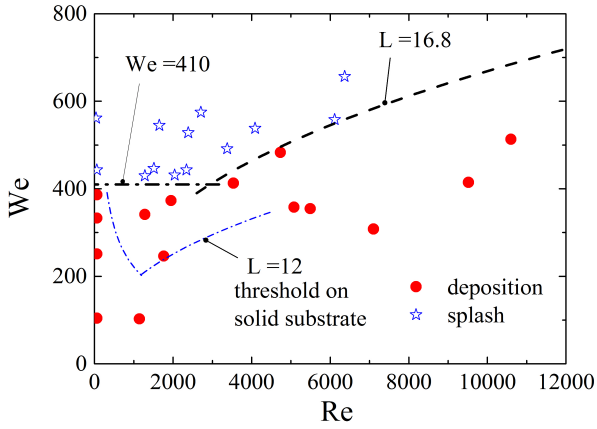

Figure 5.6: Map of outcomes of the drops of different viscosities, impact diameter and velocity impacting onto a deformable substrate S1 from Table 2.3. The impact parameters are $U_0 = 1.32, 2.05, 2.9, 3$ and 3.45 m/s, $D_0 = 2.3$ and 3 mm. The deposition/corona splash boundaries are compared with the corresponding boundaries for dry solid substrate, shown in Fig. 5.5. (Reprinted from [90].)

on the different deformable substrates. All substrates, independent on their viscoelastic properties, behave as an elastic object. Therefore, no influence of the specific softness of the substrate can be observed, once the splashing threshold is exceeded. This observation is in contrast to the work of Howland et al. [77]. When a droplet impacts and spreads on the surface, a stress rises on the surface with a frequency of $f = U/2\pi\epsilon$ [34]. The contact line velocity for an impacting droplet with $D_0 = 2.3$ mm and $U_0 = 3$ m/s yields $U = 4$ m/s. Considering this velocity and the cut-off length $\epsilon = 1$ μm the calculated frequency yields 0.6 GHz. The angular velocity corresponding to this frequency is $3{\times}10^6$ rad/s, which is far beyond the measuring capacity of any commercially available rheometer. Nevertheless, at such fast deformation the material property predominates the response to the stress in the storage modulus G'. Therefore, above the splashing threshold no influence on the impact outcome can be observed. Similar observations for the initial stages of the drop spreading phenomena governed by inertia were made by Chen et al. [34]. The drop spreading is analysed with a characteristic spreading coefficient, which is not dependent on the softness of the substrate. In these expe-

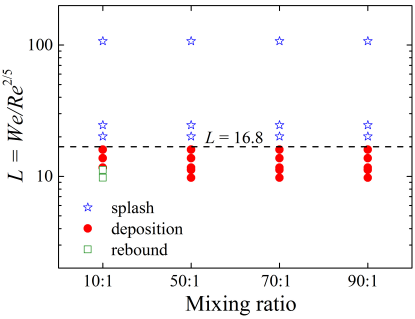

Figure 5.7: Regime map of the outcomes on various soft substrates. (Reprinted from [90].)

riments, increasing viscosity leads to the enhancement of splash. This is the case when the splashing is bounded by the constant L number [90].

5.3 Conclusions

The mechanisms of splashing on wetted and soft substrates are described and finally new scalings describing the splashing threshold are introduced in this chapter.

In the case of the wetted wall three regions of splash are identified. In Region I (associated with the case $\kappa \ll 1$) the splash is determined by the K_f number based on the properties of the wall film. In Region II (associated with the case $\kappa \gg 1$) the splash is determined by the K_d number based on the properties of the drop liquid. In the Region III a new scaling is introduced, which is based on the assumption that splashing is initiated in the liquid layer with smaller surface tension. The threshold K^* number is a function of the dimensionless term $(\kappa - 1)/\kappa^{3/5}$. These results are of a predictive nature.

This description of the splashing threshold is used to predict splashing for some common engine conditions. Both regimes, splash and no splash, can occur. This leads to the assumption that the single drop impact resulting in splashing can be on of the reasons of the engine pre-ignition. However, it cannot be only explained by drop splashing, further possible effects can be the PI rate increase with decreasing coolant temperature and late ignition timing. Additional experiments are required to understand the mechanisms leading to initial PI. However,this compa-

rison, under which conditions splashing occurs or not, can be helpful in preventing pre-ignition.

For drop impacts on soft substrates the splashing threshold is shifted towards higher Weber number and lower Reynolds number. No dependency of the softness of the substrate is observed once the threshold is exceeded. This can be explained by the rheology of the substrates at extremely high stresses. Since the response of all substrates is comparable, comparable outcomes are observed.

6 Description of the corona detachment

Next to the two known types of splashing, prompt splash and corona splash, a new phenomenon of splashing has been observed in this study. Corona Detachment, as shown in Fig. 6.1, occurs only under certain conditions as small film thicknesses and miscible liquids. In this chapter the phenomenon *corona detachment* is shown and discussed.

6.1 Observations of the detachment of the corona from the wall film

Drop impact leads to corona splash, corona expansion without splash or deposition and splash without corona. The splash without corona has been observed before [146, 164] and [63], but no clear explanation of the formation of the secondary droplets has been provided. In fact the "splash without corona" is a limiting case of the corona detachment phenomenon, which has been observed in this study.

The splashing resulting from the corona detachment can be observed in combination with both basic phenomena, forming of a corona and splashing. In both cases the corona detachment occurs after reaching the maximum crown diameter. If there is no previous splashing, the corona rises up and reaches a maximum crown diameter, as can be seen in Fig. 6.1. The rim begins to fall already when the corona starts to detach from the bottom. The detachment starts at one point of the corona base and rises up. It is rather fast until it reaches the rim of the corona. The detached fluid of the corona partially atomizes into very fine droplets and then merges with the rim. The free rim breaks up into a number of relatively large drops.

In some cases the rim instability leading to splashing starts before the corona detachment, as shown in Fig. 6.2. In this case, corona detachment acts as a second atomisation leading to very fine secondary droplets.

Corona detachment can only be observed in a narrow range of parameters, such as a small relative film thickness ($\delta < 0.1$) and the miscibility of both liquids. Hereby, corona detachment can result from drop impact onto thin wall films of the same liquid, as shown in Fig. 6.2, as well as on wall films of a different liquid, as shown in Fig. 6.1, as long as both liquids are miscible. Since corona detachment

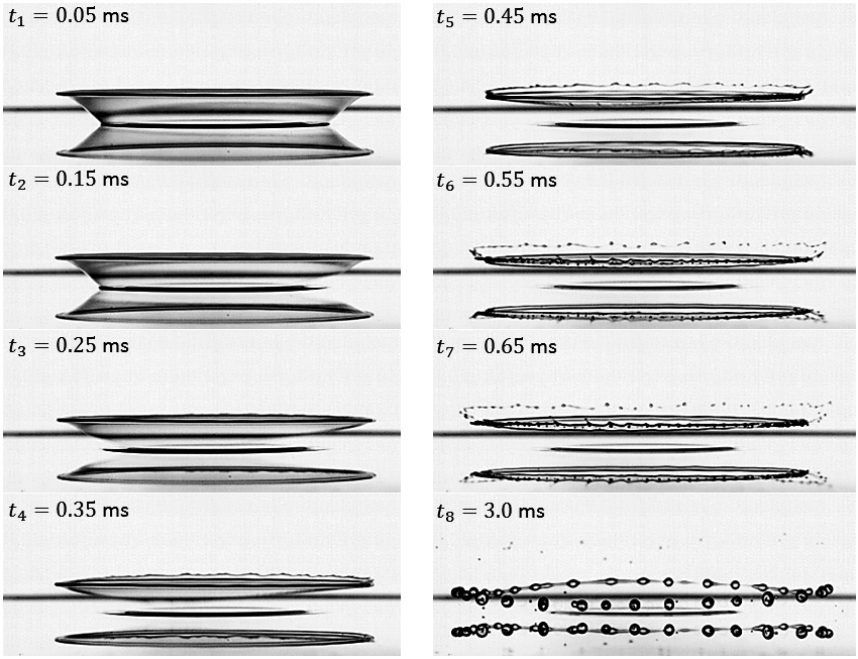

Figure 6.1: Example of the corona detachment for $\kappa = 0.5$, $\delta = 0.05$ and $U_0 = 3.2$ m/s. A S20 drop impacts onto a S10 film, both liquids are miscible.

can also be observed for combinations of the same liquid and therefore no concentration or respectively surface tension/viscosity gradient occurs, the Marangoni driven instability, which triggers the hole formation in Section 4.8, is not applicable in this case.

For very high viscous wall films (from $\nu_f = 750$ mm^2/s up to $\nu_f = 100000$ mm^2/s) corona detachment can be observed independently from the wall film thickness. Comparable to the spreading behaviour on very viscous wall films described in Section 3.1.2, the high viscosity prevents the motion in the wall film. In Fig. 6.3 the detachment of the corona is shown from below. The rupture of the corona wall starting from the corona base can be identified very good. For very high viscous wall films the corona angle becomes very small and the detachment from the corona begins in contrast to less viscous wall films earlier. Nevertheless, the liquids of drop and wall film need to be miscible still.

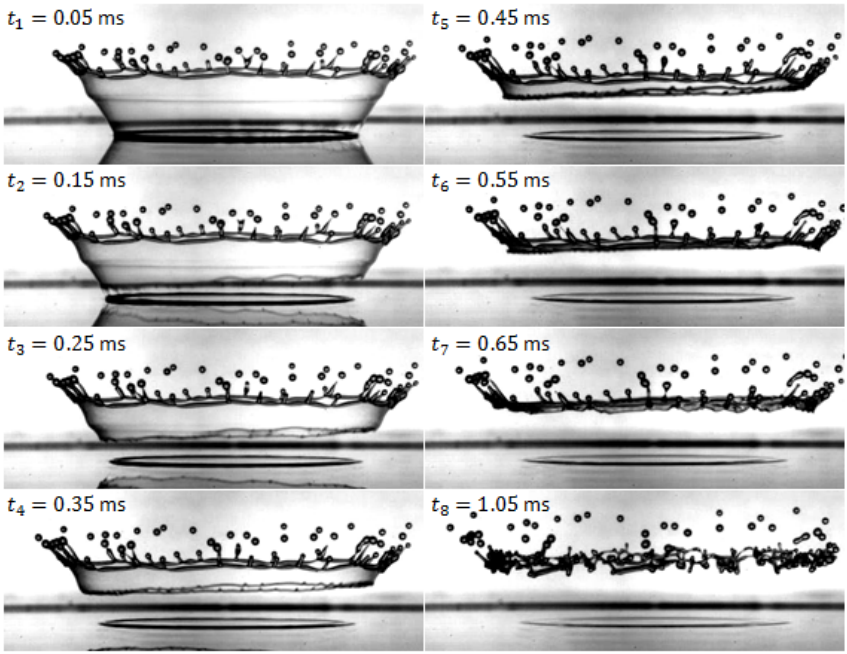

Figure 6.2: Example of the corona detachment during splash for $\kappa = 1$, $\delta = 0.045$ and $U_0 = 3.2$ m/s. A S5 drop impacts onto a S5 film, the liquids are miscible.

6.2 Corona splash by detachment from the wall film

The K_d number is introduced and defined in Eq. (1.27) using the properties of the drop liquid. In all cases the drop initial diameter D_0 is used as the length scale and the drop impact velocity as the velocity scale.

In Fig. 6.4 the number K_d is shown for the cases corresponding to the corona detachment as a function of the film thickness scaled by the viscous length in the film $\delta Re_f^{2/5}$. The cases leading to the corona splash and to the deposition are not shown in Fig. 6.4. The values for K_d corresponding to detachment in all the cases well exceed the splash/deposition limit $K_d = 2100$. Moreover, detachment phenomena are observed only in the cases $\delta Re_f^{2/5} < 1.2$. This means that detachment

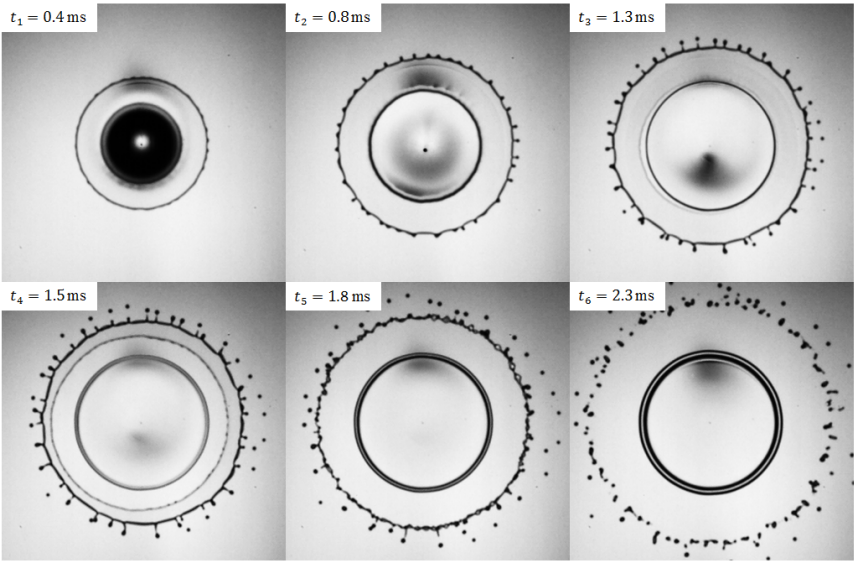

Figure 6.3: Observation of the corona detachment resulting from a S5 drop impacting onto a S10000 wall film from below for $\kappa = 20000$, $\delta = 0.045$ and $U_0 = 3$ m/s.

occurs in cases when the initial film thickness is of the same order or much smaller than the viscous length in the film $D_0 Re_f^{-2/5}$. Moreover, detachment occurs for cases when K_d is well above the splashing threshold.

As it have been shown in the previous subsection, the regime typical for the corona detachment (relatively thin film of a viscous liquid) is viscosity dominated. The detachment of the corona can be caused by a strong corona stretching. This stretching is the result of fast flow deceleration in the wall film at the times larger than t_{visc}. We can estimate the typical lamella velocity, $u_{\mathrm{visc}} = R_{\mathrm{visc}}/t_{\mathrm{visc}}$ with the help of (3.7)

$$u_{\mathrm{visc}} = U_0 Re^{-1/10}. \tag{6.1}$$

The characteristic corona stretching can be therefore estimated as $\dot{\gamma} = u_{\mathrm{visc}}/h_{\mathrm{visc}}$, which yields the following expression for the stretching rate

$$\dot{\gamma} = \frac{U_0}{D_0} Re^{3/10}. \tag{6.2}$$

The corona breakup is governed also by capillary forces. The typical time of

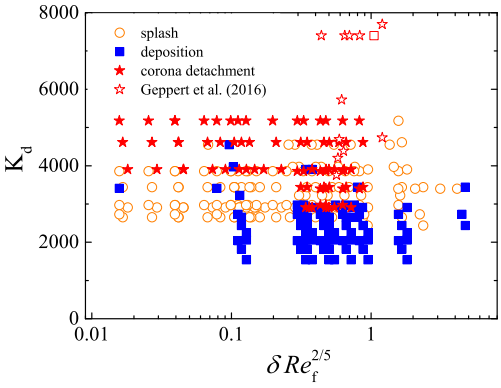

Figure 6.4: Drop impact leading to the corona detachment. Values of the K_d number for various film thicknesses, scaled by the viscous length: $\delta Re_f^{2/5}$. The experimental data are from the present study ★ and from [63], marked by open stars ☆. Other types of outcomes are also shown in the graph.

capillary breakup is $t_\sigma = \sqrt{\rho h_{\text{visc}}^3/\sigma}$. The dimensionless stretching rate P_d which can govern the corona breakup near the wall film, leading to its detachment can be now defined

$$P_d \equiv \dot{\gamma} t_\sigma = \tilde{We}^{1/2} Re_d^{-3/10}. \tag{6.3}$$

Here it should be noted that the instant of the corona detachment is not exactly repeatable even if the experiments are repeated with the same parameters. This fact indicates that the mechanism of the detachment is triggered by flow perturbations.

The Weber number $\tilde{We}$ has to account for the different values of the surface tensions σ_d and σ_f of each liquid and of the interfacial tension σ_{df}. In these experiments the surface tension has not been varied in a wide range, therefore no accurate analysis of the effect of σ_d, σ_f and σ_{df} is possible. At this stage we assume that the value of σ_{df} determines the shape of the interface between the two liquids and does not significantly influence the process of detachment. Since surface tension tends to stabilize interfacial instabilities, we use the smallest value of surface tension $\tilde{\sigma} \equiv \min\{\sigma_d; \sigma_f\}$ in the definition of $\tilde{We}$.

The preferable breakup on a layer of the liquid with lower surface tension can be observed in the experiments. One example of a low surface tension oil drop

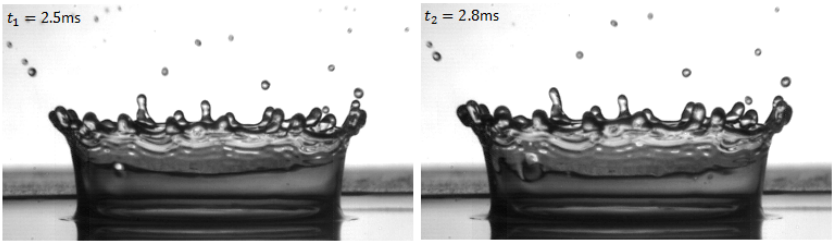

Figure 6.5: Example of the partial break up of an inner layer of the corona for $\kappa = 0.2$, $\delta = 0.22$ and $u = 3.2$ m/s. A S5 drop impacts onto a W film, both liquids are immiscible.

impacting a water layer is shown in Fig. 6.5. Several expanding holes in the internal layer, moving in the vertical direction, can be seen in the corona. The outer water layer is not yet broken.

The validity of this choice is justified by the results shown in Fig. 6.6.

The drop impact outcomes at different values of dimensionless stretching rate P_d and dimensionless viscosity ratio κ are shown in Fig. 6.6. The data shown in Fig. 6.6 includes the results from this study and the observations from [63].

The dependence of the outcome on the value of κ is based on the assumption that the influence of the film thickness is small if $\delta < 0.3$. This assumption is based on the fact that the splashing threshold is only weakly influenced by δ in this range ([146]) except for the smallest film thicknesses, $\delta < 0.05 \sim 0.1$. Moreover, the value of the residual film thickness is almost independent on the film thickness and approaches the corresponding value during drop impact onto a dry substrate [182].

At values of $\kappa > 10$ the corona detachment is observed over a relatively small range of stretching rates $2.8 < P_d < 3.3$. No other outcomes have been observed in this region for all film thicknesses δ and viscosity ratios κ. At smaller values of κ a clear window exists corresponding to the corona detachment. We should note that the detachment window $2.8 < P_d < 3.3$ is valid also for impacts onto the films $0.1 < \delta < 0.3$ for all the values of the viscosity ratio κ.

In addition to this detachment window a clear region exists in the P_d - κ map belonging to the detachment events.

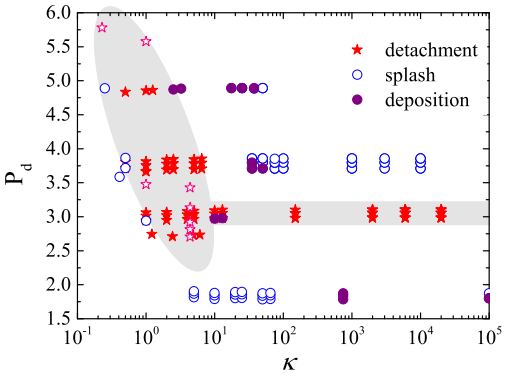

Figure 6.6: Values of the dimensionless stretching rate P_d number as a function of the viscosity ratio κ for relatively thin initial wall film thickness corresponding to $\delta Re_f^{2/5} < 1.2$. The experimental data for detachment are from the present study ★ and from [63], marked by open stars ☆.

6.3 Conclusions

Corona detachment can only be observed for a narrow range of parameters, such as a small relative film thickness and miscibility. It is shown that the phenomenon of corona detachment is not particularly unusual. Corona detachment from the wall film is governed by the dimensionless corona stretching P_d and viscosity ratio κ. Moreover, if the viscosity of the film is much larger than the viscosity of the drop, $\kappa > 10$, or the film thickness $\delta > 0.1$ the value of the characteristic stretching P_d, associated with detachment is in a constant narrow range $2.8 < P_d < 3.3$.

7 Multicomponent corona and secondary droplets

In the present chapter the distribution of the liquids of drop and wall film during the drop impact is discussed. In order to understand the dynamics of drop impact of different liquids, it is important to understand how both liquids act during and after the impact. First experiments with black dye can be found in [88]. This part of the study can be considered as an exploratory experimental study, which demonstrates the potential usability of the colour high-speed video technique for characterization of multicomponent drop impact.

7.1 Expansion of the multicomponent corona

The distribution of two liquids differs significantly, if both liquids are miscible or immiscible. While immiscible liquids have a distinct interface and corresponding interfacial tension, miscible liquids form a homogenous solution over time. Starting with immiscible liquids, both liquids can be clearly distinguished by dying the drop liquid. The interfacial tension of the water/silicone oil combination, which is used in the following, is $\sigma_{WS} = 51$ mN/m.

Figure 7.1 shows the temporal evolution of a dyed water drop impacting onto a silicone oil wall film. Starting with the rise of the corona the rim of the corona is transparent and therefore only consisting of the liquid of the wall film. With increasing instability of the rim, the finger-like jets consist also at the end of jets only of the wall film liquid, followed by the liquid of the drop. The liquid of the drop is encapsulated by a thin layer of the wall film liquid. When the finger-like jets breakup into secondary droplets the first secondary droplets leaving the jets consists only of the wall film liquid. Afterwards secondary droplets consisting of both liquids can occur, whereby the liquid of the droplet is always encapsulated by the wall film liquid [91].

In most cases these droplets occur as a droplet in a droplet. In order to determine the content of the secondary droplets, a calibration method is introduced in Section 7.2.2. The observations of the calibration measurements using an acoustic levitator show that for water/silicone oil combinations the silicone oil is encapsulating the water drop, even if the drop appears only to contain the dyed water liquid

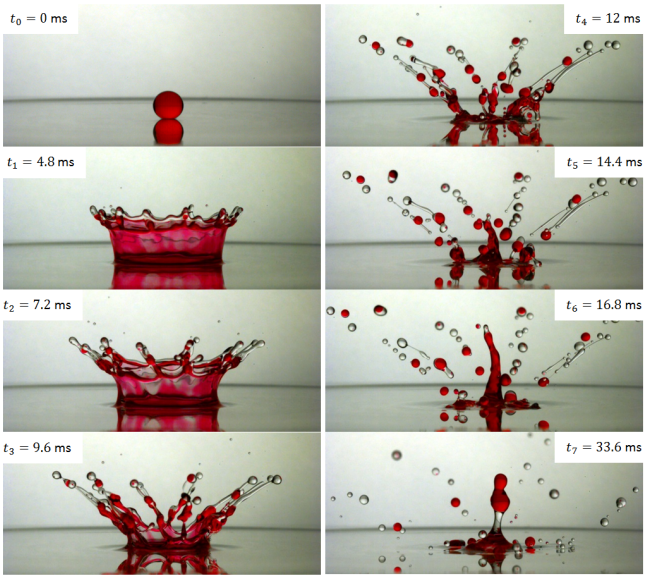

Figure 7.1: Temporal development of the corona of a dyed water droplet impacting onto a S10 wall film. The relative film thickness is $\delta = 0.18$.

due to the small shadow resulting from the imaging. This supports the assumption that either transparent (silicone oil in these experiments) or a mixed (containing both liquids) secondary droplets are formed.

In the case of partial rebound, the tip of the central jet consists in most cases of the wall film liquid. Comparable to the composition of the secondary droplets, the liquid of the drop is encapsulated by the wall film liquid, which is especially evident if a satellite droplet detaches from the central jet.

With increasing viscosity of the wall film the ratio of mixed secondary droplets is increasing. The content distribution seems to be dependent on the wall film viscosity.

If the viscosities of both liquids differ significantly, as shown in Fig. 7.1, the liquids act quite different. If the liquid of the drop is highly viscous, as in Fig. 7.1 (glycerine), the liquid of the drop rarely participates in the evolution of the corona and therefore the corona wall as well as the secondary droplets consist only of the wall film liquid. In this case the drop only suppresses the liquid of the wall film. Considering a high viscous drop as limiting case as already shown in Section 3.1.2 , the drop liquid is not participating in the corona formation and splashing, which

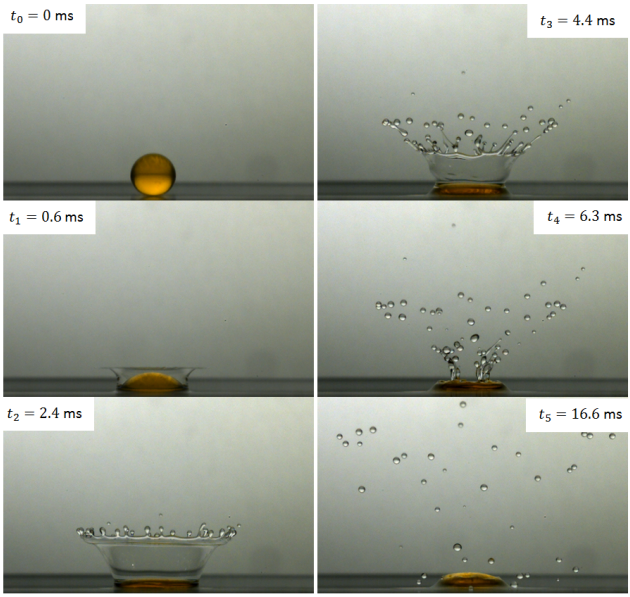

Figure 7.2: Temporal development of the corona of a dyed glycerine droplet on a S10 wall film. The relative film thickness is $\delta = 0.1$.

finally leads to secondary droplets only containing the wall film liquid. In this case the content distribution is mainly determined by the wall film liquid too. Considering in contrast the impact of a less viscous drop on a very high viscous wall film as limiting case, the wall film liquid will not participate into the formation of secondary droplets. Therefore, the secondary droplets will only contain of the drop liquid.

With increasing κ the wall film becomes more viscous and the total number of secondary droplets decreases in general. Furthermore, the ratio of secondary droplets containing the liquid of the wall film and containing both liquids reverses. Since for very low κ all secondary droplets only contain the liquid of the wall film, at a certain condition the ratio reverses from more secondary droplets containing only the liquid of the film to more secondary droplets containing both liquids. This shows the dependency of the wall film viscosity on the content distribution of the secondary droplets.

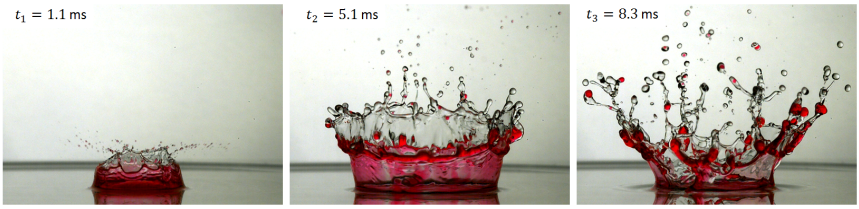

Figure 7.3: Temporal development of a double corona of a dyed water droplet impacting onto a S1 wall film with the relative film thickness $\delta = 0.2$, $U_0 = 3$ m/s and $\kappa = 1$.

7.1.1 Evolution of the double corona

In a few cases inside the main corona a further corona can be observed. This second corona consists of the drop liquid, which is dyed red. The rise of the *double corona* is shown in Fig. 7.3. This phenomenon was already observed in previous experiments, but first identified by this colour visualisation. The corona of the wall film rises much faster than the corona of the drop, resulting in a higher corona height. With increasing viscosity of the wall film the difference of the rim velocities of corona heights decreases. With increasing wall film viscosity the difference of both coronas decreases until both coronas rise with almost the same rim velocity.

The appearance of the double corona can be explained by the significant difference of the surface tensions of the drop and film liquids. In the case of the inertia dominated drop impact with $We \gg 1$, $Re \gg 1$, the corona appears as a kinematic discontinuity [202] on the wall film as a result of the interaction of the outer undisturbed film and radially spreading film in the inner region (inside the corona).

Nevertheless, the viscosity of the wall film seems to determine the height difference of both coronas until both coronas show almost the same height as shown in Fig. 7.4. The motion of a rim is determined by the balance of inertia of the liquid entering the rim and surface tension. The relative rim velocity [171] is $U_{\mathrm{rim}} = \sqrt{2\sigma/\rho h}$. In our case two rims on two liquid films are formed. Both rim velocities scaled by the impact velocity is shown in Fig. 7.5 over the dimensionless time.

The *double corona* was already observed, but not yet explained in few studies of Thoroddsen et al. [6, 174] and Shaikh et al. [163]. In the study of Thorordsen et al. the impact of viscous drops onto less viscous wall films for miscible liquids is investigated. High impact velocity and high drop viscosity lead first to the for-

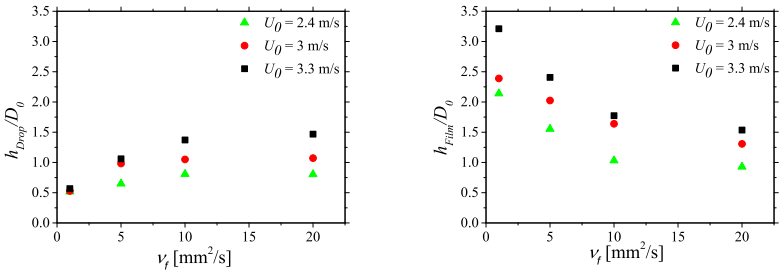

Figure 7.4: The corona height of the drop (a) and of the film (b) liquid scaled by the initial drop diameter as a function of the viscosity of the film for a relative film thickness $\delta = 0.2$.

mation of the wall film corona followed by the drop corona. Different length and time scales are also observed [174], but the formation process could be different. This shows that under certain conditions the double corona can also be observed for miscible liquids. Shaikh et al. observed the double corona for immiscible liquids, but focused in the study on the total distribution of the secondary droplets in general [163].

7.1.2 Distribution of the drop liquid in the wall film after drop impact

One further open question is, where the drop liquid goes during and after the drop impact. The distribution of the drop liquid is dependent on the miscibility of both liquids. Considering immiscible liquids as presented in the previous Section 7.1, a distinct interface can be observed. This interface separates both liquids from each other resulting in two parallel corona walls with the drop liquid within and the wall film liquid outsides. Therefore, during the expansion of the corona the drop liquid is centered bounded by the corona. In the receding phase of the corona the drop liquid merges back to the center of impact. This can be clearly observed in Fig. 7.6, in which the drop liquid is dyed with red colour. After the collapse of the corona, it can be seen, that the drop liquid is rather located close to the impact center in several secondary droplets floating on top of the wall film. In contrast to this behaviour, in Fig. 7.7 the temporal evolution of a water drop impacting onto a water film is shown. Since both liquids are miscible, immediately after the

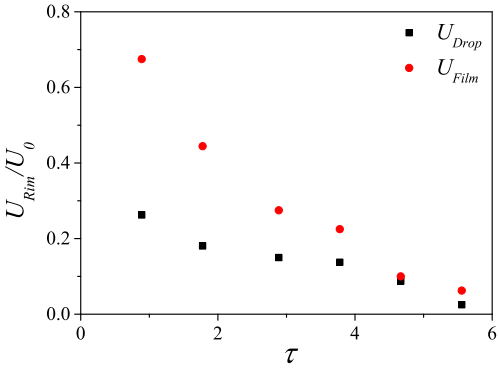

Figure 7.5: The scaled velocity of both rims of the double corona over dimensionless time $\tau = t\frac{U_0}{D_0}$ for a dyed water droplet impacting onto a S1 wall film with a relative film thickness $\delta = 0.2$.

impact diffusion processes can be observed, visualised as red stripes in the corona wall. Furthermore, this leads to the formation of secondary droplets containing a mixture of both. The central jet, resulting from partial rebound, seems to be highly concentrated by the drop liquid to the saturation of the red colour. The imaging from below allows the observation of the liquid distribution inside the wall film. It can be seen in Fig. 7.7, that the drop impact results in a sun-like shape. The drop liquids spreads much further in this case compared to Fig. 7.6. This shows the huge difference due to the miscibility and needs to be further investigated.

7.2 Evaluation of the contents of a liquid multicomponent drop

7.2.1 Description of the measurement method

No attempt has been done so far to quantitatively measure the volume ratio of liquids in the multicomponent secondary droplets. Optical methods are preferred for volume ratio measurements because of their non-intrusiveness. However, there are numerous complicating factors beyond the description of the light scattering. For instance, the addition of a fluorescent dye in the impacting drop would result

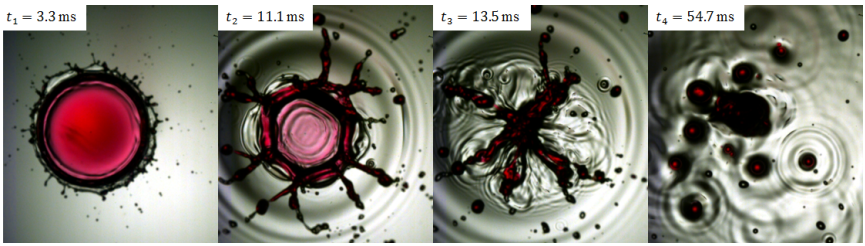

Figure 7.6: Temporal development of a double corona of a dyed water droplet impacting onto a S1 wall film with the relative film thickness $\delta = 0.2$.

in a scattering from mixture secondary drops proportional to the amount of fluorescent dye that was in the volume. However, the illumination would have to be appropriate to be sure all dye molecules were excited, the total volume of the secondary droplet would still have to be determined, and internal absorption and secondary scattering would have to be accounted for, as with other applications of laser-induced fluorescence [70]. Although solutions for the light scattering from a sphere with an eccentrically located spherical inclusion have been presented in [21, 45, 58, 67, 185, 189]. The present study introduces a single view imaging approach to make such a quantitative estimation.

In the following discussion several assumptions have been made. When considering a host droplet with an inclusion, the refractive indexes of the two liquids must be different. This difference can be achieved using a dye, as shown in Fig. 7.1. Furthermore, several images in a time sequence of the same droplet must be available, imposing demands on the frame rate of the imaging system, depending on the conditions of drop impact. A unique droplet identification must be possible from frame to frame, which is only possible if the droplets do not traverse too far in each frame. For instance, the experiments described in the present study were performed using a FASTCAM SA-X2 camera, having a frame rate of 20000 fps with a pixel resolution of 1024×672 and a shutter speed of 30 μs. An f-stop of 32 was used to insure a large depth of field.

Another assumption is that any inclusion droplet in the host droplet is well illuminated, meaning the periphery of the inclusion should be detectable by the imaging camera. This requires that the fluid of the inclusion droplet at its periphery be illuminated by the fluence field and that the scattered light also reach the detector. This is not a trivial constraint and demands experimentation with the system illumination. In the present experiments, several illumination sources were employed simultaneously, as described in Section 2.1.5.

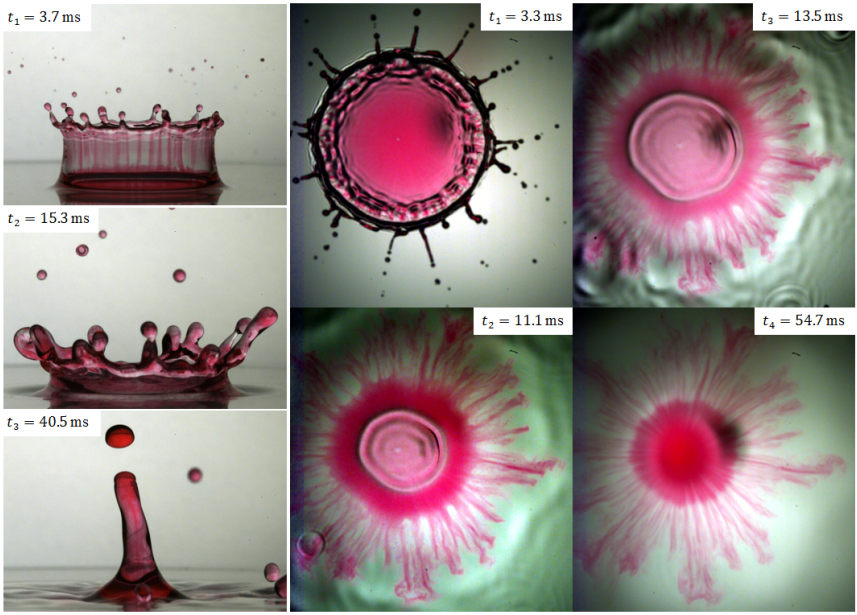

Figure 7.7: Temporal development of a double corona of a dyed water droplet impacting onto a S1 wall film with the relative film thickness $\delta = 0.2$.

The underlying principle of the method is sketched in Fig. 7.9, where three curves are shown on a graph relating volume ratio (inclusion droplet to secondary droplet) to observed projected area ratio (inclusion droplet to host droplet). The top curve serves as a reference and expresses the volume to projected area ratio of the inclusion droplet if no distortion is caused by the outer host droplet. This would occur if the refractive index of the host droplet (colored white) would have the same refractive index as the surrounding ambient (refractive index matched). The middle and bottom curves relate the actual volume ratio to the observed projected area ratio if the inclusion droplet is either on the near or far side of the host droplet from where the image is captured. The numerical values shown in this graph correspond to a relative refractive index of 1.403, i.e. silicone droplets in air. These curves were obtained by simply applying Snell's law at the ambient-droplet interface and determining the point on the host droplet circumference, where the edge ray of the inclusion drop exits the host droplet towards the camera. From this simple consideration, the middle and lower curves should represent upper and lower bounds of the projected image size, if the inclusion droplet is centered on

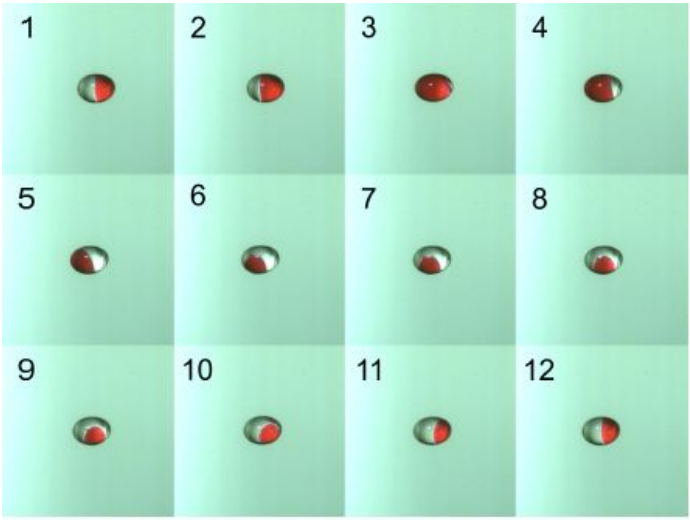

Figure 7.8: Sequence of 12 images of a levitated, red coloured water droplet embedded in a 3μl silicon oil droplet.

the observation axis. If the inclusion droplet lies eccentric from the center axis of the host droplet, then other (larger) values of area ratio are to be expected, as will be confirmed below in Section 7.2.2.

7.2.2 Calibration of the method

To test this hypothesis, a calibration has been performed by suspending drops of known mixture volume ratio in an acoustic levitator and imaging them onto a camera. Levitated drops take on an spheroidal shape, as described in detail in [198]. Furthermore, droplets in an acoustic levitator tend to rotate about a vertical axis, since residual forces arise if the droplet is not exactly centered in the respective pressure node, something which is virtually always present due to natural air currents in the laboratory.

To establish the known mixture ratio in the droplet, first a water drop colored red is injected into a pressure node using a precision injection needle of 0.4mm inner diameter and treated with a hydrophobic coating (NeverWet®). The volume can then be computed assuming symmetry about the axial axis and having calibrated the camera magnification using a target grid previous to the measurement. Silicon oil is then added to the drop, again using a precision injection needle and

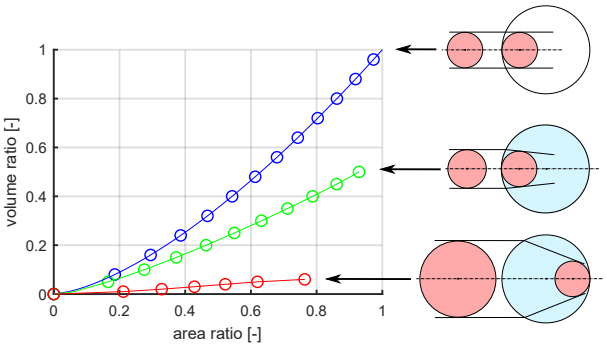

Figure 7.9: Relation between volume ratio of an inclusion droplet centered on the axis of a host droplet to the area ratio observed from a camera, also placed on the axis. Top: The host droplet has the same refractive index as the ambient; Middle: The host droplet is a liquid in air and the inclusion droplet is on the camera side of the host droplet. Bottom: The host droplet is a liquid in air and the inclusion droplet is on the far side from the camera in the host droplet. Computations have been performed for a relative refractive index of 1.33, i.e. water droplets in air.

a precision pump. The volume of silicon oil is known to be within $\pm\mu$l. The silicon oil encapsulates the colored water droplet. From the camera image of the total droplet, the volume ratio can then be compared to the project area ratio, as presented in Fig. 7.9. The calibration procedure was conducted for water drops of four different approximate diameters and for silicon oils of kinematic viscosity 5 and 20 mm^2/s and ranging from volumes between 2 and 5 μl.

A typical sequence of droplet images taken from the acoustic levitator is shown in Fig. 7.8, from which both the spheroidal shape of the droplet can be observed as well as the changing eccentricity of the inclusion droplet in the host droplet. Referring to the discussion in Section 7.2.1, the rotation of the droplet is such that the inclusion droplet is directly opposite to the camera viewing side in the main droplet in photograph 3, whereas between photographs 8 and 9 a minimum image of the inclusion droplet is observed, suggesting that the inclusion droplet is located within the host droplet on the camera viewing side.

The eccentricity of the inclusion droplet (E) is defined according to the scheme shown in Fig. 7.10. First, the center of the colored water droplet is determined, designated here as the vector **e**. This vector is then projected onto the major axis

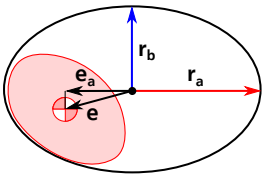

Figure 7.10: Defining parameters for the eccentricity of the inclusion droplet.

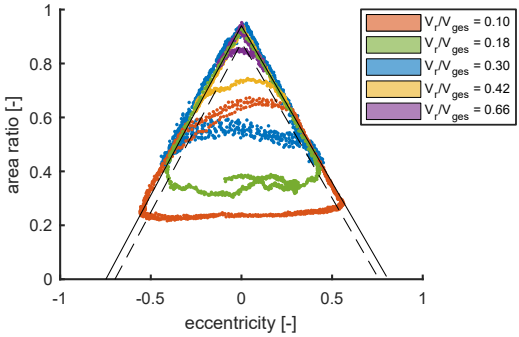

Figure 7.11: Characteristic triangle comparing area ratio with eccentricity.

of the droplet, resulting in the vector e_a. The ratio $E = \|e_a/r_a\|$ is called the eccentricity, where r_a is the major semi-axis length. If the levitated droplet is now observed over many images, the computed projected area ratio of water droplet (red) to total droplet area $\epsilon = A_{water}/A_{total}$ can be compared with the measured eccentricity, which results in characteristic triangles shown in Fig. 7.11 for five different volume ratios of secondary droplet to inclusion droplet.

The measured triangle shows remarkable consistency among different volume ratios on the two side arms and at the peak. However, the minimum level of the area ratio ϵ correlates strongly with the volume ratio. If only measured values falling within the inner dotted triangle are considered, then the probability density function of the area ratios are represented in Fig. 7.12. The most probable occurrence of these distributions, i.e. the position of the maximum peak for each volume ratio, is then taken as a representative area ratio and compared with the postulated ratios presented in Fig. 7.9. This has been done in Fig. 7.13, where a large number of different volume ratios have been compared to the middle curve of Fig. 7.9. An empirical calibration curve is fitted and shown as a solid line. This

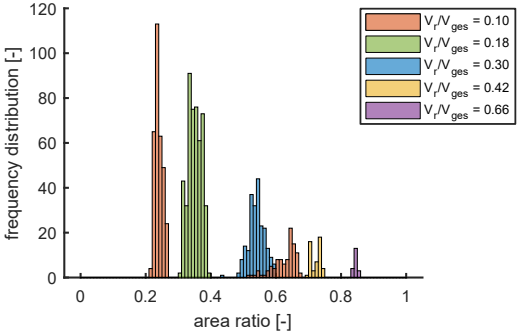

Figure 7.12: Probability density function of area ratio measured in dotted region shown in Fig. 7.11.

curve is numerically described by

$$\frac{V_{incl}}{V_{total}} = 0.59\,\epsilon^{1.19}. \tag{7.1}$$

The simple phenomenological explanation in Section 7.2.1 agrees very well with the measured values. This indicates that the images, which represent the lower line on the eccentricity triangle plot, correspond to the minimum image size of the inclusion droplet. At larger values of area ratio ϵ larger deviations from this correlation are observed. This corresponds to the condition that the inclusion drop is not completely illuminated and the projected area cannot properly estimated from the images. For future studies the illumination has to be improved.

7.2.3 Number and content of the secondary drops

The influence of the relative film thickness on the total number of secondary droplets is shown in Fig. 7.14 (a). Since the splashing threshold is not significantly affected by the relative film thickness in these experiments in general, the total number of secondary droplets decreases slightly with decreasing relative film thickness. Starting from $\kappa = 1$ the total number of secondary droplets decreases with increasing κ. This agrees with the decreasing instability of the rim for increasing wall film viscosity.

The ratio of the secondary droplets containing the wall-film liquid or a mixture of both liquids is dependent on the viscosity ratio κ, as shown in Fig. 7.14 (b). If the wall film is less viscous, the instability in the wall film liquid is higher

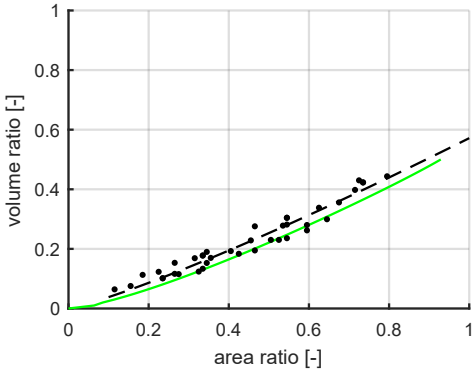

Figure 7.13: Calibration curve for volume ratio as a function of minimum area ratio. Dots represent measurements from the acoustic levitator and the dashed black line corresponds to Eq. (7.1). The green line is taken directly from Fig. 7.9

compared to the liquid of the drop and therefore the wall film liquid starts to form finger-like jets which finally lead to the generation of secondary droplets. With increasing viscosity of the wall film the rim is still governed by the liquid of the wall film but the finger-like jets contain more and more of both liquids, more or less simultaneously. Consequently, the ratio of the mixed secondary droplets increases until finally only mixed secondary droplets are generated. This observation can be explained by the double corona. For bigger corona height differences the corona of the wall film leads to the formation of secondary droplets and therefore, most secondary droplets contain only the wall film liquid. With increasing wall film viscosity, this corona height difference decreases, which leads to more mixed secondary droplets. However, more experiments are needed including also varying the drop liquid in order to confirm this hypothesis. Furthermore, this method has to be extended for miscible liquids.

In Fig. 7.15 two distributions of the area ratio of both liquids are shown exemplary. Since the impact parameters are comparable and only the film viscosity is changed, the effect of the film viscosity on the total number of secondary droplets on the hand and on the content distribution on the other hand is clearly visible.

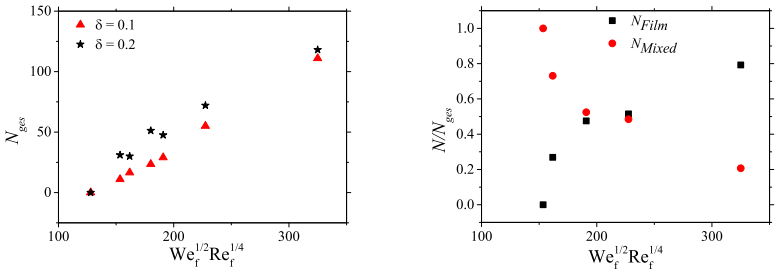

(a) (b)

Figure 7.14: Total number of secondary droplets as a function of $We_f^{1/2} Re_f^{1/4}$ for immiscible liquids for the relative film thicknesses $\delta = 0.1$ and $\delta = 0.2$ (a)) and the ratio of secondary droplets containing wall film liquid and respectively a mixture of both liquids as a function (b)) as a function of Weber and Reynolds number.

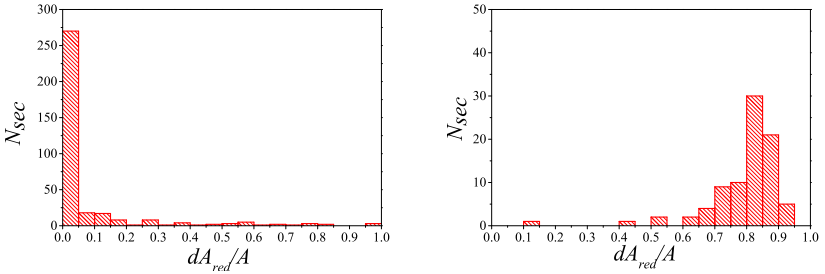

(a) (b)

Figure 7.15: Distribution of the area ratio of detected red pixel which are related to the liquid of the drop inside of the produced secondary droplets resulting from a FuW drop impacting onto (a)) a S1 and (b)) a S50 wall film for $\delta = 0.2$ and $U_0 = 3.3$ m/s.

7.3 Conclusions

In order to visualise the distribution of both immiscible liquids during and after the impact, the liquid of the drop is dyed. The content of multicomponent secondary droplets is dependent on the liquid combination. For $\kappa \ll 1$ the secondary droplets consist only of the liquid of the wall film while with increasing κ the distribution changes until all secondary droplets consist of a mixture of both liquids. In the case of a higher relative film thickness the *double corona* can be observed. While the surface tension difference of the drop and wall film liquid lead to the formation of the double corona, the viscosity of the wall film determines its hight difference. With increasing κ the height difference of both coronas decreases until both corona heights are comparable. The effect of miscibility is obvious in the drop liquid distribution in the wall film for miscible and immiscible liquids. For immiscible liquids the drop liquid forms droplets floating on the wall film, the drop liquid forms a sun-like shape in the wall film for miscible liquids. A calibration method is introduced to determine the area ratio of a known droplet-in-droplet configuration using an acoustic levitator. These calibration data are used to analyse the multicomponent secondary droplets in the experiments. It is shown that the content of the secondary droplets is dependent on the wall film viscosity.

8 Conclusions and outlook

In the present study the drop impact onto wetted and soft substrates is investigated for various impact conditions and fluid combinations. These phenomena have been investigated intensively over the last 150 years. Nevertheless, if the liquids of drop and wall film are different, the physics of the interaction of both liquids during the impact is much more complicated.

The main objectives of the present study are to gain a better understanding of drop impacts onto a wall wetted by another liquid, of the interaction of both liquids during the impact process and of the kinematics of drop spreading and corona stability. For many industrial applications the description of the splashing threshold and the content of multicomponent secondary droplets are mainly required. To better predict these quantities the hydrodynamics of impact, kinematics of spreading and corona stability have to be accurately investigated.

To achieve these aims, experimental setups have been designed for the observation of different outcomes of drop impact onto a normal substrate as well as onto an inclined wall film.

Different outcomes resulting from drop impact are identified and classified: deposition, corona, splashing and partial rebound. The different outcomes are hereby influenced by the impact parameter such as initial drop diameter and impact velocity, but also by the fluid properties of both liquids such as kinematic viscosity and surface tension. The effect of these influencing parameters on the impact outcomes are determined. Drop spreading is observed for drop impact onto high viscous and soft substrates. The maximum spreading diameter is analysed, which is mainly dependent on the Reynolds number. The expansion of a corona is observed for less viscous wall films. In this case the maximum corona diameter is investigated and determined for several impact conditions and fluid combinations. It is shown that the Weber number cannot be used to describe the dynamics of the corona propagation in the viscous regime. The maximum corona diameter can be described by the Reynolds number though.

For drop impact onto an inclined flowing wall film the impact leads to the expansion of a non-axisymmetric corona. The geometry of this non-axisymmetric corona is analysed and theoretically described. For different urea-water solutions as drop and wall film liquid the formation of holes is observed. Concentration differences in the corona wall seem to induce Marangoni-driven flows, which finally

lead to the formation of holes in the corona wall. The time of the first hole appearance is linearly dependent on the concentration difference of the wall film and drop liquid. Further investigations including variation of the fluid temperature are necessary to verify this assumption.

The formation of secondary droplets as result from drop splashing is investigated and the influencing parameters are identified. Since both fluid properties influence the splashing threshold, a new scaling is introduced and described considering both fluid properties. It is shown that the well-known K number only determines the splashing threshold of the viscosity of the film is much larger or much smaller than the drop viscosity. For comparable viscosities of drop and wall film, a critical modified K number is introduced as a function of the viscosity ratio. Finally, the modified K number is used to predict splashing for typical engine conditions, since splashing is considered as one effect triggering pre-ignition in the engine.

For certain conditions, a further fascinating phenomenon is observed: corona detachment. The corona detaches from the base of the corona and leads to a secondary atomisation. The narrow range of parameters, in which corona detachment can be observed, is investigated and determined.

For many technical applications such as the internal combustion engine, the knowledge of the content of secondary droplets is very important. The content of these multicomponent droplets can significantly influence the efficiency of technical processes, like combustion. In this study a method is developed to determine the content of multicomponent corona and secondary droplets. By adding dye to the liquid of the drop and using a colour high-speed imaging system, both liquids can be distinguished. Dependent on the wall film viscosity and film thickness, the evolution of a double corona is observed. In this case two coronas with different length and time scales occur for immiscible liquids. The corona of the wall film liquid rises higher than the corona of the drop liquid, since the surface tension of the wall film is much smaller in these experiments. The height difference of both coronas depends mainly on the viscosity of the wall film. This leads to the content distribution of the secondary droplets, since a higher height difference result in a higher amount of secondary droplets only consisting of the wall film liquid. Next, calibration measurements have been conducted to determine the area ratio of a known droplet-in-droplet configuration using an acoustic levitator. These calibration data are used to analyse the multicomponent secondary droplets in the experiments. It is shown that the content of the secondary droplets is dependent on the wall film viscosity. It is demonstrated, that this method can be used for future investigations of parametric studies determining the content of multicomponent secondary droplets in case of immiscible liquids. This method has to be

further extended considering also miscible liquids. For the characterisation of the very fine secondary spray different measurement techniques such as the time shift technique can be used, since high-speed imaging is limited in the spatial resolution.

Bibliography

[1] G. Ahmed, V. V. Kalinin, O. Arjmandi-Tash, and V. M. Starov. Equilibrium of droplets on a deformable substrate: Influence of disjoining pressure. *Colloids and Surfaces A: Physicochemical and Engineering Aspects*, 521:3–12, 2017.

[2] E. Alam, S. Yadav, J. J. Schneider, and T. Gambaryan-Roisman. Imbibition of water into substrates prepared by thermal treatment of polydimethylsiloxane layers. *Colloids and Surfaces A: Physicochemical and Engineering Aspects*, 521:69–77, 2017.

[3] S. K. Alghoul, C. N. Eastwick, and D. B. Hann. Normal droplet impact on horizontal moving films: an investigation of impact behaviour and regimes. *Experiments in Fluids*, 50(5):1305–1316, 2011.

[4] A. Alizadeh, V. Bahadur, W. Shang, Y. Zhu, D. Buckley, A. Dhinojwala, and M. Sohal. Influence of substrate elasticity on droplet impact dynamics. *Langmuir*, 29(14):4520–4524, 2013.

[5] A. Alizadeh, M. Yamada, R. Li, W. Shang, S. Otta, S. Zhong, L. Ge, A. Dhinojwala, K. R. Conway, V. Bahadur, et al. Dynamics of ice nucleation on water repellent surfaces. *Langmuir*, 28(6):3180–3186, 2012.

[6] A. B. Aljedaani, C. Wang, A. Jetly, and S. T. Thoroddsen. Experiments on the breakup of drop-impact crowns by marangoni holes. *Journal of Fluid Mechanics*, 844:162–186, 2018.

[7] L. Andreassi, S. Ubertini, and L. Allocca. Experimental and numerical analysis of high pressure diesel spray–wall interaction. *International Journal of Multiphase Flow*, 33(7):742–765, 2007.

[8] O. Arjmandi-Tash, N. M. Kovalchuk, A. Trybala, I. V. Kuchin, and V. Starov. Kinetics of wetting and spreading of droplets over various substrates. *Langmuir*, 33(18):4367–4385, 2017.

[9] V. Bahadur, L. Mishchenko, B. Hatton, J. A. Taylor, J. Aizenberg, and T. Krupenkin. Predictive model for ice formation on superhydrophobic surfaces. *Langmuir*, 27(23):14143–14150, 2011.

[10] S. Bakshi, I. V. Roisman, and C. Tropea. Investigations on the impact of a drop onto a small spherical target. *Physics of Fluids*, 19(3):032102, 2007.

[11] D. Banks, C. Ajawara, R. Sanchez, H. Surti, and G. Aguilar. Effects of drop and film viscosity on drop impacts onto thin films. *Atomization and Sprays*, 23(6), 2013.

[12] Bartels Mikrotechnik. Operating manual for micropump mp6/mp6-air/mp6-pp and controller.

[13] E. Berberović, N. P. van Hinsberg, S. Jakirlić, I. V. Roisman, and C. Tropea. Drop impact onto a liquid layer of finite thickness: Dynamics of the cavity evolution. *Physical Review E*, 79(3):036306, 2009.

[14] R. Bernard, P. Foltyn, A. Geppert, G. Lamanna, and B. Weigand. Generalized analysis of the deposition/splashing limit for one-and two-component droplet impacts upon thin films. In *Ilass Europe. 28th european conference on Liquid Atomization and Spray Systems*, pages 730–737. Editorial Universitat Politècnica de València, 2017.

[15] V. Bertola and M. Wang. Dynamic contact angle of dilute polymer solution drops impacting on a hydrophobic surface. *Colloids and Surfaces A: Physicochemical and Engineering Aspects*, 481:600–608, 2015.

[16] J. C. Bird, S. S. Tsai, and H. A. Stone. Inclined to splash: triggering and inhibiting a splash with tangential velocity. *New Journal of Physics*, 11(6):063017, 2009.

[17] A. Bisighini, G. E. Cossali, C. Tropea, and I. V. Roisman. Crater evolution after the impact of a drop onto a semi-infinite liquid target. *Physical Review E*, 82(3):036319, 2010.

[18] K. Black and V. Bertola. Non-newtonian leidenfrost drops. *Atomization and Sprays*, 23(3), 2013.

[19] B. Blais, J.-P. Braeunig, D. Chauveheid, J.-M. Ghidaglia, and R. Loubère. Dealing with more than two materials in the fvcf–enip method. *European Journal of Mechanics-B/Fluids*, 42:1–9, 2013.

[20] D. Bolleddula, A. Berchielli, and A. Aliseda. Impact of a heterogeneous liquid droplet on a dry surface: Application to the pharmaceutical industry. *Adv. Colloid Interface Sci.*, 159(2):144–159, 2010.

[21] F. Borghese, P. Denti, R. Saija, and O. Sindoni. Optical properties of spheres containing a spherical eccentric inclusion. *JOSA A*, 9(8):1327–1335, 1992.

[22] F. Boyer, E. Sandoval-Nava, J. H. Snoeijer, J. F. Dijksman, and D. Lohse. Drop impact of shear thickening liquids. *Physical Review Fluids*, 1(1):013901, 2016.

[23] J. Breitenbach. *Drop and spray impact onto a hot substrate: Dynamics and heat transfer*. PhD thesis, Technische Universität, 2018.

[24] BROOKFIELD. DV-III ULTRA Operating instructions.

[25] Bruenig. Farbsegmentierung. https://me.efi.th-nuernberg.de/interaktion/index.php5/, 11 2014.

[26] S. Brulin. Einfluss der Temperatur auf den Tropfenaufprall auf einen Flüssigkeitsfilm. Master thesis, Technische Universität, Darmstadt, 2016.

[27] H.-J. Butt, I. V. Roisman, M. Brinkmann, P. Papadopoulos, D. Vollmer, and C. Semprebon. Characterization of super liquid-repellent surfaces. *Current Opinion in Colloid & Interface Science*, 19(4):343 – 354, 2014.

[28] L. Cao, A. K. Jones, V. K. Sikka, J. Wu, and D. Gao. Anti-icing superhydrophobic coatings. *Langmuir*, 25(21):12444–12448, 2009.

[29] J. R. Castrejón-Pita, R. Castrejón-García, and I. M. Hutchings. High speed shadowgraphy for the study of liquid drops. In *Fluid Dynamics in Physics, Engineering and Environmental Applications*, pages 121–137. Springer, 2013.

[30] S. Chandra and C. Avedisian. On the collision of a droplet with a solid surface. *Proceedings of the Royal Society of London. Series A: Mathematical and Physical Sciences*, 432(1884):13–41, 1991.

[31] Z. Che, A. Deygas, and O. K. Matar. Impact of droplets on inclined flowing liquid films. *Physical Review E*, 92(2):023032, 2015.

[32] Z. Che and O. K. Matar. Impact of droplets on liquid films in the presence of surfactant. *Langmuir*, 33(43):12140–12148, 2017.

[33] L. Chen, E. Bonaccurso, P. Deng, and H. Zhang. Droplet impact on soft viscoelastic surfaces. *Physical Review E*, 94(6):063117, 2016.

[34] L. Chen, E. Bonaccurso, and M. E. Shanahan. Inertial to viscoelastic transition in early drop spreading on soft surfaces. *Langmuir*, 29(6):1893–1898, 2013.

[35] N. Chen, H. Chen, and A. Amirfazli. Drop impact onto a thin film: Miscibility effect. *Physics of Fluids*, 29(9):092106, 2017.

[36] L. Cheng. Dynamic spreading of drops impacting onto a solid surface. *Industrial & Engineering Chemistry Process Design and Development*, 16(2):192–197, 1977.

[37] M. Cheng and J. Lou. A numerical study on splash of oblique drop impact on wet walls. *Computers & Fluids*, 115:11–24, 2015.

[38] S.-L. Chiu and T.-H. Lin. Experiment on the dynamics of a compound drop impinging on a hot surface. *Physics of Fluids*, 17(12):122103, 2005.

[39] C. Clanet, C. Béguin, D. Richard, and D. Quéré. Maximal deformation of an impacting drop. *Journal of Fluid Mechanics*, 517:199–208, 2004.

[40] E. Collings, A. Markworth, J. McCoy, and J. Saunders. Splat-quench solidification of freely falling liquid-metal drops by impact on a planar substrate. *Journal of Materials Science*, 25(8):3677–3682, 1990.

[41] G. Cossali, G. Brunello, A. Coghe, and M. Marengo. Impact of a single drop on a liquid film: experimental analysis and comparison with empirical models. In *Italian Congress of Thermofluid Dynamics UIT, Ferrara*, volume 30, 1999.

[42] G. Cossali, A. Coghe, and M. Marengo. The impact of a single drop on a wetted solid surface. *Experiments in Fluids*, 22(6):463–472, 1997.

[43] L. Courbin, J. C. Bird, and H. A. Stone. Splash and anti-splash: observation and design. *Chaos: An Interdisciplinary Journal of Nonlinear Science*, 16(4):041102, 2006.

[44] M. Coux, C. Clanet, and D. Quéré. Soft, elastic, water-repellent materials. *Applied Physics Letters*, 110(25):251605, 2017.

[45] Z. Cui and Y. Han. A review of the numerical investigation on the scattering of gaussian beam by complex particles. *Physics Reports*, 538(2):39–75, 2014.

[46] E. L. Cussler. *Diffusion: mass transfer in fluid systems*. Cambridge University Press, 2009.

[47] Dataphysics. OCA Produktserie.

[48] P. Day, A. Manz, and Y. Zhang. *Microdroplet technology: principles and emerging applications in biology and chemistry*. Springer Science & Business Media, 2012.

[49] P.-G. De Gennes, F. Brochard-Wyart, and D. Quéré. *Capillarity and wetting phenomena: drops, bubbles, pearls, waves*. Springer Science & Business Media, 2013.

[50] B. Derby. Inkjet printing of functional and structural materials: fluid property requirements, feature stability, and resolution. *Ann. Rev. Mater. Res.*, 40:395–414, 2010.

[51] B. Derby and N. Reis. Inkjet printing of highly loaded particulate suspensions. *MRS Bull.*, 28(11):815–818, 2003.

[52] S. F. Dingle. *Lubricant induced pre-ignition in an optical spark-ignition engine*. PhD thesis, Brunel University London, 2014.

[53] O. G. Engel. Crater depth in fluid impacts. *Journal of Applied Physics*, 37(4):1798–1808, 1966.

[54] P. Favaro and S. Soatto. *3-d shape estimation and image restoration: Exploiting defocus and motion-blur*. Springer Science & Business Media, 2007.

[55] A. I. Fedorchenko and A.-B. Wang. On some common features of drop impact on liquid surfaces. *Physics of Fluids*, 16(5):1349–1365, 2004.

[56] T. Fujimatsu, H. Fujita, M. Hirota, and O. Okada. Interfacial deformation between an impacting water drop and a silicone-oil surface. *Journal of Colloid and Interface Science*, 264(1):212–220, 2003.

[57] J. Fukai, Y. Shiiba, T. Yamamoto, O. Miyatake, D. Poulikakos, C. M. Megaridis, and Z. Zhao. Wetting effects on the spreading of a liquid droplet colliding with a flat surface: Experiment and modeling. *Physics of Fluids*, 7(2):236–247, 1995.

[58] K. A. Fuller. Scattering and absorption cross sections of compounded spheres. iii. spheres containing arbitrarily located spherical inhomogeneities. *JOSA A*, 12(5):893–904, 1995.

[59] A. K. Gaharwar, R. K. Avery, A. Assmann, A. Paul, G. H. McKinley, A. Khademhosseini, and B. D. Olsen. Shear-thinning nanocomposite hydrogels for the treatment of hemorrhage. *ACS Nano*, 8(10):9833–9842, 2014.

[60] X. Gao, L. Kong, R. Li, and J. Han. Heat transfer of single drop impact on a film flow cooling a hot surface. *International Journal of Heat and Mass Transfer*, 108:1068–1077, 2017.

[61] A. Geppert, D. Chatzianagnostou, C. Meister, H. Gomaa, G. Lamanna, and B. Weigand. Classification of impact morphology and splashing/deposition limit for n-hexadecane. *Atomization and Sprays*, 26(10), 2016.

[62] A. Geppert, F. Greif, G. Lamanna, and B. Weigand. Phenomenology of two-component droplet-wall film-interaction. In *Proceedings of the 25th European Conference on Liquid Atomization and Spray Systems, ILASS-Europe*, 2013.

[63] A. Geppert, A. Terzis, G. Lamanna, M. Marengo, and B. Weigand. Two component droplet wall-film interactions: impact dynamics on very thin films. In *Proc. ILASS-Europe 2016*, Brighton, UK, September 2016.

[64] A. Geppert, A. Terzis, G. Lamanna, M. Marengo, and B. Weigand. A benchmark study for the crown-type splashing dynamics of one-and two-component droplet wall–film interactions. *Experiments in Fluids*, 58(12):172, 2017.

[65] F. Gibbs, S. Kermasha, I. Alli, and C. N. M. Bernard. Encapsulation in the food industry: a review. *International Journal of Food Sciences and Nutrition*, 50(3):213–224, 1999.

[66] M. Gohl, S. Brandt, M. Wittler, M. Budde, G. Knoll, S. Krause, S. Pischinger, C. Stein, P. Adomeit, G. Matz, et al. Influence of the mixture formation on the lubrication oil emission of combustion engines. *SAE International Journal of Fuels and Lubricants*, 3(1):733–744, 2010.

[67] G. Gouesbet and G. Gréhan. Generalized lorenz-mie theory for a sphere with an eccentrically located spherical inclusion. *Journal of Modern Optics*, 47(5):821–837, 2000.

[68] S. Gouin. Microencapsulation: industrial appraisal of existing technologies and trends. *Trends in Food Science & Technology*, 15(7-8):330–347, 2004.

[69] P. Gregory, E. Guthrie, and M. E. Bunce. Experiments on splash dispersal of fungus spores. *Microbiology*, 20(2):328–354, 1959.

[70] D. Greszik, H. Yang, T. Dreier, and C. Schulz. Measurement of water film thickness by laser-induced fluorescence and raman imaging. *Applied Physics B*, 102(1):123–132, 2011.

[71] Y. Guo and Y. Lian. High-speed oblique drop impact on thin liquid films. *Physics of Fluids*, 29(8):082108, 2017.

[72] L. Han, T. Zhu, H. Qiao, D. Zhang, D. Fu, and J. Zhang. Investigation of low-speed pre-ignition in boosted spark ignition engine. Technical report, SAE Technical Paper, 2015.

[73] C. Hao, Y. Zhou, X. Zhou, L. Che, B. Chu, and Z. Wang. Dynamic control of droplet jumping by tailoring nanoparticle concentrations. *Applied Physics Letters*, 109(2):021601, 2016.

[74] F. H. Harlow and J. P. Shannon. The splash of a liquid drop. *J. Appl. Phys.*, 38(10):3855–3866, 1967.

[75] E. Hecht. *Optik*. Walter de Gruyter GmbH & Co KG, 2018.

[76] P. Hobbs and T. Osheroff. Splashing of drops on shallow liquids. *Science*, 158(3805):1184–1186, 1967.

[77] C. J. Howland, A. Antkowiak, J. R. Castrejón-Pita, S. D. Howison, J. M. Oliver, R. W. Style, and A. A. Castrejón-Pita. ItâĂŹs harder to splash on soft solids. *Physical Review Letters*, 117(18):184502, 2016.

[78] H. K. Huh, S. Jung, K. W. Seo, and S. J. Lee. Role of polymer concentration and molecular weight on the rebounding behaviors of polymer solution droplet impacting on hydrophobic surfaces. *Microfluidics and Nanofluidics*, 18(5-6):1221–1232, 2015.

[79] T. Inoue, Y. Inoue, and M. Ishikawa. Abnormal combustion in a highly boosted si engine-the occurrence of super knock. Technical report, SAE Technical Paper, 2012.

[80] B. Jaehne. *Quantitative Visualization*, pages 157–187. Springer Berlin Heidelberg, 2005.

[81] C. Josserand and S. T. Thoroddsen. Drop impact on a solid surface. *Annu. Rev. Fluid Mech.*, 48:365–391, 2016.

[82] S. Jung, M. Dorrestijn, D. Raps, A. Das, C. M. Megaridis, and D. Poulikakos. Are superhydrophobic surfaces best for icephobicity? *Langmuir*, 27(6):3059–3066, 2011.

[83] M. Kadoura and S. Chandra. Rupture of thin liquid films sprayed on solid surfaces. *Experiments in Fluids*, 54(2):1–11, 2013.

[84] M. Kassai, H. Hashimoto, T. Shiraishi, A. Teraji, and T. Noda. Mechanism analysis on lspi occurrence in boosted si engines. Technical report, SAE Technical Paper, 2015.

[85] M. Kassai, K. Torii, T. Shiraishi, T. Noda, T. K. Goh, K. Wilbrand, S. Wakefield, A. Healy, D. Doyle, R. Cracknell, et al. Research on the effect of lubricant oil and fuel properties on lspi occurrence in boosted si engines. Technical report, SAE Technical Paper, 2016.

[86] A. Khoufech, M. Benali, and K. Saleh. Influence of liquid formulation and impact conditions on the coating of hydrophobic surfaces. *Powder Technology*, 270:599–611, 2015.

[87] J. Kim. Spray cooling heat transfer: the state of the art. *International Journal of Heat and Fluid Flow*, 28(4):753–767, 2007.

[88] H. Kittel, I. Roisman, and C. Tropea. Drops make a splash. In *Selected Papers from the 31st International Congress on High-Speed Imaging and Photonics*, volume 10328, page 103281B. International Society for Optics and Photonics, 2017.

[89] H. Kittel, I. Roisman, and C. Tropea. Splashing of a very viscous liquid drop impacting onto a solid wall wetted by another liquid. In *ILASS Europe. 28th European Conference on Liquid Atomization and Spray Systems*, pages 716–722. Editorial Universitat Politècnica de València, 2017.

[90] H. M. Kittel, E. Alam, I. V. Roisman, C. Tropea, and T. Gambaryan-Roisman. Splashing of a newtonian drop impacted onto a solid substrate coated by a thin soft layer. *Colloids and Surfaces A: Physicochemical and Engineering Aspects*, 553:89–96, 2018.

[91] H. M. Kittel, I. V. Roisman, and C. Tropea. Content of secondary droplets formed by drop impact onto a solid wall wetted by another liquid. In *14th Triennial International Conference on Liquid Atomization and Spray Systems*, 2018.

[92] H. M. Kittel, I. V. Roisman, and C. Tropea. Splash of a drop impacting onto a solid substrate wetted by a thin film of another liquid. *Physical Review Fluids*, 3:073601, Jul 2018.

[93] M. Krystek. *Berechnung der Messunsicherheit: Grundlagen und Anleitung für die praktische Anwendung*. Beuth Verlag, 2015.

[94] H. Kubach, A. Weidenlener, J. Pfeil, T. Koch, H. Kittel, I. V. Roisman, and C. Tropea. Investigations on the influence of fuel oil film interaction on pre-ignition events in highly boosted di gasoline engines. Technical report, SAE Technical Paper, 2018.

[95] S. Kulinich, S. Farhadi, K. Nose, and X. Du. Superhydrophobic surfaces: are they really ice-repellent? *Langmuir*, 27(1):25–29, 2010.

[96] N. Laan, K. G. de Bruin, D. Bartolo, C. Josserand, and D. Bonn. Maximum diameter of impacting liquid droplets. *Physical Review Applied*, 2(4):044018, 2014.

[97] G. Lagubeau, M. A. Fontelos, C. Josserand, A. Maurel, V. Pagneux, and P. Petitjeans. Spreading dynamics of drop impacts. *Journal of Fluid Mechanics*, 713:50–60, 2012.

[98] A. Latka, A. Strandburg-Peshkin, M. M. Driscoll, C. S. Stevens, and S. R. Nagel. Creation of prompt and thin-sheet splashing by varying surface roughness or increasing air pressure. *Physical Review Letters*, 109(5):054501, 2012.

[99] T. Lauer and M. Heiß. Analysis of particle separation with respect to preignition in an si-engine. In *6th European Conference on Computational Fluid Dynamics (ECFD VI)*, 2014.

[100] T. Lauer, M. Heiss, N. Bobicic, and S. Pritze. Model approach for preignition mechanisms. *MTZ Worldwide*, 75(1):44–49, 2014.

[101] M. Layani, R. Berman, and S. Magdassi. Printing holes by a dewetting solution enables formation of a transparent conductive film. *ACS Appl. Mater. Interfaces*, 6(21):18668–18672, 2014.

[102] J. B. Lee, S. dos Santos, and C. Antonini. Water touch-and-bounce from a soft viscoelastic substrate: wetting, dewetting, and rebound on bitumen. *Langmuir*, 32(32):8245–8254, 2016.

[103] W.-K. Lee, W.-B. Jung, S. R. Nagel, and T. W. Odom. Stretchable superhydrophobicity from monolithic, three-dimensional hierarchical wrinkles. *Nano Letters*, 16(6):3774–3779, 2016.

[104] A. H. Lefebvre and V. G. McDonell. *Atomization and Sprays*. CRC Press, 2017.

[105] A. N. Lembach, H.-B. Tan, I. V. Roisman, T. Gambaryan-Roisman, Y. Zhang, C. Tropea, and A. L. Yarin. Drop impact, spreading, splashing, and penetration into electrospun nanofiber mats. *Langmuir*, 26(12):9516–9523, 2010.

[106] G. Leneweit, R. Koehler, K. Roesner, and G. Schäfer. Regimes of drop morphology in oblique impact on deep fluids. *Journal of Fluid Mechanics*, 543:303–331, 2005.

[107] Z. Levin and P. V. Hobbs. Splashing of water drops on solid and wetted surfaces: hydrodynamics and charge separation. *Phil. Trans. R. Soc. Lond. A*, 269(1200):555–585, 1971.

[108] H. Lhuissier, C. Sun, A. Prosperetti, and D. Lohse. Drop fragmentation at impact onto a bath of an immiscible liquid. *Physical Review Letters*, 110(26):264503, 2013.

[109] G. Liang, Y. Guo, Y. Yang, N. Zhen, and S. Shen. Spreading and splashing during a single drop impact on an inclined wetted surface. *Acta Mechanica*, 224(12):2993–3004, 2013.

[110] G. Liang, X. Mu, Y. Guo, and S. Shen. Flow and heat transfer during a single drop impact on a liquid film. *Numerical Heat Transfer, Part B: Fundamentals*, 69(6):575–582, 2016.

[111] G. Liang and I. Mudawar. Review of mass and momentum interactions during drop impact on a liquid film. *International Journal of Heat and Mass Transfer*, 101:577–599, 2016.

[112] L. A. Lubbers, J. H. Weijs, L. Botto, S. Das, B. Andreotti, and J. H. Snoeijer. Drops on soft solids: free energy and double transition of contact angles. *Journal of Fluid Mechanics*, 747, 2014.

[113] X. Luo, H. Teng, T. Hu, R. Miao, and L. Cao. An experimental investigation on low speed pre-ignition in a highly boosted gasoline direct injection engine. *SAE International Journal of Engines*, 8(2):520–528, 2015.

[114] W. Macklin. Wc macklin and pv hobbs, science 166, 107 (1969). *Science*, 166:107, 1969.

[115] W. Macklin and G. Metaxas. Splashing of drops on liquid layers. *J. Appl. Phys.*, 47(9):3963–3970, 1976.

[116] M. Magar, U. Spicher, S. Palaveev, M. Gohl, G. Müller, C. Lensch-Franzen, and J. Hadler. Experimental studies on the occurrence of low-speed pre-ignition in turbocharged gdi engines. *SAE International Journal of Engines*, 8(2):495–504, 2015.

[117] M. Marengo, C. Antonini, I. V. Roisman, and C. Tropea. Drop collisions with simple and complex surfaces. *Current Opinion in Colloid & Interface Science*, 16(4):292–302, 2011.

[118] H. Marmanis and S. Thoroddsen. Scaling of the fingering pattern of an impacting drop. *Physics of Fluids*, 8(6):1344–1346, 1996.

[119] J. Marston and S. Thoroddsen. Apex jets from impacting drops. *Journal of Fluid Mechanics*, 614:293–302, 2008.

[120] M. Mayer, P. Hofmann, B. Geringer, J. Williams, and J. Moss. Influence of different fuel properties and gasoline-ethanol blends on low-speed pre-ignition in turbocharged direct injection spark ignition engines. *SAE International Journal of Engines*, 9(2):841–848, 2016.

[121] G. H. McKinley and M. Renardy. Wolfgang von ohnesorge. *Physics of Fluids*, 23(12):127101, 2011.

[122] A. J. Meuler, G. H. McKinley, and R. E. Cohen. Exploiting topographical texture to impart icephobicity. *ACS Nano*, 4(12):7048–7052, 2010.

[123] L. Mishchenko, B. Hatton, V. Bahadur, J. A. Taylor, T. Krupenkin, and J. Aizenberg. Design of ice-free nanostructured surfaces based on repulsion of impacting water droplets. *ACS Nano*, 4(12):7699–7707, 2010.

[124] A. S. Moita and A. L. N. Moreira. Scaling the effects of surface topography in the secondary atomization resulting from droplet/wall interactions. *Experiments in Fluids*, 52(3):679–695, 2012.

[125] A. Moreira, A. Moita, and M. Panao. Advances and challenges in explaining fuel spray impingement: How much of single droplet impact research is useful? *Progress in Energy and Combustion Science*, 36(5):554–580, 2010.

[126] Y. Moriyoshi, T. Yamada, D. Tsunoda, M. Xie, T. Kuboyama, and K. Morikawa. Numerical simulation to understand the cause and sequence of lspi phenomena and suggestion of cao mechanism in highly boosted si combustion in low speed range. Technical report, SAE Technical Paper, 2015.

[127] C. Motzkus, F. Gensdarmes, and E. GÃľhin. Study of the coalescence/splash threshold of droplet impact on liquid films and its relevance in assessing airborne particle release. *Journal of Colloid and Interface Science*, 362(2):540 – 552, 2011.

[128] C. Mundo, M. Sommerfeld, and C. Tropea. Droplet-wall collisions: experimental studies of the deformation and breakup process. *International Journal of Multiphase Flow*, 21(2):151–173, 1995.

[129] D. W. Murphy, C. Li, V. dâĂŹAlbignac, D. Morra, and J. Katz. Splash behaviour and oily marine aerosol production by raindrops impacting oil slicks. *Journal of Fluid Mechanics*, 780:536–577, 2015.

[130] M. Ohtomo, H. Miyagawa, M. Koike, N. Yokoo, and K. Nakata. Preignition of gasoline-air mixture triggered by a lubricant oil droplet. *SAE International Journal of Fuels and Lubricants*, 7(3):673–682, 2014.

[131] T. Okawa, T. Shiraishi, and T. Mori. Effect of impingement angle on the outcome of single water drop impact onto a plane water surface. *Experiments in Fluids*, 44(2):331–339, 2008.

[132] J. Palacios, J. Hernández, P. Gómez, C. Zanzi, and J. López. Experimental study of splashing patterns and the splashing/deposition threshold in drop impacts onto dry smooth solid surfaces. *Experimental Thermal and Fluid Science*, 44:571–582, 2013.

[133] K.-L. Pan, K.-R. Cheng, P.-C. Chou, and C.-H. Wang. Collision dynamics of high-speed droplets upon layers of variable thickness. *Experiments in Fluids*, 45(3):435–446, 2008.

[134] K.-L. Pan and C. K. Law. Dynamics of droplet–film collision. *Journal of Fluid Mechanics*, 587:1–22, 2007.

[135] K.-L. Pan, K.-C. Tseng, and C.-H. Wang. Breakup of a droplet at high velocity impacting a solid surface. *Experiments in Fluids*, 48(1):143–156, 2010.

[136] M. Pasandideh-Fard, V. Pershin, S. Chandra, and J. Mostaghimi. Splat shapes in a thermal spray coating process: simulations and experiments. *Journal of Thermal Spray Technology*, 11(2):206–217, 2002.

[137] M. PasandidehâĂŘFard, Y. M. Qiao, S. Chandra, and J. Mostaghimi. Capillary effects during droplet impact on a solid surface. *Physics of Fluids*, 8(3):650–659, 1996.

[138] F. Pedrotti, L. Pedrotti, W. Bausch, and H. Schmidt. Optik für ingenieure. *Berlin/Heidelberg*, 2002.

[139] R. E. Pepper, L. Courbin, and H. A. Stone. Splashing on elastic membranes: The importance of early-time dynamics. *Physics of Fluids*, 20(8):082103, 2008.

[140] R. Pericet-Camara, G. K. Auernhammer, K. Koynov, S. Lorenzoni, R. Raiteri, and E. Bonaccurso. Solid-supported thin elastomer films deformed by microdrops. *Soft Matter*, 5(19):3611–3617, 2009.

[141] Precitec Optronik GmbH. Chrocodile cls operation manual, 2014.

[142] B. Prunet-Foch, F. Legay, M. Vignes-Adler, and C. Delmotte. Impacting emulsion drop on a steel plate: influence of the solid substrate. *J. Colloid Interface Sci.*, 199(2):151–168, 1998.

[143] H. C. Pumphrey and P. A. Elmore. The entrainment of bubbles by drop impacts. *Journal of Fluid Mechanics*, 220:539–567, 1990.

[144] K. Range and F. Feuillebois. Influence of surface roughness on liquid drop impact. *Journal of Colloid and Interface Science*, 203(1):16–30, 1998.

[145] G. Riboux and J. M. Gordillo. Experiments of drops impacting a smooth solid surface: a model of the critical impact speed for drop splashing. *Physical Review Letters*, 113(2):024507, 2014.

[146] R. Rioboo, C. Bauthier, J. Conti, M. Voue, and J. De Coninck. Experimental investigation of splash and crown formation during single drop impact on wetted surfaces. *Experiments in Fluids*, 35(6):648–652, 2003.

[147] R. Rioboo, C. Tropea, and M. Marengo. Outcomes from a drop impact on solid surfaces. *Atomization and Sprays*, 11(2), 2001.

[148] R. Rioboo, M. VouÃľ, A. Vaillant, and J. De Coninck. Drop impact on porous superhydrophobic polymer surfaces. *Langmuir*, 24(24):14074–14077, 2008.

[149] I. Roisman and C. Tropea. Impact of a drop onto a wetted wall: description of crown formation and propagation. *Journal of Fluid Mechanics*, 472:373–397, 2002.

[150] I. V. Roisman. Inertia dominated drop collisions. ii. an analytical solution of the navier–stokes equations for a spreading viscous film. *Physics of Fluids*, 21(5):052104, 2009.

[151] I. V. Roisman. Fast forced liquid film spreading on a substrate: flow, heat transfer and phase transition. *Journal of Fluid Mechanics*, 656:189âĂŞ204, 2010.

[152] I. V. Roisman. On the instability of a free viscous rim. *Journal of Fluid Mechanics*, 661:206–228, 2010.

[153] I. V. Roisman, E. Berberović, and C. Tropea. Inertia dominated drop collisions. i. on the universal flow in the lamella. *Physics of Fluids*, 21(5):052103, 2009.

[154] I. V. Roisman, T. Gambaryan-Roisman, O. Kyriopoulos, P. Stephan, and C. Tropea. Breakup and atomization of a stretching crown. *Physical Review E*, 76(2):026302, 2007.

[155] I. V. Roisman, K. Horvat, and C. Tropea. Spray impact: rim transverse instability initiating fingering and splash, and description of a secondary spray. *Physics of Fluids*, 18(10):102104, 2006.

[156] I. V. Roisman, A. Lembach, and C. Tropea. Drop splashing induced by target roughness and porosity: The size plays no role. *Advances in Colloid and Interface Science*, 222:615–621, 2015.

[157] I. V. Roisman, R. Rioboo, and C. Tropea. Normal impact of a liquid drop on a dry surface: model for spreading and receding. *Proceedings of the Royal Society of London. Series A: Mathematical, Physical and Engineering Sciences*, 458(2022):1411–1430, 2002.

[158] I. V. Roisman, N. P. van Hinsberg, and C. Tropea. Propagation of a kinematic instability in a liquid layer: Capillary and gravity effects. *Physical Review E*, 77(4):046305, 2008.

[159] B. L. Scheller and D. W. Bousfield. Newtonian drop impact with a solid surface. *AIChE Journal*, 41(6):1357–1367, 1995.

[160] A. Schmidt, B. Kühnreich, H. Kittel, C. Tropea, I. V. Roisman, A. Dreizler, and S. Wagner. Laser based measurement of water film thickness for the application in exhaust after-treatment processes. *International Journal of Heat and Fluid Flow*, 71:288–294, 2018.

[161] M. Schremb. *Hydrodynamics and Thermodynamics of Ice Accretion through Impact of Supercooled Large Droplets: Experiments, Simulations and Theory*. PhD thesis, Technische Universität, Darmstadt, 2018.

[162] R. D. Schulman and K. Dalnoki-Veress. Liquid droplets on a highly deformable membrane. *Physical Review Letters*, 115(20):206101, 2015.

[163] S. Shaikh, G. Toyofuku, R. Hoang, and J. Marston. Immiscible impact dynamics of droplets onto millimetric films. *Experiments in Fluids*, 59(1):7, 2018.

[164] Š. Šikalo and E. Ganić. Phenomena of droplet–surface interactions. *Experimental Thermal and Fluid Science*, 31(2):97–110, 2006.

[165] J. H. Spurk. *Dimensionsanalyse in der Strömungslehre*. Springer-Verlag, 2013.

[166] J. H. Spurk and N. Aksel. *Strömungslehre*, volume 4. Springer, 1989.

[167] R. Srikar, T. Gambaryan-Roisman, C. Steffes, P. Stephan, C. Tropea, and A. Yarin. Nanofiber coating of surfaces for intensification of drop or spray impact cooling. *International Journal of Heat and Mass Transfer*, 52(25-26):5814–5826, 2009.

[168] D. W. Stanton and C. J. Rutland. Multi-dimensional modeling of thin liquid films and spray-wall interactions resulting from impinging sprays. *International Journal of Heat and Mass Transfer*, 41(20):3037–3054, 1998.

[169] K. Takeuchi, K. Fujimoto, S. Hirano, and M. Yamashita. Investigation of engine oil effect on abnormal combustion in turbocharged direct injection-spark ignition engines. *SAE International Journal of Fuels and Lubricants*, 5(3):1017–1024, 2012.

[170] X. Tang, A. Saha, C. K. Law, and C. Sun. Bouncing-to-merging transition in drop impact on liquid film: Role of liquid viscosity. *Langmuir*, 34(8):2654–2662, 2018.

[171] G. I. Taylor. The dynamics of thin sheets of fluid. iii. disintegration of fluid sheets. *Proceedings of the Royal Society of London. Series A. Mathematical and Physical Sciences*, 253(1274):313–321, 1959.

[172] A. Terzis, M. Kirsch, V. Vaikuntanathan, A. Geppert, G. Lamanna, and B. Weigand. Splashing characteristics of diesel exhaust fluid (adblue) droplets impacting on urea-water solution films. *Experimental Thermal and Fluid Science*, 102:152–162, 2019.

[173] S. Thoroddsen, T. Etoh, and K. Takehara. High-speed imaging of drops and bubbles. *Annu. Rev. Fluid Mech.*, 40:257–285, 2008.

[174] S. Thoroddsen, T. G. Etoh, and K. Takehara. Crown breakup by marangoni instability. *Journal of Fluid Mechanics*, 557:63–72, 2006.

[175] P. Tourkine, M. Le Merrer, and D. Quéré. Delayed freezing on water repellent materials. *Langmuir*, 25(13):7214–7216, 2009.

[176] C. Tropea. Optical particle characterization in flows. *Annual Review of Fluid Mechanics*, 43:399–426, 2011.

[177] C. Tropea and M. Marengo. The impact of drops on walls and films. *Multiphase Science and Technology*, 11(1), 1999.

[178] C. Tropea and A. L. Yarin. *Springer handbook of experimental fluid mechanics*, volume 1. Springer Science & Business Media, 2007.

[179] M. Trujillo and C. Lee. Modeling crown formation due to the splashing of a droplet. *Physics of Fluids*, 13(9):2503–2516, 2001.

[180] C. Ukiwe and D. Y. Kwok. On the maximum spreading diameter of impacting droplets on well-prepared solid surfaces. *Langmuir*, 21(2):666–673, 2005.

[181] D. B. van Dam and C. Le Clerc. Experimental study of the impact of an ink-jet printed droplet on a solid substrate. *Physics of Fluids*, 16(9):3403–3414, 2004.

[182] N. P. Van Hinsberg, M. Budakli, S. Göhler, E. Berberović, I. V. Roisman, T. Gambaryan-Roisman, C. Tropea, and P. Stephan. Dynamics of the cavity and the surface film for impingements of single drops on liquid films of various thicknesses. *J. Colloid Interface Sci.*, 350(1):336–343, 2010.

[183] R. L. Vander Wal, G. M. Berger, and S. D. Mozes. The splash/non-splash boundary upon a dry surface and thin fluid film. *Experiments in Fluids*, 40(1):53–59, 2006.

[184] K. K. Varanasi, T. Deng, J. D. Smith, M. Hsu, and N. Bhate. Frost formation and ice adhesion on superhydrophobic surfaces. *Applied Physics Letters*, 97(23):234102, 2010.

[185] G. Videen, D. Ngo, P. Chỳlek, and R. Pinnick. Light scattering from a sphere with an irregular inclusion. *JOSA A*, 12(5):922–928, 1995.

[186] C. W. Visser, P. E. Frommhold, S. Wildeman, R. Mettin, D. Lohse, and C. Sun. Dynamics of high-speed micro-drop impact: numerical simulations and experiments at frame-to-frame times below 100 ns. *Soft Matter*, 11(9):1708–1722, 2015.

[187] P. Walzel. Zerteilgrenze beim Tropfenaufprall. *Chem. Ing. Tech.*, 52:338–339, 1980.

[188] A.-B. Wang and C.-C. Chen. Splashing impact of a single drop onto very thin liquid films. *Physics of Fluids*, 12(9):2155–2158, 2000.

[189] J. Wang, G. Gouesbet, Y. Han, and G. Gréhan. Study of scattering from a sphere with an eccentrically located spherical inclusion by generalized lorenz–mie theory: internal and external field distribution. *JOSA A*, 28(1):24–39, 2011.

[190] Z. Wang, A. A. Volinsky, and N. D. Gallant. Crosslinking effect on polydimethylsiloxane elastic modulus measured by custom-built compression instrument. *Journal of Applied Polymer Science*, 131(22), 2014.

[191] C. M. Weickgenannt, Y. Zhang, S. Sinha-Ray, I. V. Roisman, T. Gambaryan-Roisman, C. Tropea, and A. L. Yarin. Inverse-leidenfrost phenomenon on nanofiber mats on hot surfaces. *Physical Review E*, 84(3):036310, 2011.

[192] N. Welsch and C. C. Liebmann. *Ordnung der Farben*, pages 115–132. Spektrum Akademischer Verlag, Heidelberg, 2012.

[193] S. Wildeman, C. W. Visser, C. Sun, and D. Lohse. On the spreading of impacting drops. *Journal of Fluid Mechanics*, 805:636âĂŞ655, 2016.

[194] A. M. Worthington. Xxviii. on the forms assumed by drops of liquids falling vertically on a horizontal plate. *Proceedings of the Royal Society of London*, 25(171-178):261–272, 1877.

[195] A. M. Worthington and R. Cole. Impact with a liquid surface, studied by the aid of instantaneous photography. *Phil. Trans. R. Soc. Lond. A*, 189:137–148, 1897.

[196] L. Xu, W. W. Zhang, and S. R. Nagel. Drop splashing on a dry smooth surface. *Physical Review Letters*, 94(18):184505, 2005.

[197] L. Yang, C. Liu, and R. Shivpuri. Physiothermodynamics of lubricant deposition on hot die surfaces. *CIRP Ann-Manuf. Technol.*, 54(1):253–256, 2005.

[198] A. Yarin, M. Pfaffenlehner, and C. Tropea. On the acoustic levitation of droplets. *Journal of Fluid Mechanics*, 356:65–91, 1998.

[199] A. L. Yarin. *Free liquid jets and films: hydrodynamics and rheology*. Longman Publishing Group, 1993.

[200] A. L. Yarin. Drop impact dynamics: splashing, spreading, receding, bouncing ... *Annu. Rev. Fluid Mech.*, 38:159–192, 2006.

[201] A. L. Yarin, I. V. Roisman, and C. Tropea. *Collision Phenomena in Liquids and Solids*. Cambridge University Press, Cambridge, 2017.

[202] A. L. Yarin and D. A. Weiss. Impact of drops on solid surfaces: self-similar capillary waves, and splashing as a new type of kinematic discontinuity. *Journal of Fluid Mechanics*, 283:141–173, 1995.

[203] H.-T. Youn. Charakterisierung der Zusammensetzung von Krone und Sekundärtropfen nach dem Tropfenaufprall auf einen Flüssigkeitsfilm. Master thesis, Technische Universität, Darmstadt, 2018.

[204] A. Zahdeh, P. Rothenberger, W. Nguyen, M. Anbarasu, S. Schmuck-Soldan, J. Schaefer, and T. Goebel. Fundamental approach to investigate preignition in boosted si engines. *SAE International Journal of Engines*, 4(1):246–273, 2011.

Nomenclature

Latin letters

upper case

symbol	SI unit	description
A	m^2	surface area
A_{red}	m^2	surface area of red detected pixel
B	–	dimensionless constant
Ca	–	capillary number
D	–	diffusion coefficient
D_0	m	initial drop diameter
D_B	m	corona base diameter
D_C	m	corona rim diameter
D_{max}	m	maximum corona base diameter
$\overline{D}_{max}$	–	dimensionless maximum corona base diameter
$D_{max,spread}$	m	maximum spreading diameter
$\overline{D}_{max,spread}$	–	dimensionless maximum spreading diameter
E	–	eccentricity of the inclusion drop
G	$Pa=N/m^2$	shear modulus
H	m	corona height
H_c	1/m	mean curvature
K	–	K number
L	–	L number
L_{nd}	–	length scale of roughness
N	–	number of
N_{sec}	–	number of secondary droplets
Oh	–	Ohnesorge number
P_d	–	dimensionless stretching rate

Q	m^3/s	volume flux
R_b	m	corona radius
$\overline{R}_b$	–	dimensionless corona radius
Re	–	Reynolds number
R_{nd}	m	surface roughness
Rpk	m	average height of peaks over the roughness core profile
Rsm	m	mean width of profile element
$S, S(t)$	m^2	surface
T	K	temperature
U	m/s	velocity component in x-direction
U_0	m/s	impact velocity
V	m/s	velocity component in y-direction
V_O, V_W	m^3	volume of oil/water
V_r	m^3	volume of the red liquid inside the drop
V_{ges}	m^3	total volume of all secondary droplets
W	kg m^2/s^{-2}	work
We	–	Weber number
X	m	jet coordinate
X_B	–	interface

lower case

symbol	SI unit	description
c_1	–	concentration
d_c	m	diameter of cannula
f	$Hz = 1/s$	operating frequency
g	m/s^2	acceleration of gravity
h	m	film thickness
h_{res}	m	residual lamella thickness
$\overline{h}$	–	dimensionless residual lamella thickness
h_s	m	thickness of the free sheet
i	–	spanwise location $\left(i \in N_z\right)$

i, j, k	–	control variables of the coordinates
j_i	–	constant flux in z-direction
l	m	distance
m	kg	mass
n	–	sample size
p	$\mathrm{bar} = \mathrm{kg/m\,s^2}$	pressure
p_0	$\mathrm{bar} = \mathrm{kg/m\,s^2}$	ambient pressure
p_σ	$\mathrm{bar} = \mathrm{kg/m\,s^2}$	capillary pressure
r	m	radial coordinate
r_a	m	major semi-axis length
s	m	arc length of drop contour
s_p	–	standard deviation
t	s	time
t_i, t^i	s	time step i
t_1, t_2, t_3	s	characteristic time
t_p	–	correction factor
t_σ	s	typical time of capillary breakup
u	m/s	velocity component in x-direction
$\overline{u}$	–	dimensionless velocity component in x-direction
u_i	m/s	velocity (free index i)
$u_{\max}$	m/s	maximum velocity
v	m/s	velocity component in y-direction
x	m	chordwise coordinate
y	m	wall normal coordinate
z	m	axial coordinate

Greek letters

upper case

symbol	SI unit	description
Δ	–	constant positive displacement of the velocity field

ΔP	bar	Laplace pressure
Λ	–	impact parameter
Φ	°	angle

lower case

symbol	SI unit	description
$\alpha,\ \alpha_{incl}$	°	inclination angle
β	–	dimensionless constant
δ	–	relative film thickness
δ_{BL}	–	dimensionless thickness of the boundary layer
ϵ	–	area ratio of the red water drop to the total drop
η	–	dimensionless constant
$\dot{\gamma}$	1/s	shear rate
κ	–	kinematic viscosity ratio
μ	Pa s=Ns/m^2	dynamic viscosity
ν	m^2/s	kinematic viscosity
σ	N/m	surface tension
τ	–	dimensionless time
τ_{max}	–	dimensionless maximum spreading time
τ_{w}	Pa=N/m^2	wall shear stress
θ	°	contact angle
ρ	kg/m^3	density
$\overline{\rho}$	kg/m^3	mean density
χ	–	dimensionless constant
ξ	–	similarity vairable

Abbreviations

symbol	description
ad	advancing
CAM	camera
CCD	charged coupled device
CHR	chromatic confocal sensor
CLS	confocal Line Sensor
CMOS	complementary metal oxide semiconductor
corona	corona splash
cr	corona
d, D	drop
DOF	depth of field
Exp#	experiment number #
ext	external
f, F	fluid
FOV	field of view
fps	frames per second
GB	gigabyte
HS	high speed camera
HSI	hue saturation intensity
int	internal
lam	lamella
LED	light emitting diode
max	maximum
max, spread	maximum spreading
min	minimum
PDMS	polydimethylsiloxane
prompt	prompt splash
px	pixel
PI	pre ignition
r	radial coordinate

re	receding
res	resiudal
RGB	red green blue
spread	spreading
stat	statistical
sys	systematical
TDMS	technical data management structure
TU	Technische Universität
visc	viscous
wt.	weight
2D	two-dimensional
3D	three-dimensional

List of Figures

List of Tables